An Analysis of Surface Roughness and its Influence on a Thrust Bearing

by
Xiaohan Zhang

A dissertation submitted to the Graduate Faculty of
Auburn University
in partial fulfillment of the
requirements of the Degree of
Doctor of Philosophy

Auburn, Alabama
August 4, 2018

Keywords: Mixed Lubrication Analysis, Thrust bearing, Fractal Dimension, Tribology,
Rough Surface

Approved by

Robert L. Jackson, Chair, Professor of Mechanical Engineering
George Flowers, Professor of Mechanical Engineering
Dan Marghitu, Professor of Mechanical Engineering
Hans-Werner van Wyk, Assistant Professor of Mathematics and Statistics

ABSTRACT

Thrust bearings are a widely used type of bearing in many rotary industrial applications. In this work, a thrust bearing surface under the mixed lubrication regime is analyzed. A new model which coupled the mechanical deformation, thermo-elastic deformation, boundary lubrication and solid contact is developed to investigate the behavior of the thrust bearing during rotation. This new model provides predictions of important quantities such as the frictional torque, the load carrying capacity, the minimum film thickness, the temperature rise and the contact pressure.

During the rotation of the thrust bearing in the mixed lubrication regime, surface asperities in the thrust bearing surfaces can come into contact to influence the properties of the thrust bearing. Therefore, the characterization of the rough surfaces is also very important in studying the thrust bearings. Fractal descriptions of rough surfaces are widely used in tribology. The fractal dimension, *D*, is an important parameter which has been regarded as instrument independent, although recent findings bring this into question. A thrust bearing is analyzed in the mixed lubrication regime while considering the multiscale roughness of its surfaces. Surface data obtained from a thrust bearing surface is characterized and used to calculate the fractal dimension value by the roughness-length method. Then these parameters are used to generate different rough surfaces via a filtering algorithm. By comparing the predicted performance between the measured surface and generated fractal surfaces, it is found that the fractal

dimension must be used carefully when characterizing the tribological performance of rough surfaces, and other parameters need also be considered or found.

ACKNOWLEDGMENTS

I would like to acknowledge everyone who assisted me throughout my master's and doctoral studies over the years. First and foremost, I want to express my gratitude and gratefulness to my parents, my husband and my parents-in-law for their selfless support and encouragement.

I would like to acknowledge my advisor, Dr. Robert Jackson for his enthusiastic guidance and support during my studies in Auburn University. As my advisor, he has taught me more than I could ever give him credit for here. He has shown me, by his example, what a good professor should be. Much thanks to Mrs. Yang Xu for helping with my experiments and programming. I also want to express my thanks to my lab mates and friends, Xianzhang Wang, Bowen An, Swarna Saha, Nolan Chu and Alex Locker, who made me finish my dissertation in a relaxed and pleasant environment. I would like to thank my committee members and outside readers, Dr. George Flowers, Dr. Dan Marghitu, Dr. Hans-Werner van Wyk and Dr. Xinyu Zhang, for their supporting and guidance.

Last but not least, I want to thank my husband again who was not in Auburn during my preparation for the graduation. Therefore, I did not need to waste time quarreling with him and I could throw myself into writing my dissertation.

TABLE OF CONTENTS

LIST OF FIGURES

LIST OF TABLES

LIST OF ABBREVIATYONS

A_n	Nominal contact area
A^*	Contact area ratio
a	Radius of the contact circle
D	Fractal dimension
E	Equivalent Young’s modulus
f_c	Cut-off frequency
H	Hurst exponent
h	Nominal film thickness
h_{min}	Minimum film thickness
h_m	Separation of the mean surface height
h_s	Initial surface separation
K	Kurtosis
k_{ijkl}	Influence coefficient
k	Thermal conductivity
L	Load carrying capacity
l	Length of measured surface
n_w	Total number of square windows
p	Uniform pressure
p_0	Maximum pressure

Q	Volumetric heat
q_0	Cut-off wave vector
q	Wave vector
R	Thermal resistance
R_A	Asperity radius
R_q (σ)	Root mean square roughness
r	Radius of the center plate
Sk	Skewness
T	Frictional torque
TT	Temperature
TT_0	Ambient temperature
u	Surface deformation
V	Relative sliding speed
w	Side length
z_j	Residuals of the asperity height
$\bar{z}$	Mean residual asperity height
α	Thermal expansion coefficient
ϕ_r	Pressure flow factors in r direction
ϕ_θ	Pressure flow factors in θ direction
ϕ_s	Shear flow factor
η	Viscosity of lubrication
η_s	Asperity density
σ_s	Root mean square of the asperity height in GW model

ν	Poisson’s ratio
τ	Shear stress
τ_0	Yield stress of the grease
$\dot{\gamma}$	Shear rate
λ	Wavelength of the surface
μ	Expectation of the distribution
ω	Angular velocity
θ_0	Angle of one edge of the pad without grooves
θ_1	Angle of the other edge of the pad without grooves

CHAPTER 1

INTRODUCTION AND LITERATURE REVIEW

Thrust bearings are a special type of bearings which can support an axial force (acts parallel to the axis of rotation). It can also be called a flat faced bearing and is widely used in many rotary industrial applications, like the steering wheel, automatic transmission and engines. The investigation of the behavior of the bearings had received attentions for several decades, but most of the researches are focused on the analysis of the behaviors of journal bearings [1-11], rarely works have concerned the behavior of the flat faced thrust bearings.

The research of thrust bearings lies in many aspects, like the number of the grooves number, the shape of the grooves and thermal effect on the thrust bearings. Brockwell, et al. [12] changed the groove number in the thrust bearing from two to six to investigate the influence of the groove number experimentally. He concluded that four pads seem to be the optimized number in a thrust bearing.

In 1987, Heshmat, et al. [13] concerned with the performance of gas lubricated compliant thrust bearing, their work offered an analytical study of the elastohydrodynamics of the thrust bearing and the geometric parameters of the thrust bearing were also optimized to obtain the highest load carrying capacity. Heshmat also pointed out that the load carried by the asperities cannot be modeled by the classical Reynolds hydrodynamic analysis.

Carpino [14] investigated the flexible flat land thrust bearing at low speeds in 1990. In his work, point loads were applied to the thrust bearing to cause the surface deflection of the thrust bearing. Therefore, the converging clearances necessary for hydrodynamic lubrication can be created by the surface deflection. His work is perhaps the same as ours, except that he treated the fluid film between the disk and the plate as incompressible.

Most recently, the effects of groove geometry on the hydrodynamic lubrication thrust bearings were studied by Yu and Sadeghi [15] through developing a numerical model. Their work showed us that with proper groove geometries, the thrust bearing can support a significant amount of load for particular operating conditions and the thrust bearing has an optimum value of groove depth to support the maximum load carrying capacity. Yu also found that the number of grooves can have an influence on the load support mechanism, as Brockwell [12] also concluded, and there exists a critical characteristic number, γ_{cr}, for the groove number so that the load capacity can be diminished.

Over the years, the thermal effect on the thrust bearing was also considered in analyzing the behavior of the thrust bearing. Cameron and Wood [16] presented a general form of the theory for a grooved parallel surface thrust bearing while considering the thermal deformations, they assumed that the heat conducted away from the oil film through the metal can be neglected and the constant temperature exists across the film.

Taniguchi and Ettles [17] did some research on the parallel surface thrust bearing as well. In their work, a distorted film shape was displayed by using an optical interference method. It was concluded that thrust washers with random waviness tended to perform better than lapped bearings. It should be noted that the material of the bearing they used was aluminum to accentuate thermal expansion, which is not the same as what we used in our work.

In addition to considering the groove geometry effect on the thrust bearing, Yu and Sadeghi [18] discussed the thermal effects in the thrust bearing. They found that thermal effects can increase the side flow rate as well as reduce the load carrying capacity and the frictional torque. Meanwhile, thermal effects had a greater influence with the increase of the groove depth and groove numbers. Moreover, certain operating conditions existed before thermal effects dominated the thrust washer performance.

Meanwhile, Jackson and Green also did some research on the behavior of the thrust bearings. In 2006, Jackson and Green [19] investigated the behavior of the thrust bearings under the mixed lubrication and asperity contact. Thermoelastic deformations were considered later on and the relevant work was published in [20]. Both of these works predicted the frictional torque, bearing temperature, hydrodynamic lift and other indicators of bearing performance by coupling sliding friction, boundary lubrication, asperity contact and full-film lubrication together, which will also be considered in the current work.

During the analysis of the thrust bearing, rough surfaces also play an important role in the performance of thrust bearings since the roughness can affect the wear, friction and sealing behavior of contact surfaces. Therefore, effective characterization of surface roughness is a significant problem.

It can be found that typically the study of thrust bearings mainly focused on the groove effects [15], its behavior under mixed lubrication or hydrodynamic lubrication conditions [19, 21], and the thermal effects on the thrust washer [17, 18, 20]. Rarely works have combined the mixed lubrication analysis and the surface roughness effects together to analyze the behavior of a thrust bearing.

According to previous studies, essentially two different types of geometries are utilized in surfaces: Euclidean geometry and fractal geometry. Euclidean geometry has long been used to describe numerous natural phenomena. However, this kind of geometry has many limitations because it can be difficult to compute the multi-scale roughness of a real world geometry. To better characterize “rough” phenomena in both natural and artificial worlds, new approaches needed to be introduced in addition to Euclidean geometry. Arguably, Mandelbrot was the first person who pointed out that the fractal geometry seems much more suitable for describing the natural world, which is inherently rough on many scales [22]. Mandelbrot also defined a fractal as “a shape made of parts similar to the whole in some way” [23].

When using the fractal geometry to characterize rough surfaces, the most important parameter is the fractal dimension, D. It describes the space occupancy of an object and can be used to quantify the roughness of an object. Non-fractal Euclidian geometries have integer values for their fractal dimensions, like a line has a fractal dimension equal to one (D=1), the fractal dimension of a plane is two (D=2) and a space has fractal dimension equals to three (D=3). Fractal geometry can work with objects that are non-Euclidean because they have non-integer dimensions. The non-integer fractal dimension means an object is ‘in between’ these geometries due to features or roughness along the border of the object. For instance, one could envision that a line could approach the geometry of a plane as its roughness increases to become very large. Hence, roughness can be said to cause an object to have a dimension in between these geometries.

In this work, a thrust bearing with grease lubrication under the mixed lubrication regime is analyzed. The first aim of this work is to build a new model with consideration of the influence of the hydrodynamic lubrication, the solid contact, the mechanical deformation, and thermoelastic deformation, to investigate the behavior of the thrust bearing during the rotation. Therefore, this model can make predictions of the load carrying capacity, the frictional torque, washer temperature distribution and some other properties of the thrust bearing. The second aim is to combine the elasto-hydrodynamic lubrication and the rough surface contact effects together to analyze the effectiveness of the fractal methods in characterizing the thrust bearing surface. The third aim of this work is to analyze if the fractal parameter can represent a real surface adequately.

CHAPTER 2

METHODOLOGY

2.1 Pressure Calculation

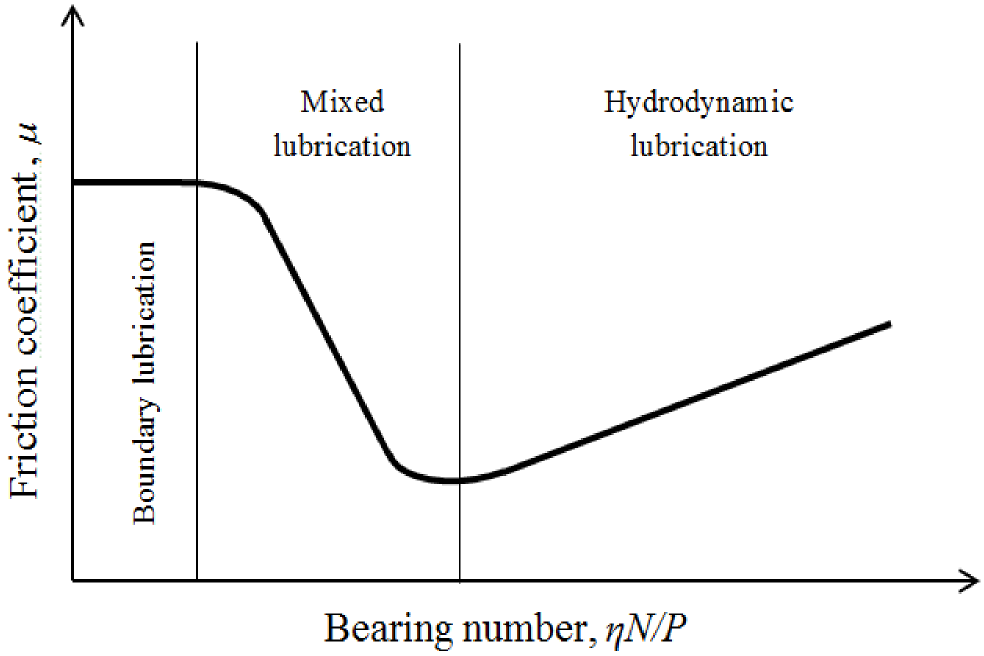

Fig.1- Schematic of a Stribeck curve

The Stribeck curve is basically a curve describing the relationship between the coefficient of friction and the bearing number (defined as the relative sliding velocity, *N*, times the viscosity of the lubricant, η, per unit load, *P*). According to the Stribeck curve (see Fig.1), a lubricated surface contact can be categorized by three regimes: the boundary lubrication regime, the mixed lubrication regime and the hydrodynamic lubrication regime. Despite the existence of a lubricating film between two contact surfaces, some surface asperities in the thrust bearing can still come into contact because of the surface roughness. Therefore, the contact between the thrust bearing surfaces in our work is considered to be in the mixed lubrication regime.

Normally, the mixed lubrication contact can be divided into a hydrodynamic lubrication part and a solid contact part. In our work, the flow-factor modified Reynolds equation [24, 25] is used to model the hydrodynamic lubrication between the interface and the Greenwood and Williamson (GW) model [26] is used to calculate the pressure and shear stress from the solid contact. Fig.2 illustrates the hydrodynamic lubrication part and the solid contact part in the mixed lubrication contact. The red area means the contact part between two surfaces.

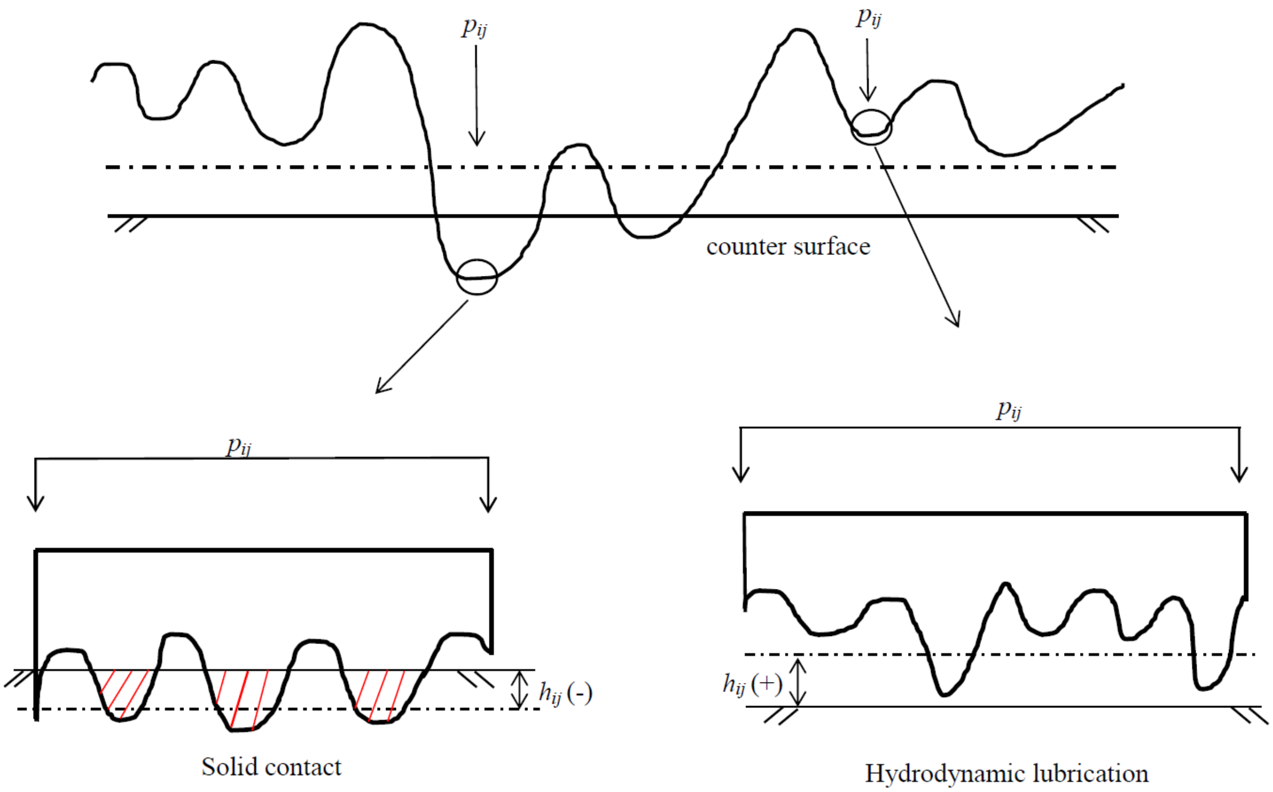

Fig.2- Illustration of hydrodynamic lubrication and the solid contact in the mixed lubrication contact

According to Patir and Cheng [24, 25], the fluid pressure p_f, generated by the hydrodynamic part can be calculated by the modified Reynolds equation in the cylindrical coordinates, which is [27]:

$$\frac{\partial}{\partial r}\left(\phi_r \frac{rh^3}{\eta}\frac{\partial p_f}{\partial r}\right) + \frac{1}{r}\frac{\partial}{\partial \theta}\left(\phi_\theta \frac{h^3}{\eta}\frac{\partial p_f}{\partial \theta}\right) = 12\left(\frac{r\omega}{2}\frac{\partial h}{\partial \theta} - \frac{r\omega}{2}\sigma\frac{\partial \phi_s}{\partial \theta}\right) \tag{1}$$

$$\phi_\theta = \phi_r = 1 - 0.9\exp(-0.56H) \tag{2}$$

$$\phi_s = \begin{cases} 1.899H^{0.98}exp(-0.92H + 0.05H^2) & H \leq 5 \\ 1.126\exp(-0.25H) & H > 5 \end{cases} \tag{3}$$

where ϕ_r and ϕ_θ are the pressure flow factors and ϕ_s is the shear flow factor (they are all calculated according to [28]); $H = h/\sigma$ is the ratio of the nominal film thickness h to the surface roughness σ; η is the viscosity of the lubricant. The flow factors consider how the roughness obstructs the flow between surfaces in close proximity. Since the roughness of the thrust bearing surface in our work is considered to be isotropic, the equations of flow factors for isotropic surfaces are used based on Patir and Cheng [24, 25], see Eqs. (2) and (3).

The Reynolds equation is solved by the finite difference method in our work (see Fig.3). There three different types of finite difference method: the backward difference (Eq. (4)), the forward difference (Eq. (5)) and the center difference (Eq. (6)). The center difference is chosen to solve the Reynolds equation in this work.

$$\left(\frac{df}{dx}\right)_n = \frac{f_n - f_{n-1}}{x_n - x_{n-1}} \tag{4}$$

$$\left(\frac{df}{dx}\right)_n = \frac{f_{n+1} - f_n}{x_{n+1} - x_n} \tag{5}$$

$$\left(\frac{df}{dx}\right)_n = \frac{f_{n+1} - f_{n-1}}{x_{n+1} - x_{n-1}} \tag{6}$$

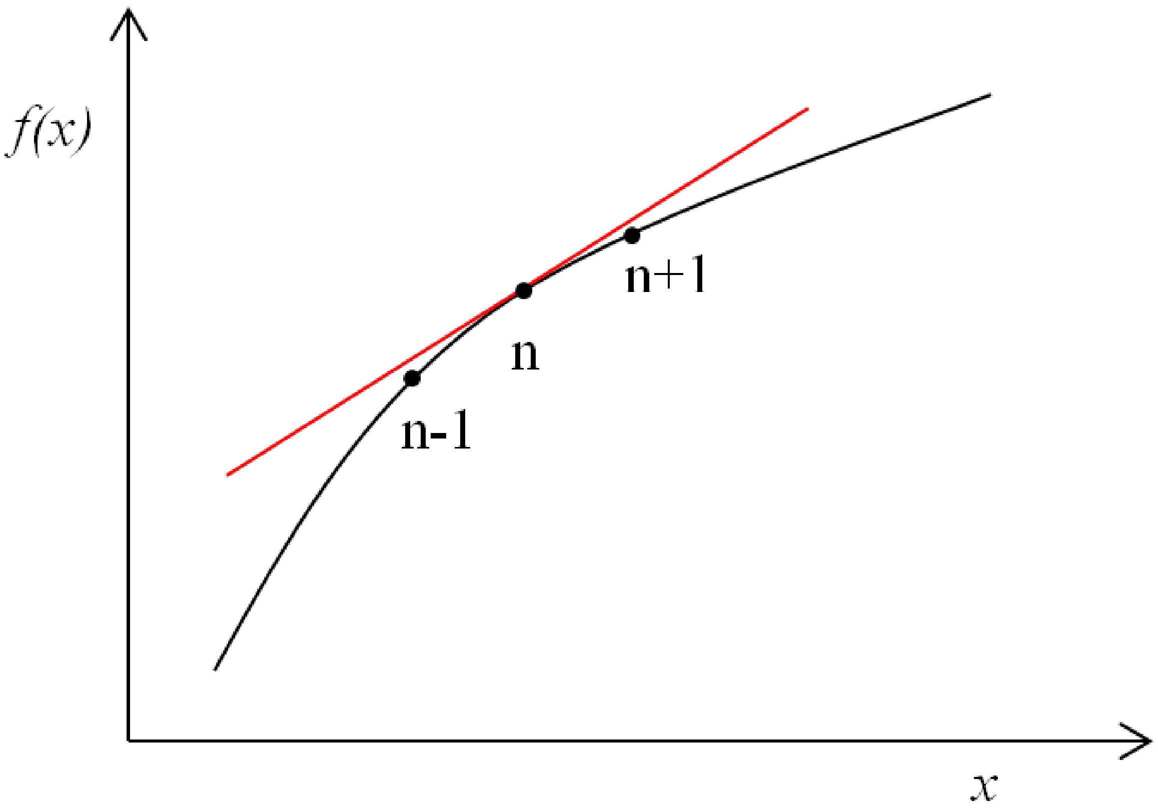

Fig.3 - Finite difference method

Greenwood and Williamson [26] derived the statistical contact models (which can also be called GW model) in 1966. In their model, they assumed that the contact asperities have the same radius of curvature and the contact asperities follow a Gaussian distribution when two real rough surfaces come into contact. Eq. (7) is the Gaussian distribution function in the GW model and the expressions of the solid contact pressure, p_s, calculated by the GW model are shown in Eq. (8).

$$\varphi(z) = \frac{1}{\sqrt{2\pi}\sigma_s} exp\left(-\frac{z^2}{2\sigma_s^2}\right) \tag{7}$$

$$p_s = \frac{4}{3}\eta_s E\sqrt{R}\int_d^{\infty}(z-h)^{\frac{3}{2}}\varphi(z)dz \tag{8}$$

where $\varphi(z)$ can also be called the probability function; η_s is the asperity density; E is the equivalent Young's modulus; σ_s is the root mean square of the asperity height; R is the radius of curvature and Eq. (8) is solved by the Simpson quadrature in our work.

According to the discussion in Chapter 1, thermal effects cannot be neglected during the performance analysis of the thrust bearing. The temperature rise can have an influence on many quantities of the thrust bearing system, like the deformation of the thrust washer and the rheological properties of the grease. Fig.4 shows the flow chart of the numerical process for the mixed lubrication analysis with coupling the mechanical deformation, thermo-elastic deformation, hydrodynamic lubrication and solid contact together. The left half of the flow chart shows the calculation process of the hydrodynamic half by using Reynolds equation and the right part of it shows the calculation process of the solid contact part. The film thickness between the two surfaces is updated every iteration. After the pressure and shear stress of the hydrodynamic lubrication part and the solid contact part are obtained from the calculation above (the convergence criteria for the pressure is $error \leq 1 \times 10^{-4}$), the frictional torque and load carrying capacity of the thrust bearing can be calculated.

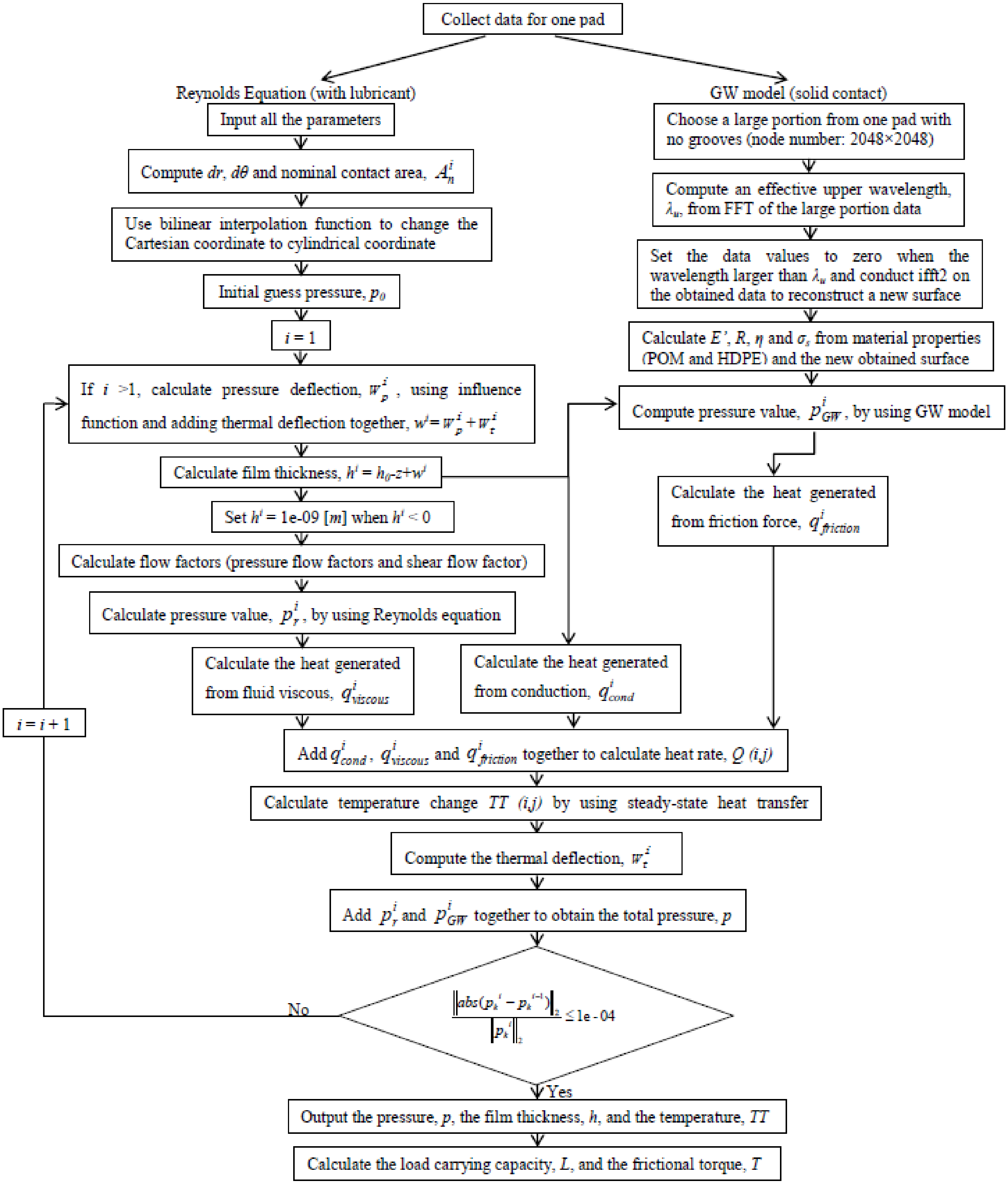

Fig.4 - Flow chart of the mixed lubrication analysis for the thrust bearing system

2.2 Surface Deformation

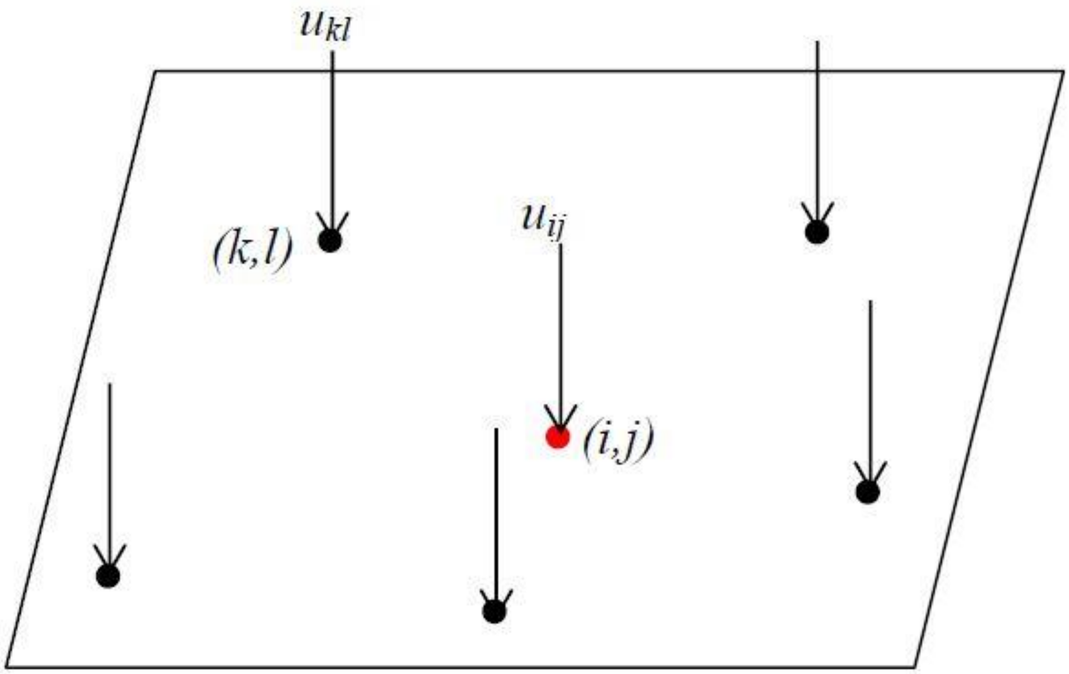

Fig.5 - Surface deformation on one point of a surface

When calculating the surface deformation, the thrust bearing surfaces are divided into discrete points, the deformation of the calculated point is influenced by the deformation of the other points in the surface (see Fig.5). Therefore, deformation of the other point should also be considered when calculating the mechanical deformation and thermal deformation of a node on the surface.

2.2.1 Mechanical deformation

By using the influence coefficient method, the elastic deformation of a node on the surface induced by an arbitrary pressure distribution can be calculated:

$$(u_{ij})_m = \sum_{k=1}^{N}\sum_{l=1}^{M} k_{ijkl} \cdot p_{kl} \tag{9}$$

where $(u_{ij})_m$ is the mechanical deformation of the calculated point, k_{ijkl} is the influence coefficient, p is the uniform pressure applied on the discrete points of the surface.

According to Love [29], the influence coefficient at a rectangular area (2a×2b) around a node can be calculated by the equation:

$$k=\frac{1-v^2}{\pi E}\left\{(x+a)\ln\left[\frac{(y+b)+\left\{(y+b)^2+(x+a)^2\right\}^{1/2}}{(y-b)+\left\{(y-b)^2+(x+a)^2\right\}^{1/2}}\right]+(y+b)\ln\left[\frac{(x+a)+\left\{(y+b)^2+(x+a)^2\right\}^{1/2}}{(x-a)+\left\{(y+b)^2+(x-a)^2\right\}^{1/2}}\right]\right.$$

$$\left.+(x-a)\ln\left[\frac{(y-b)+\left\{(y-b)^2+(x-a)^2\right\}^{1/2}}{(y+b)+\left\{(y+b)^2+(x-a)^2\right\}^{1/2}}\right]+(y-b)\ln\left[\frac{(x-a)+\left\{(y-b)^2+(x-a)^2\right\}^{1/2}}{(x+a)+\left\{(y-b)^2+(x+a)^2\right\}^{1/2}}\right]\right\} \tag{10}$$

where v is Poisson's ratio.

A verification of the influence function has also been conducted by comparing to a known solution. Suppose the contact between two elastic solid surfaces is Hertz contact (see Fig.6), the values of the related parameters are also shown in Fig.6 (Hertz contact is spherical contact, but it is solved in this work as a parabolic peak). The reference deformation can be calculated according to Johnson [30]:

$$u_{ref}\begin{cases}=\frac{1-v^2}{E}\frac{\pi p_0}{4a}(2a^2-r^2), & r\le a\\ =\frac{1-v^2}{E}\frac{p_0}{2a}\left\{(2a^2-r^2)sin^{-1}\left({}^{a}/_{r}\right)+r^2\left({}^{a}/_{r}\right)\left(1-{}^{a^2}/_{r^2}\right)^{1/2}\right\}, & r>a\end{cases} \tag{11}$$

where r is the radius where the contact point is located; a is the radius of the contact circle, p_0 is the maximum pressure. a and p_0 can also be calculated according to Johnson [30]:

$$a=\left(\frac{3PR}{4E}\right)^{1/3} \tag{12}$$

$$p_0=\frac{3P}{2\pi a^2} \tag{13}$$

where the values of P and R can be found in Fig.6.

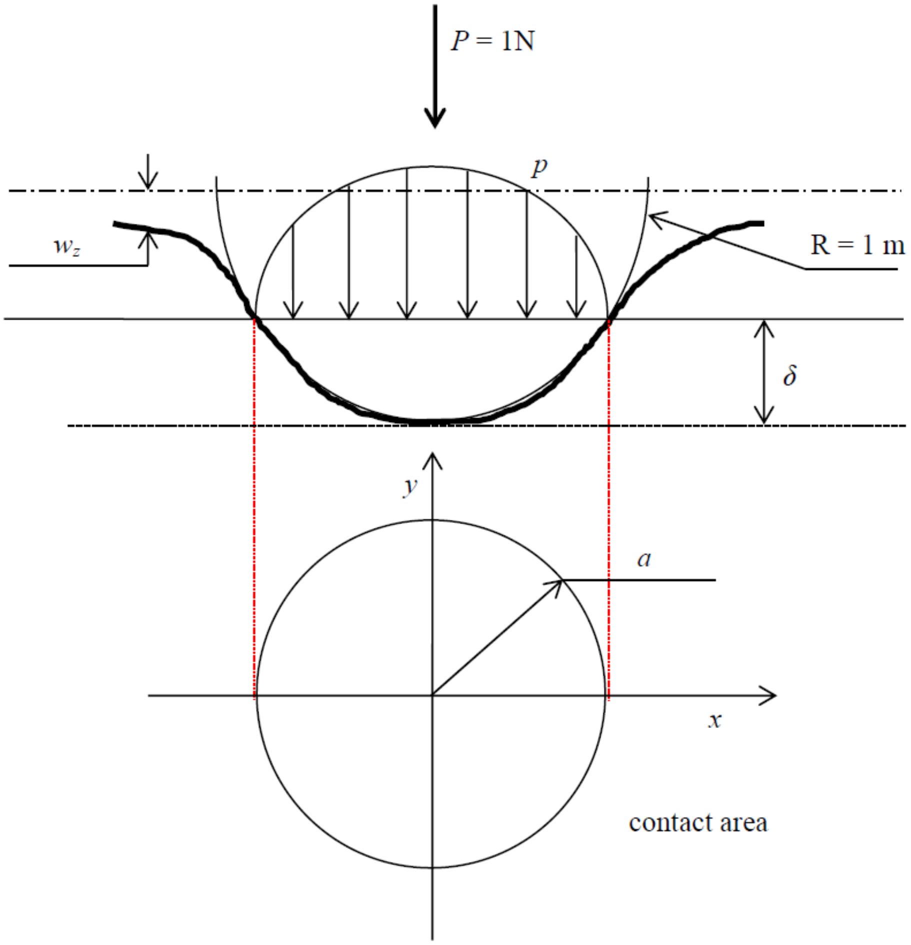

Fig.6 - Schematic illustration of Hertz contact

Fig.7 shows the plots of the deflection calculated by the influence function and the Hertz contact theory. It can be found that the deflection calculated by the influence function is matching satisfactorily with the deflection calculated by the Hertz contact theory, which means that the influence function algorithm is correct and can be used in calculating the deflection of the thrust bearing surface.

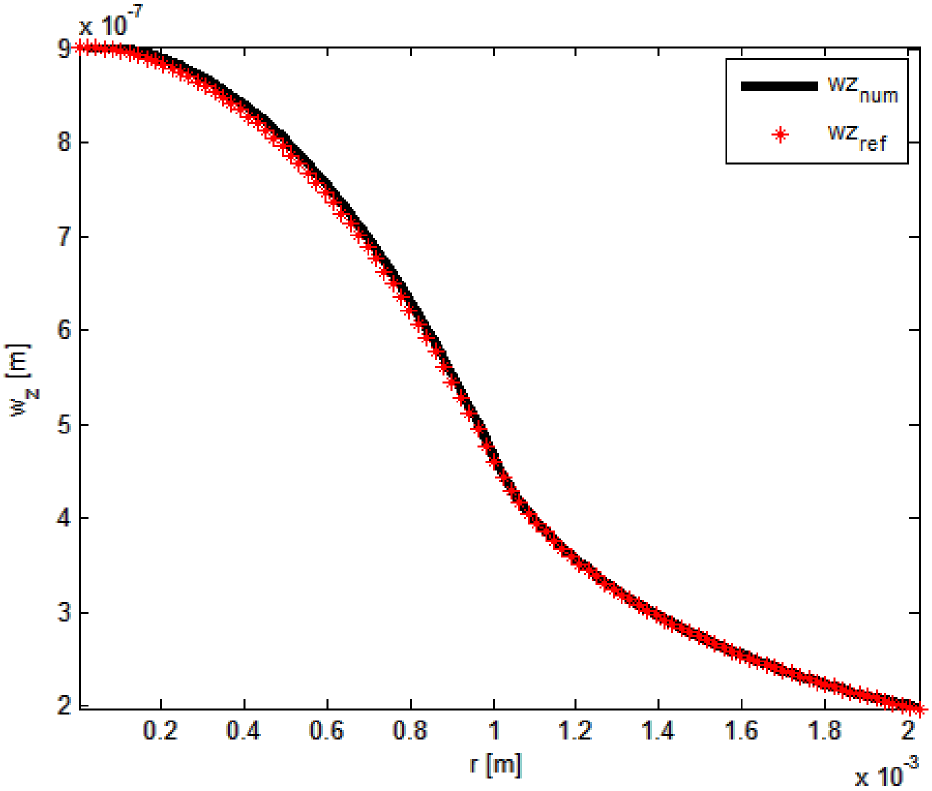

Fig.7 - Comparison of deflection calculated by the influence function and Hertz contact theory

2.2.2 Thermal deformation

The discretized points on the thrust bearing surface can be approximately regarded as a circular region at uniform temperature relative to an ambient temperature, *TT₀*, hence the thermos-elastic deformation can be calculated according to Barber [31]:

$$\left(u_{ij}\right)_t = \begin{cases} -\frac{2}{\pi}cka\left(\left(TT_{ij}\right)_c - TT_0\right)\left[ln\left(\frac{r_0}{a}\right) - ln\left\{1+\left(1-\frac{r^2}{a^2}\right)^{1/2}\right\} + \left(1-\frac{r^2}{a^2}\right)^{1/2}\right], & r \le a \\ -\frac{2}{\pi}cka\left(\left(TT_{ij}\right)_c - TT_0\right) ln\left(\frac{r_0}{r}\right), & r > a \end{cases} \tag{14}$$

where $(u_{ij})_t$ is the thermal deformation of the calculated point; r is the distance between the calculated point and the other point; r_0 is the position on the surface where $(u_{ij})_t$ is zero (r_0 is set to be three times of the pad diameter in the analysis); c is the constant given by $\alpha(1+\upsilon)/k$, α is the thermal expansion coefficient, k is the thermal conductivity which can be determined according to the material used in the thrust bearing; $\left(TT_{ij}\right)_c$ is the uniform temperature of a circular region of the calculated point; TT_0 is the ambient temperature, a is the radius of the circle around the calculated point.

2.3 Fractal Dimension Calculation

As we discussed in the references [32, 33], the roughness-length method appears to be the most effective method in calculating the fractal dimension value, so the 3D roughness-length method [34] is used to calculate the fractal dimension of the measured thrust bearing surface in this work.

For the 3D rough surfaces, the power law relationship between the standard deviation of the residual surface height, $S(w)$, and the sampling length window size, w, can be calculated by the equation below [34]:

$$S(w) = Aw^H \tag{15}$$

where H is the Hurst exponent and A is a constant. By dividing the rough surface into a grid of squares with the window length, w, $S(w)$ (can also be regarded as the root-mean-square roughness of the divided squares) can be calculated according to the following equation [34]:

$$S(w) = RMS(w) = \frac{1}{n_w}\sum_{i=1}^{n_w}\sqrt{\frac{1}{m_i - 2}\sum_{j \in w_i}(z_j - \bar{z})^2} \tag{16}$$

where n_w is the total number of square windows with the side length, w; m_i is the total number of points in the square window, w_i; z_j is the residuals of the asperity height on the trend, and $\bar{z}$ is the mean residual asperity height in each square window. For surfaces, the Hurst exponent, H, is related to the fractal dimension, D, with the equation $D = 3-H$. H can be obtained from the slope of the log-log plot of $S(w)$ and w.

CHAPTER 3

LUBRICANT VISCOSITY

3.1 Lubricant Used

As we mentioned previously, the lubricant we used between two thrust bearing surfaces is grease. Grease is regarded as a semisolid lubricant (it can also be called a non-Newtonian fluid), it is made up of a base oil, additives and the thickener. Petroleum or synthetic oil is typically used as the base oil, additives are used to modify the base oil properties and thickener is used to control the consistency of the base oil. According to the application, the grease we used in our work consists of G-501 (thickener) with KF-96-10 silicone oil (base oil).

Viscosity is a very important parameter used to measure the resistance of deformation for a lubricant when a shear stress or a tensile stress applied on it. Viscosity can effect heat generation in bearings related to a lubricant internal friction, it can also govern the sealing effect of the lubricant. The value of the viscosity can be influenced by the temperature change and the magnitude of the applied pressure. The grease lubricant is not the same as the frequently-used oil lubricant, it has a high initial viscosity and its viscosity is not only related to the temperature and the pressure but also related to the shear rate. Therefore, it is very hard to find the exact viscosity value of the grease from the handbook.

3.2 Herschel-Bulkley (H-B) Model

H-B model is a generalized model for a non-Newtonian fluid (shearing-thinning or shear-thickening), which combines the shear rate and the shear stress experienced by the fluid in a complicated way. By combining the viscosity of the grease and the generalized H-B model, a modified H-B model is used in this work:

$$\tau = \tau_0 + \eta\dot{\gamma}^n \tag{17}$$

where τ is the shear stress, τ_0 is the yield shear stress of the grease, $\dot{\gamma}$ is the shear rate. n is the flow index. η is the viscosity of the grease (will be discussed in Section 3.4). The fluid is shear-thickening for n >1, the fluid is shear-thinning for n <1. Both of k and n can be calculated according to the behavior of the grease.

Fig.8 - Physica MCR 301

Table 1 - Three tested data of the shear rate and shear stress of the grease

Shear rate, $\dot{\gamma}$ (s^{-1})	Shear stress (Pa)		
	First test	Second test	Third test
0.01	420.5340722	415.7246849	449
0.0158	423.6747764	415.8922065	454
0.0251	427.9071721	416.1608187	456
0.0398	433.5267798	416.5853994	466
0.0631	441.0115203	417.2583741	471
0.1	450.9730735	418.3241581	480
0.158	464.1409624	419.9993742	493
0.251	481.8859364	422.6854966	511
0.398	505.4470116	426.9313029	532
0.631	536.8279452	433.6610503	559
1	578.5932991	444.3188906	592
1.58	633.8017117	461.0710516	639
2.51	708.2002624	487.9322751	702
3.98	806.9837175	530.3903382	789
6.31	938.5531399	597.6878123	910
10	1113.660852	704.2662155	1080
15.8	1345.130669	871.7878248	1310
25.1	1657.05811	1140.400061	1630
39.8	2071.223039	1564.980691	2090
63.1	2622.848211	2237.955432	2740
100	3542.848211	3303.739464	3660

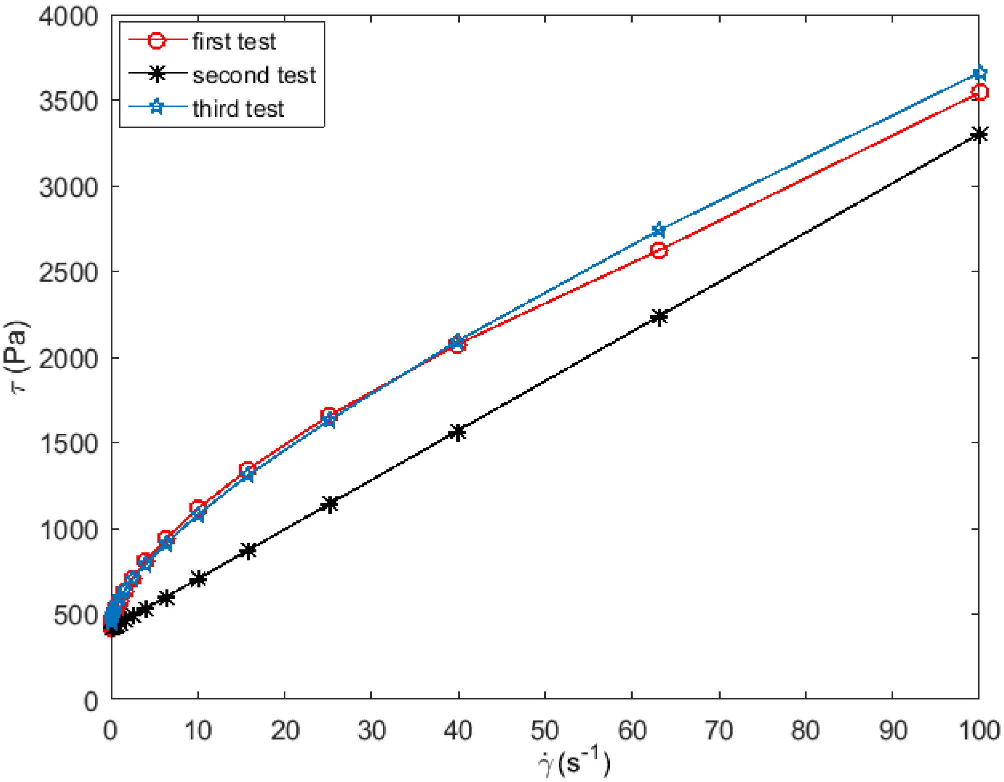

Fig.9 - Relationship between the shear stress and the shear rate of the grease

Table 2 - Parameter values in the modified H-B model

	First test	Second test	Third test	Average
Yield stress, τ_0 (Pa)	525	523	565	537.67
n	0.734188	0.708968	0.729417	0.724191

A Physica MCR 301 rheometer is used (see Fig.8) to test the grease properties and the grease is tested three times to make the measurement more accurate. Table 1 shows the three tested data of the shear rate and shear stress. Fig.9 shows the relationship between the shear stress and the shear rate of the grease based on the data in Table 1.

The intersection point of the fitted line with the y-axis is the value of the yield stress, τ_0, in Eq. (17). Table 2 shows the tested parameter values in the modified H-B model. By averaging the values in Table 2, the yield stress of the grease, τ_0, and the flow index, n, value can be obtained. Eq. (17) is then can be used to calculate the shear stress in this work.

3.3 Lubricant Viscosity Test

By changing the shear rate value in the Physica MCR 301 rheometer, the viscosity values of the grease will also be changed. The related viscosity values obtained from the tested machine are listed in Table 3. Fig.10 shows the plot of the tested results for the relationship between the averaged viscosity and the shear rate of the grease (these two values are plotted on a log-log scale) according to Table 3. It can be found from the plot that the viscosity decreases with the increase of the shear rate and the trend line seems to become flat when the shear rate becomes infinity.

Table 3 - Tested values of the shear rate and the viscosity

Shear rate, $\dot{\gamma}$ (sec^{-1})	Viscosity, μ_s ($Pa \cdot s$)			
	First test	Second test	Third test	Average value
0.01	49,150	41,100	44900	45,050
0.0158	32,900	30,600	31450	31,650
0.0251	20,850	19,900	20,000	20,250
0.0398	13,050	12,400	12,350	12,600
0.0631	8,225	7,940	7895	8,020
0.1	5,140	5,120	4,870	5,073
0.158	3,290	3,315	3,155	3,275
0.251	2,130	2,155	2,060	2,128
0.398	1,390	1,405	1,355	1,392
0.631	912	932	896	919
1	610	619	600	613
1.58	414	418	408	415
2.51	286	288	283	286
3.98	202	202	200	202
6.31	146	145	145	145
10	108	108	109	108
15.8	82.7	82	83	82
25.1	65.2	64	65	65
39.8	52.6	52	53	52
63.1	43.3	43	44	43
100	36.4	36	37	36

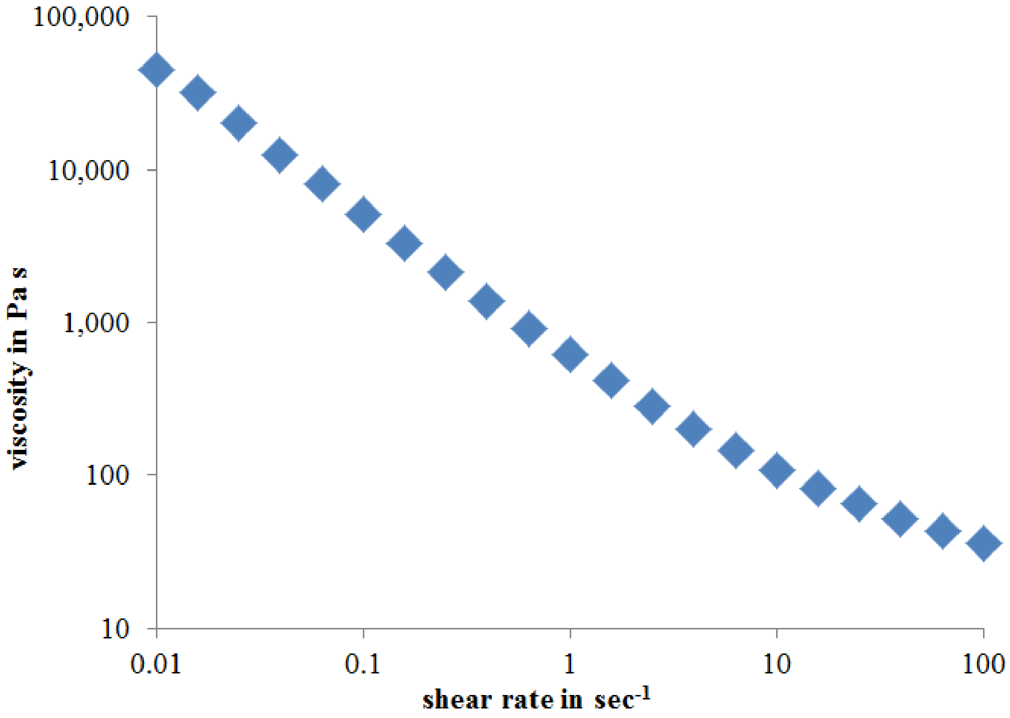

Fig.10 - Relationship between the averaged viscosity and the shear rate of the grease

3.4 Lubricant Viscosity Calculation

Fig.11 shows the fitted line of the log of the viscosity value and the log of the shear rate value in Fig.10 and the fitted equation can be obtained:

$$\eta_{sr} = \exp\begin{pmatrix} -0.00026064 \times (ln\dot{\gamma})^4 + 0.003912 \times (ln\dot{\gamma})^3 \\ +0.041273 \times (ln\dot{\gamma})^2 - 0.85966 \times (ln\dot{\gamma}) + 6.4078 \end{pmatrix} \tag{18}$$

The value of shear rate $\dot{\gamma}$ can be calculated from the equation below:

$$\dot{\gamma} = \frac{r \cdot \omega}{h} \tag{19}$$

where r is the radius of the center plate in the thrust bearing (which will be shown later), ω is the angular velocity (the velocity of the thrust bearing rotated around the intermediate shaft) of the thrust bearing system, *h* is the film thickness between the upper case and center plate (see Chapter 4).

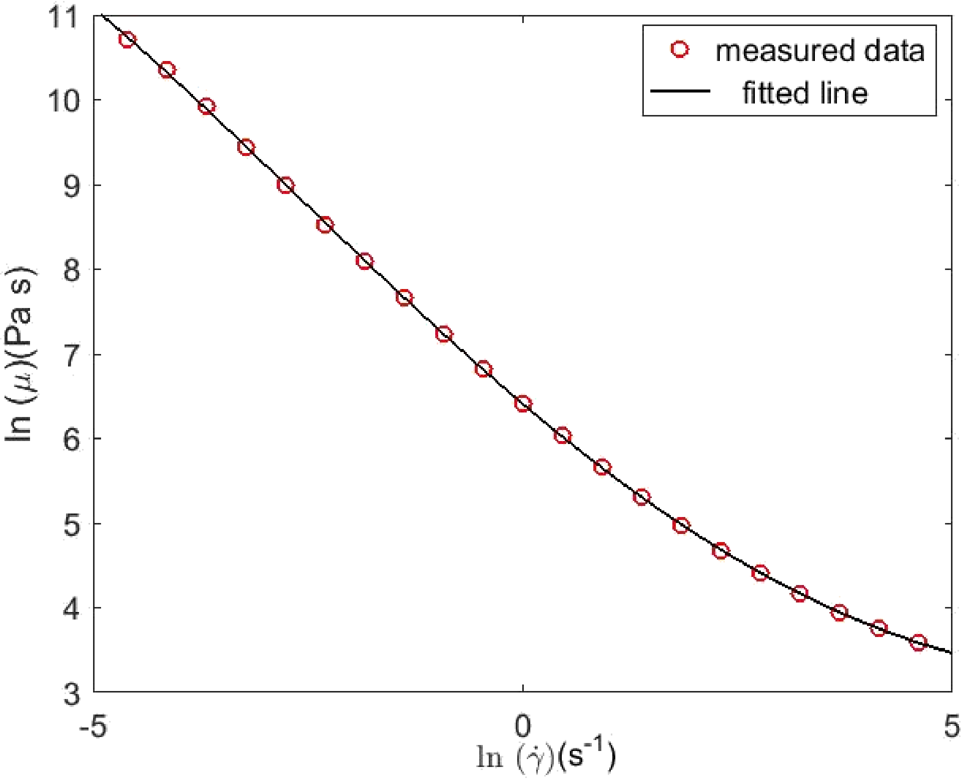

Fig.11 - Fitted line of the tested data in Fig.10

According to Hamrock [35], the relationship between the temperature and the viscosity of the grease can be written as:

$$\eta = \eta_c 10^{G_0\left(1+{TT_i}/{135}\right)^{-s_0}} \tag{20}$$

where G_0 is the dimensionless constant indicative of the viscosity grade of the liquid, s_0 is the dimensionless constant that establishes the slope of viscosity-temperature relationship. TT_i is the temperature at one node which can be calculated by the energy equation (will be discussed later), the unit of TT_i is ^oC; η_c in Eq. (20) can be calculated by the equation:

$$\eta_c = \frac{\eta_{sr}}{\eta_\infty} \tag{21}$$

where η_∞ = 6.31e-05 $N{\cdot}s/m^2$, it is an extrapolating analytical value of viscosity when TT_i tends to be infinite and it is approximately common to all oils according to Roelands [36].

G_0 and s_0 in Eq. (20) can be calculated by setting η_c in Eq. (20) equals to η_∞:

$$\eta_i = \eta_\infty 10^{G_0\left(1+{TT_i}/{135}\right)^{-s_0}} \tag{22}$$

Since it is very hard to find the viscosity values of the grease at different temperature and the properties of any grease are determined by the properties of the base oil, the properties of the base oil (which is KF-96-10 silicone oil in our research) are used instead to evaluate G_0 and s_0 values.

According to the performance test results of KF-96-10 silicone oil in the website (https://www.shinetsusilicone-global.com/catalog/pdf/kf96_e.pdf), when the temperature is 25^oC, the viscosity of the KF-96-10 silicone oil is 9.7 $N{\cdot}s/m^2$; when the temperature rises to 50 ^oC, its viscosity decreases to 6.79 $N{\cdot}s/m^2$. By putting these values into Eq. (20), values of G_0 and s_0 can be obtained (G_0 = 5.347, s_0 = 0.209)

Therefore, according to the calculation above, the grease viscosity we used in our research is:

$$\eta = \frac{\exp\begin{pmatrix} -0.00026064\times(ln\dot{\gamma})^4+0.003912\times(ln\dot{\gamma})^3 \\ +0.041273\times(ln\dot{\gamma})^2-0.85966\times(ln\dot{\gamma})+6.4078 \end{pmatrix}}{6.31\text{e}-05} \cdot 10^{5.347\left(1+\frac{TT_i}{135}\right)^{-0.209}} \tag{23}$$

CHAPTER 4

Numerical Methodology

4.1 Thrust Bearing Model

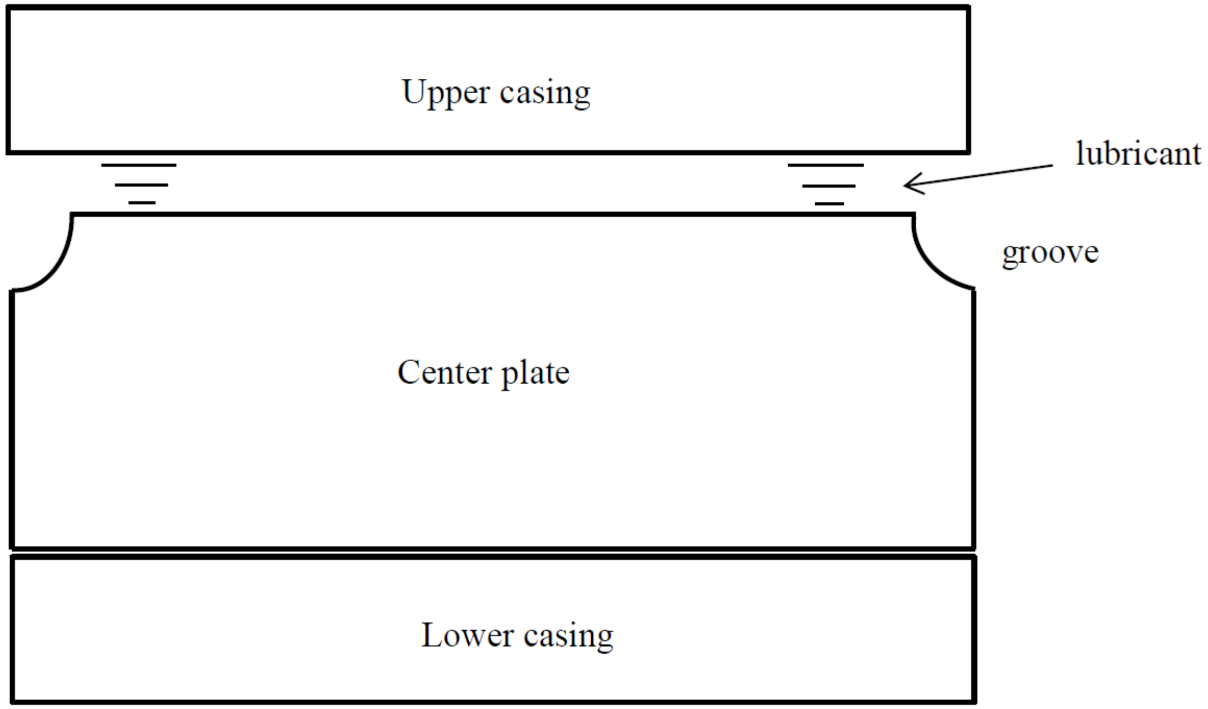

Fig.12 - Simplified schematic of the thrust bearing

The thrust bearing system studied in this work consists of an upper casing, a center plate and a lower casing. The upper casing and the lower casing are used to protect the sliding surface against the external environment and the upper casing is sliding against the center plate. There are 36 bearings pads in the center plate, the system around one pad of the thrust bearing is simplified as shown in Fig.12 for the convenience of studying and the grease is filled into the space between the upper case and the center plate. Fig.13 shows the coordinate setup in our thrust bearing system, the upper case is set at the location of $z = 0$ so that it is easy to calculate the shear stress (which will be shown later) .

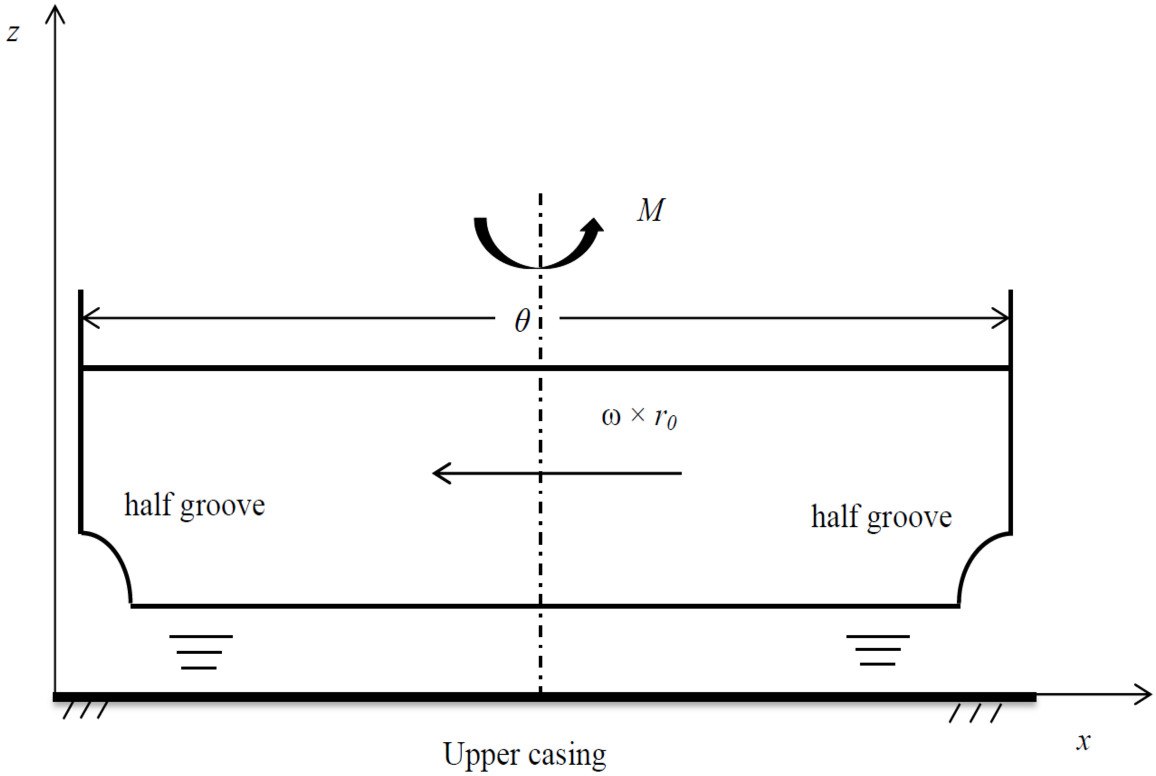

Fig.13 - Coordinate setup in the thrust bearing system

In the work, the thrust bearing surface is scanned with a Bruker NPFLEX system and part of it is shown in Fig.14 (the coordinate values are normalized by the outer radius value of the thrust bearing (r_o)). Because of the axisymmetric property of the thrust bearing system in our research, the load carrying capacity and the frictional torque for one pad of the center plate is studied and then these two values of the total bearing performance is 36 times of the values of the load carrying capacity and the frictional torque for one pad.

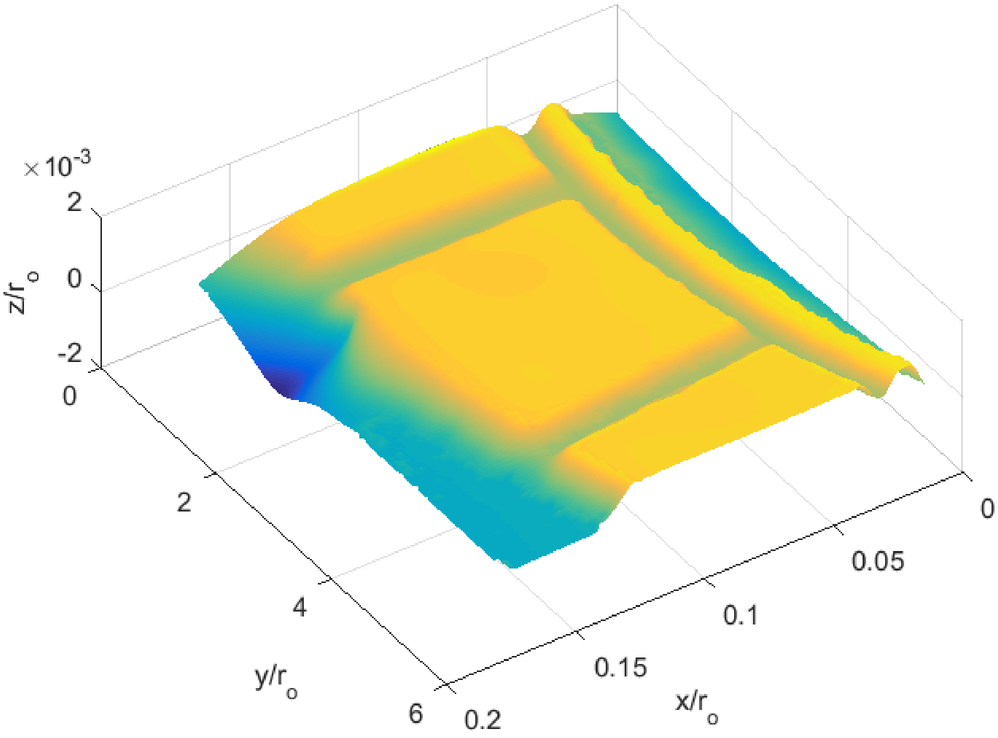

Fig.14 - Thrust bearing surface

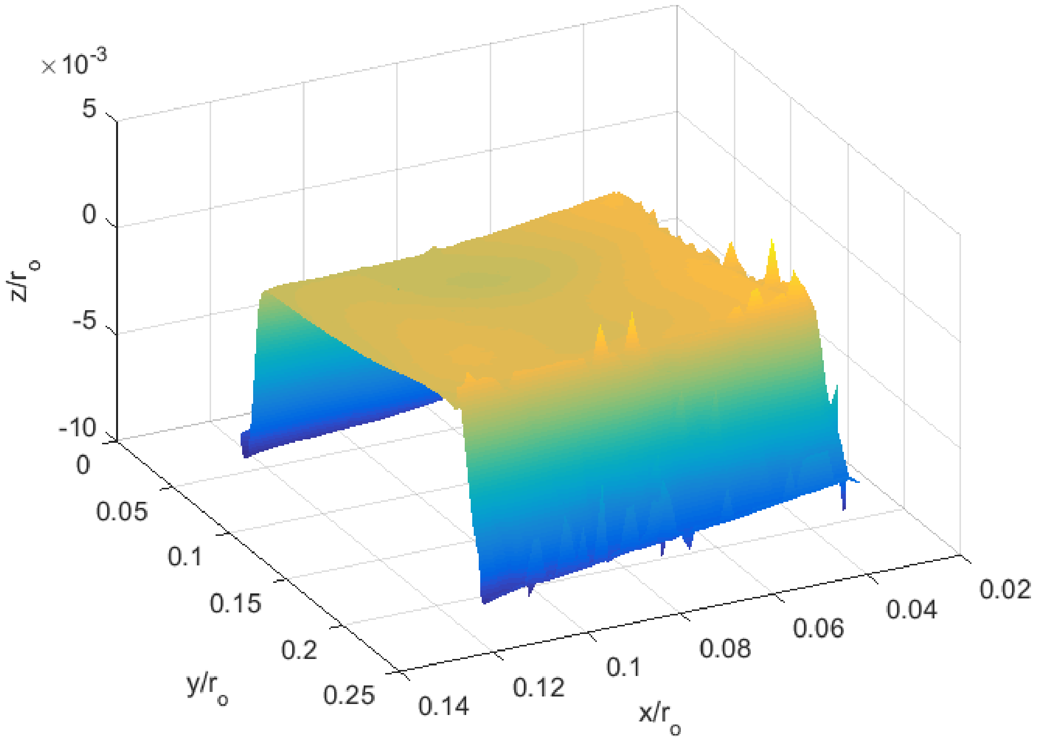

Fig.15 - One pad surface with radial grooves

One pad with two radial grooves is chosen which is shown in Fig.15 (the coordinate values are normalized by the outer radius value of the thrust bearing (r_o)). It can be found that there are lots of high peaks near the edges, which are from the experimental noise. These peaks are removed by replacing them with the average heights of the surrounding nodes for the better calculation as shown in Fig.16 (the coordinate values are normalized by the outer radius value of the thrust bearing (r_o)).

As we mentioned in Chapter 2, the thrust bearing system of the application is under the mixed lubrication regime and most of the pressure is from the solid contact part. Therefore, one single pad surface without grooves is chosen from the refined pad surface shown in Fig.17 (the coordinate values are normalized by the outer radius value of the thrust bearing (r_o)) and the surface data is collected.

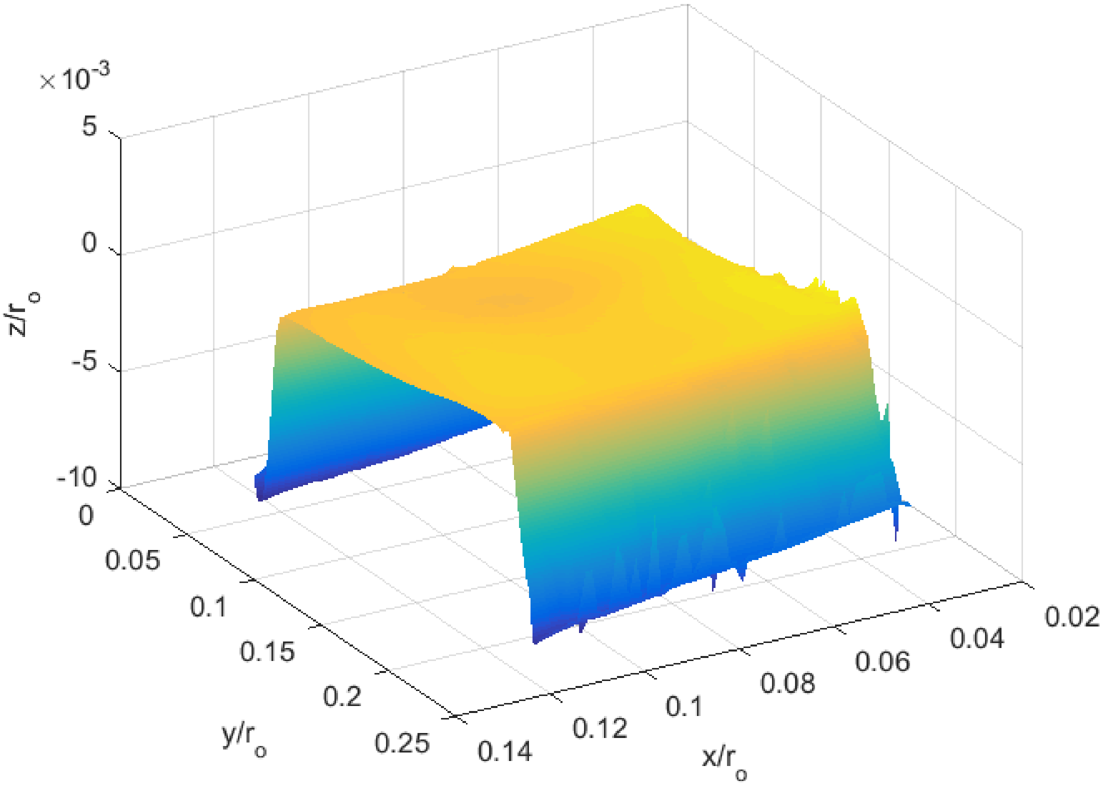

Fig.16 - One pad surface with radial grooves after refining

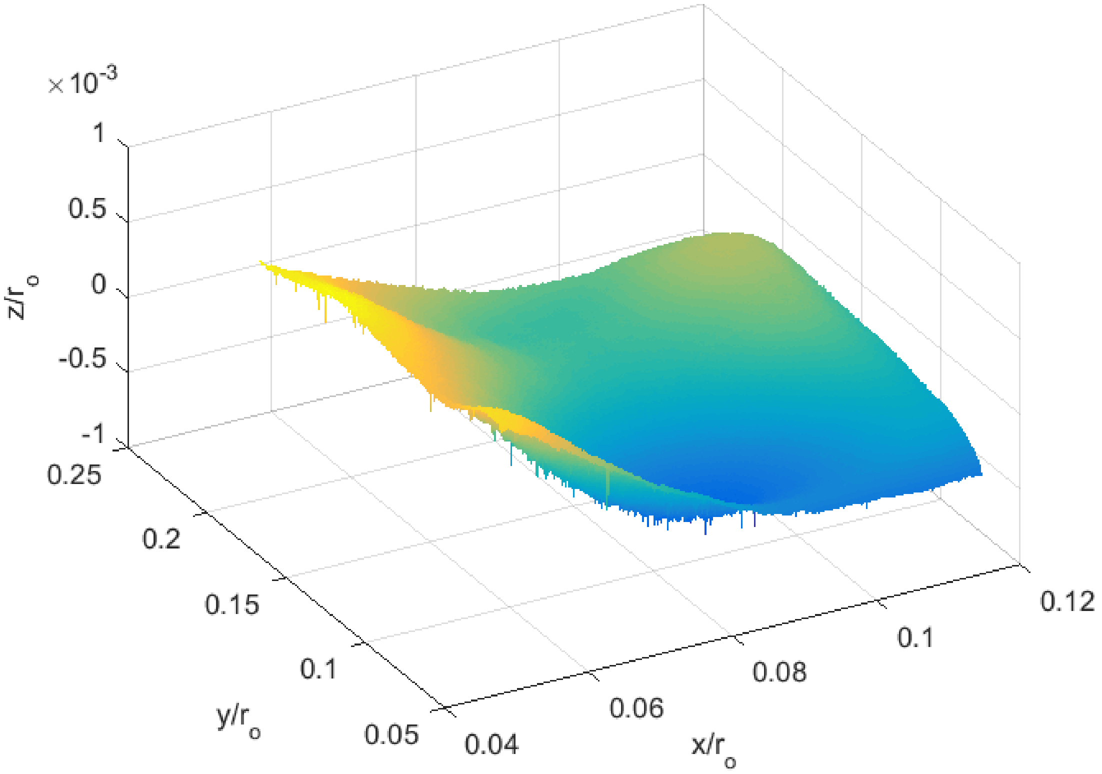

Fig.17 - One pad surface without grooves

Table 4 - Basic parameters calculated for the measured rough surface

Parameters	Values
Root mean square (R_q)	$1.0200\times10^{-5}\ m$
Kurtosis (K)	0.0057
Skewness (Sk)	-1.7321
Asperity radius (R_A)	$1.0241\times10^{-5}\ m$
Asperity density (η_s)	$3.2156\times10^{10}\ m^{-2}$

The collected data is leveled before being used to calculate the related surface parameters, so that the average slope of the surface is zero. Table 4 shows some basic parameters calculated for the pad surface.

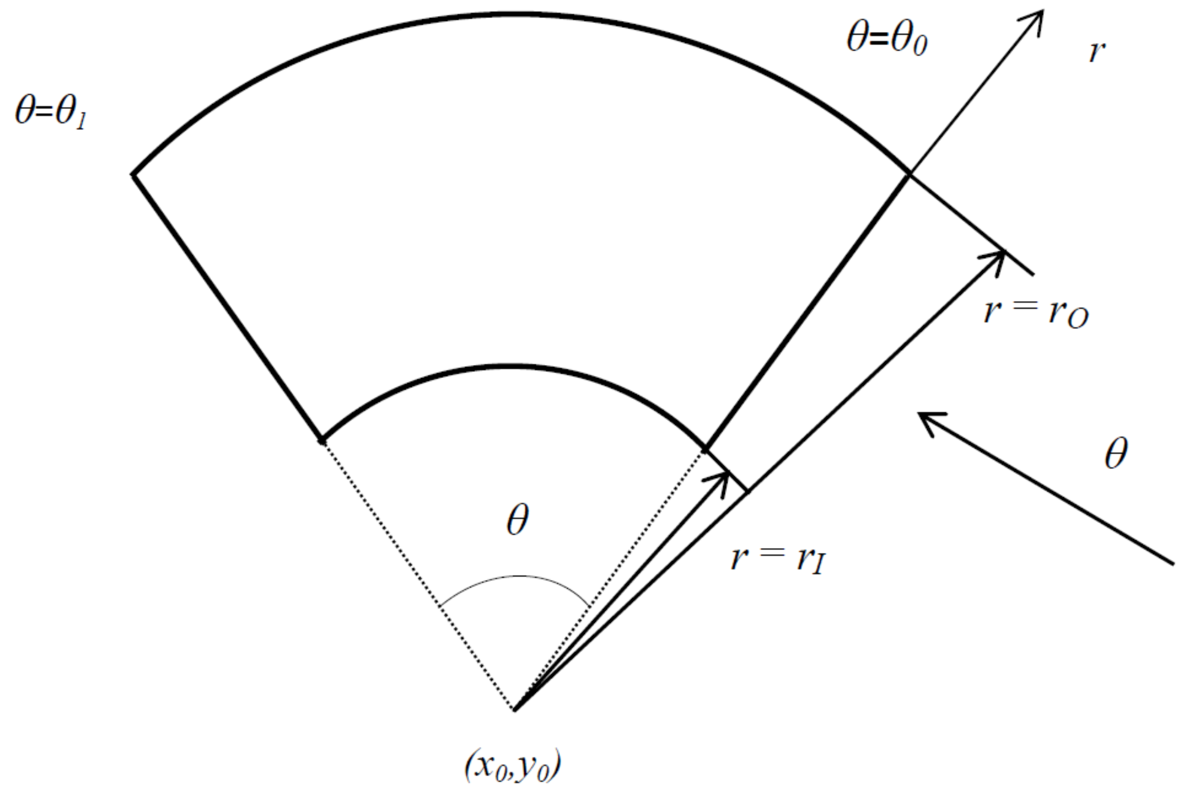

Fig.18 - Simplified sketch of one pad and its coordinate in cylindrical coordinate

The surface data is measured in the Cartesian coordinates, while the Reynolds equation is in the cylindrical coordinates (see Eq. (1) and Fig.18 shows a simplified sketch of one pad using cylindrical coordinates). Therefore, a coordinate transformation needs to be performed on the collected data so that the data can be used in the Reynolds equation. The in-plane coordinates transformation are shown in Eq. (24) and Eq. (25).

$$x - x_0 = rcos(\theta) \tag{24}$$

$$y - y_0 = rsin(\theta) \tag{25}$$

where x_0 and y_0 is the origin of the center of the thrust bearing in the Cartesian coordinate.

In the z direction, four closest-neighborhood points are found in the Cartesian coordinate and the bilinear interpolation function (Eq. (26)) is performed to map back the collected data onto the cylindrical coordinate system from Cartesian coordinates. Fig.19 shows the details of the coordinate transformation. The number of mapped nodes in the cylindrical coordinate is 60×120 (there are 60 points in the r direction and 120 points in the θ direction).

$$(x, y) = \frac{1}{(x_2 - x_1)(y_2 - y_1)} \begin{pmatrix} f(Q_{11})(x_2 - x)(y_2 - y) + f(Q_{21})(x - x_1)(y_2 - y) \\ +f(Q_{12})(x_2 - x)(y - y_{21}) + f(Q_{22})(x - x_1)(y - y_1) \end{pmatrix} \qquad (26)$$

where x_1, x_2, y_1 and y_2 are the coordinate values of points in the Cartesian coordinate, $Q_{11} = (x_1, y_1)$, $Q_{12} = (x1, y2)$, $Q_{21} = (x_2, y_1)$ and $Q_{22} = (x_2, y_2)$; $f(Q_{11})$, $f(Q_{12})$ $f(Q_{21})$ and $f(Q_{22})$ are the point heights in Cartesian coordinates and $f(x, y)$ is the point height in cylindrical coordinates.

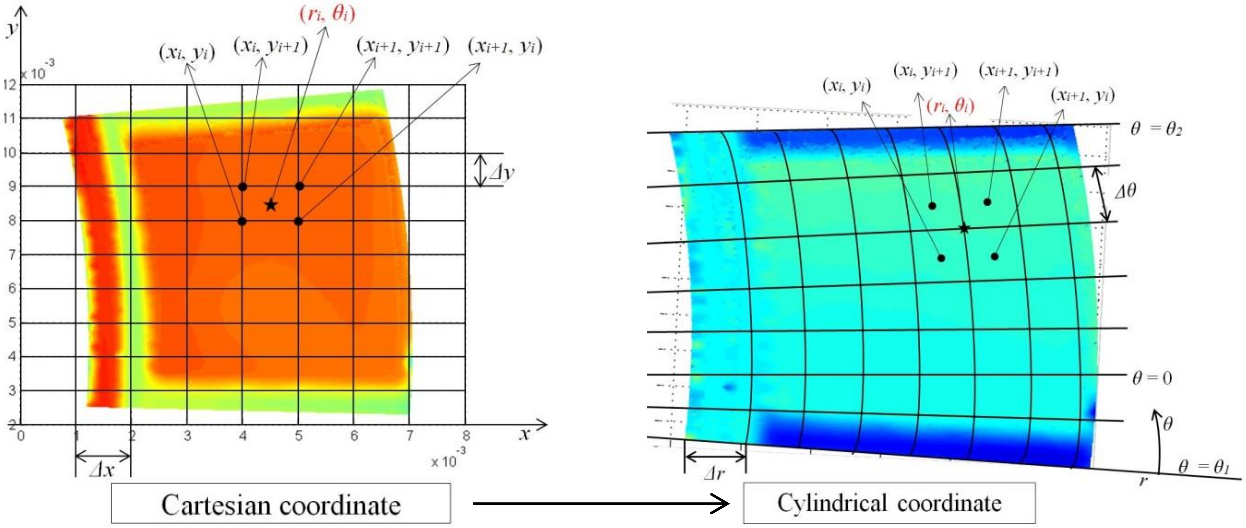

Fig.19 - Coordinate transformation from Cartesian coordinate to cylindrical coordinate

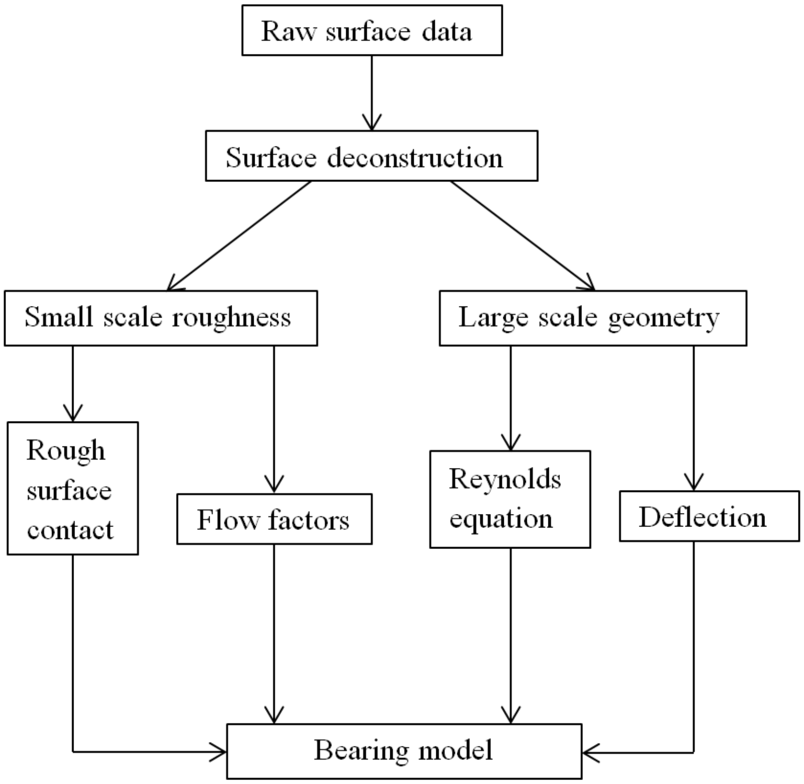

Fig.20 - Process of surface deconstruction

After the thrust washer surface is collected, the surface is deconstructed into small scale roughness and large scale roughness via a filtering algorithm according to a cut-off frequency. The parameters of the rough surface contact and the flow factors are calculated according to the small scale roughness, and the Reynolds equation and the surface deflection are solved based on the large scale geometry. Fig.20 shows the process of surface deconstruction and Fig.21 explains this process by figures (the coordinate values are normalized by the outer radius value of the thrust bearing (r_o)). By combining the small scale roughness part via rough surface contact and flow factors and the large scale geometry part together from Reynolds Equation (Eq. (1)) and macro-scale surface deformation, our bearing model is formed.

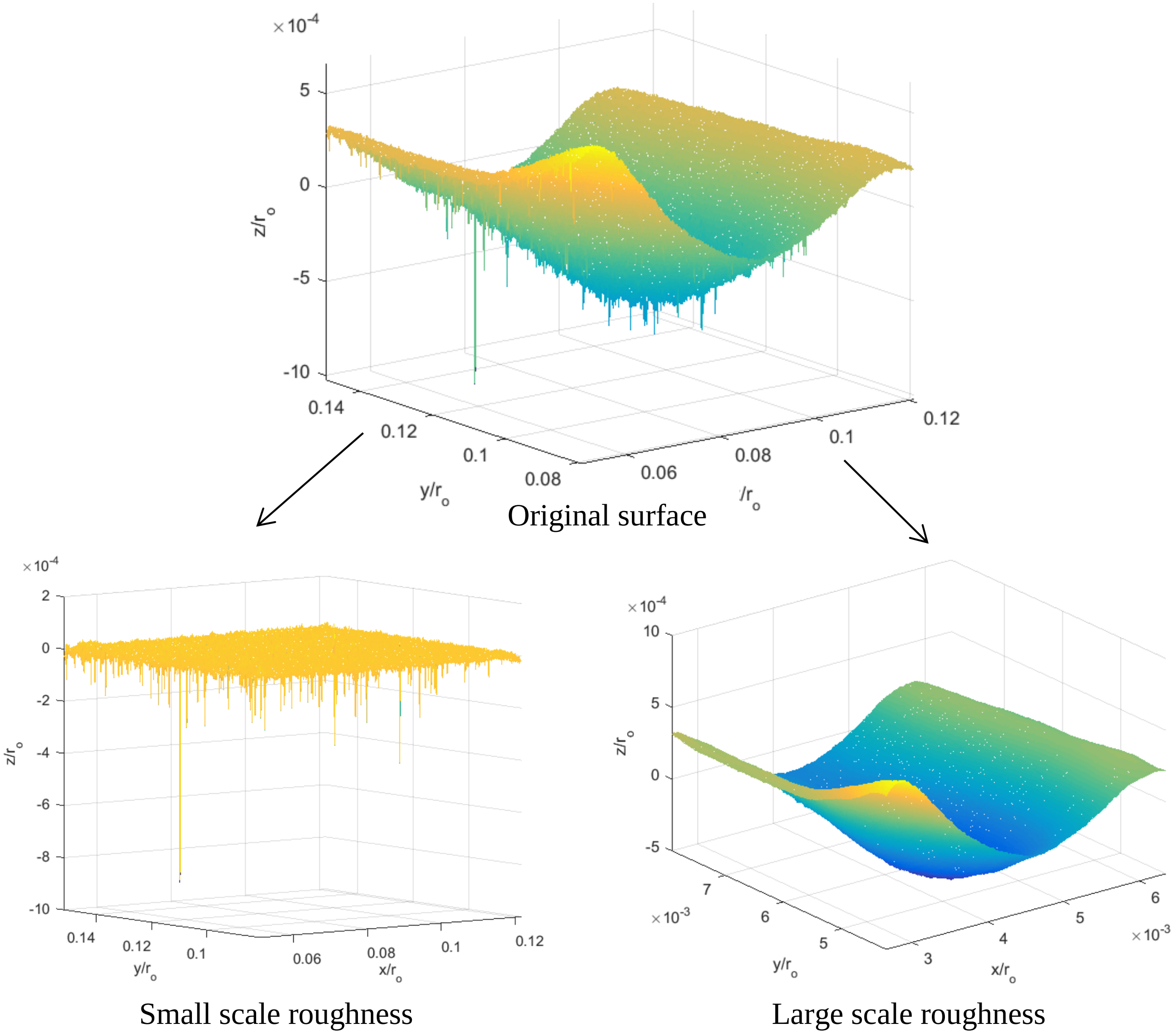

Original surface

Small scale roughness

Large scale roughness

Fig.21 - Process of surface deconstruction illustrated by figures

4.2 Heat Balance

In our analysis, the two-dimensional steady-state heat transfer equation from Özisik [37] under the cylindrical coordinates is used:

$$\frac{\partial^2 TT}{\partial r^2}+\frac{1}{r}\frac{\partial TT}{\partial r}+\frac{1}{r^2}\frac{\partial^2 TT}{\partial \theta^2}+\frac{1}{k}Q(r,\theta)=0 \tag{27}$$

where *TT* is the temperature distributed around each point, *Q(r,θ)* is the volumetric heat in the thrust bearing, it has three possible sources: a) the fractional heating from solid contact; b) the viscous heating from fluid shearing; c) the heat conducted to or from adjacent points on the thrust washer components. These sources will be described in detail later.

4.2.1 Code verification

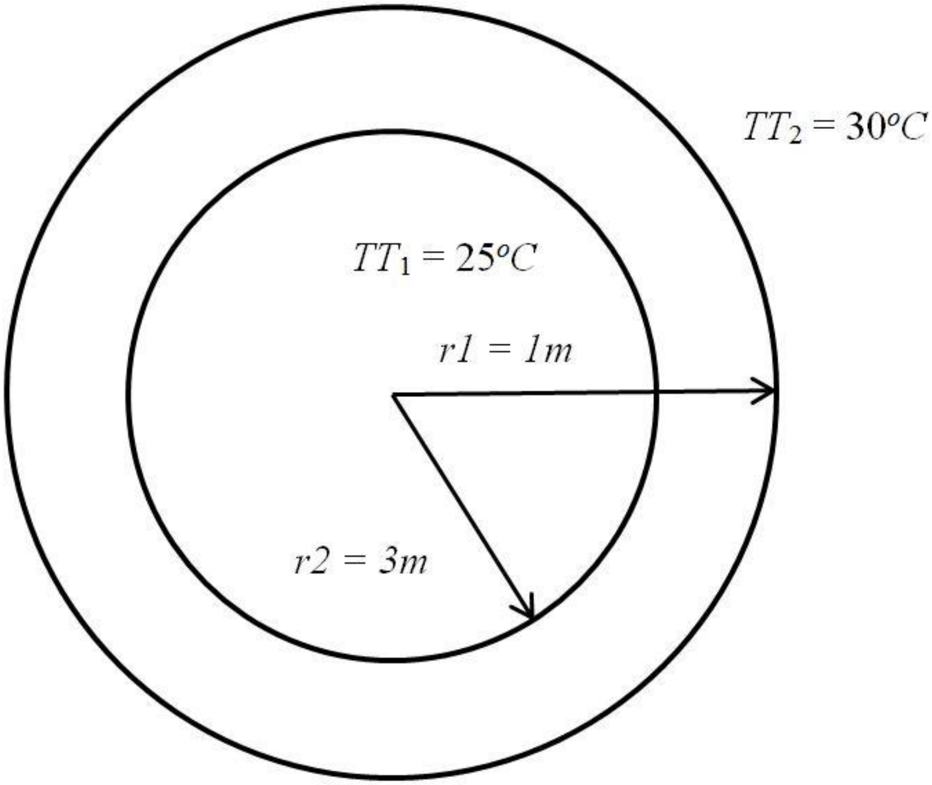

Fig.22 - Generic geometry for energy equation code verification

To verify our code for the energy equation used to calculate the temperature distribution around each point, a generic geometry under the axisymmetric condition without heat conduction is considered (see Fig.22). Then the energy equation can be written as Eq. (28) in this situation.

$$\frac{\partial^2 TT}{\partial r^2} + \frac{1}{r}\frac{\partial TT}{\partial r} = 0 \tag{28}$$

The analytical solution of Eq. (28) for the generic geometry is shown as Eq. (29) and the discretized numerical solution for Eq. (28) can also be obtained (see Eq. (30)).

$$TT = \frac{5}{ln3} ln(r) + 25 \tag{29}$$

$$\left(\frac{1}{\Delta r^2} - \frac{1}{2r\Delta r}\right) TT_{i-1.j} - \frac{2}{\Delta r^2} TT_{i,j} + \left(\frac{1}{\Delta r^2} + \frac{1}{2r\Delta r}\right) TT_{i+1,j} = 0 \tag{30}$$

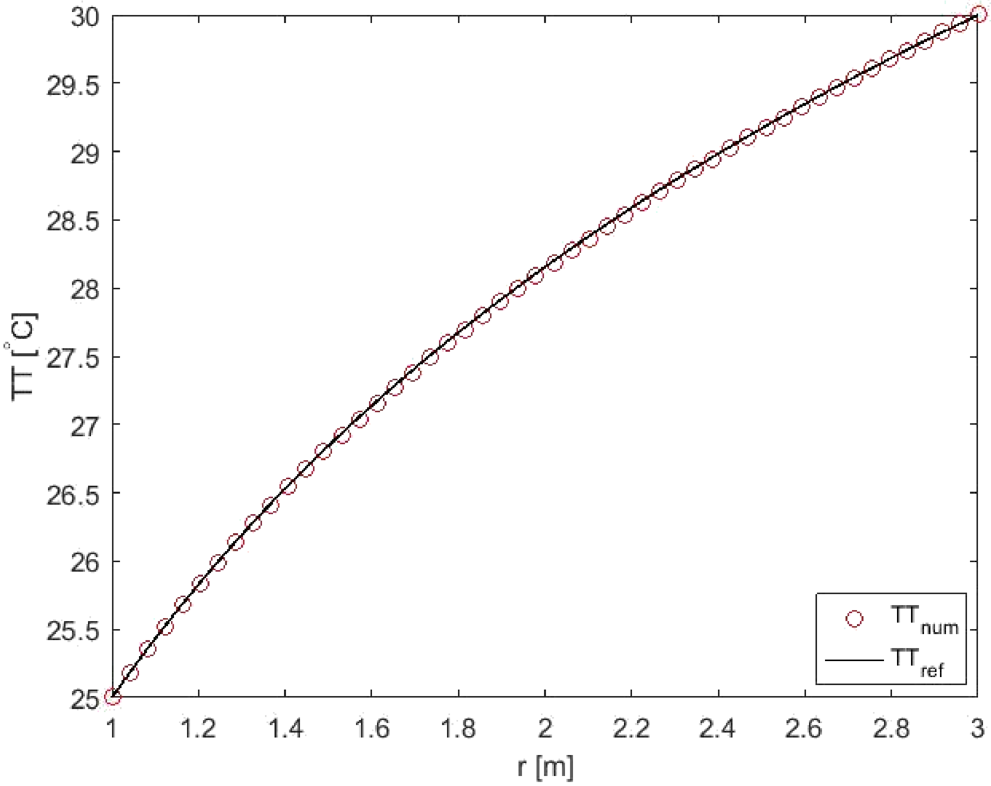

Fig.23 - Generic geometry for energy equation code verification

Fig.23 shows the results of temperature change calculated from the numerical solution and the analytical solution. The changing trends from these two solutions are effectively the same which indicates that the code for solving the energy equation is valid.

4.2.2 Volumetric heat calculation

a) Frictional heating

After the solid contact pressure is obtained based on the solid contact model (Eq. (8)), the equation of frictional heating at each node can be written as:

$$q_f^i = \tau_s^i A_i \tag{31}$$

$$\tau_s^i = V_i p_s^i \tag{32}$$

where τ_s^i is the shear stress generated from solid contact, A_i is the contact area, V_i is the relative sliding speed and p_s^i is the solid contact pressure at each node.

b) Viscous heating

The viscous heating is generated from fluid shearing based on the hydrodynamic lubrication model. For the calculation of the viscous hearting from grease lubrication, the modified Herschel-Bulkley model (H-B model) [38] is used to calculate the shear stress:

$$q_v^i = \tau_f^i A_i V_i \tag{33}$$

$$\tau_f^i = \tau_0 + \eta_i \left(\frac{r_i \omega}{h_i}\right)^n \tag{34}$$

where τ_f^i is the shear stress generated from the shear fluid at one node, τ_0 is the yield stress of the grease which has already known in Chapter 3, r_i is the radius and h_i is the film thickness at one node in the center plate, n = 0.724139 which is obtained from Chapter 3.

c) Heat conduction

The heat transfer between the adjacent components for one pad in the thrust bearing can be modeled as a one dimensional problem because the dimensions across the components and the grease film thickness are much smaller than the radial dimensions, which is drawn as Fig.24. Therefore, the heat conduction is only considered for the nodes with same radial and circumferential position in two components.

In Fig.24, R is the thermal resistance. R_u consists of the thermal resistance from the upper casing, the thermal resistance from the fluid and the thermal resistance from half of the center plate. R_l includes the thermal resistance from half of the center plate and the thermal resistance from lower casing. TT_0 is the ambient temperature which is set to be 25°C and TT_c is the temperature of center plate. In this work, Heat convection is not considered because of its expected small value compared with the heat conduction. In addition, the temperature of one pad is considered as periodical in the circumference direction and the temperature in the inner and outer radii is also set to equal to TT_0 (25°C) (see Fig.25).

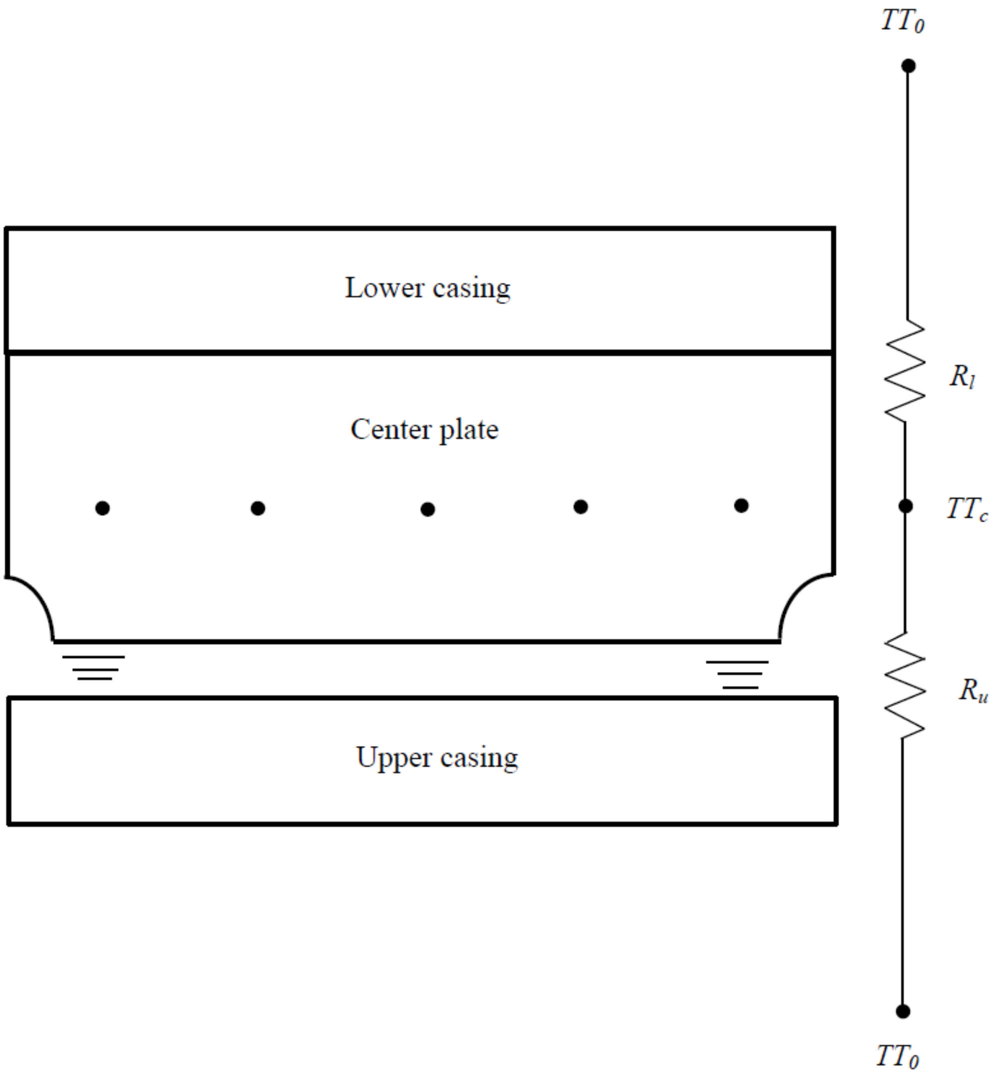

Fig.24 - Schematic of heat transfer between components (not drawing for scale)

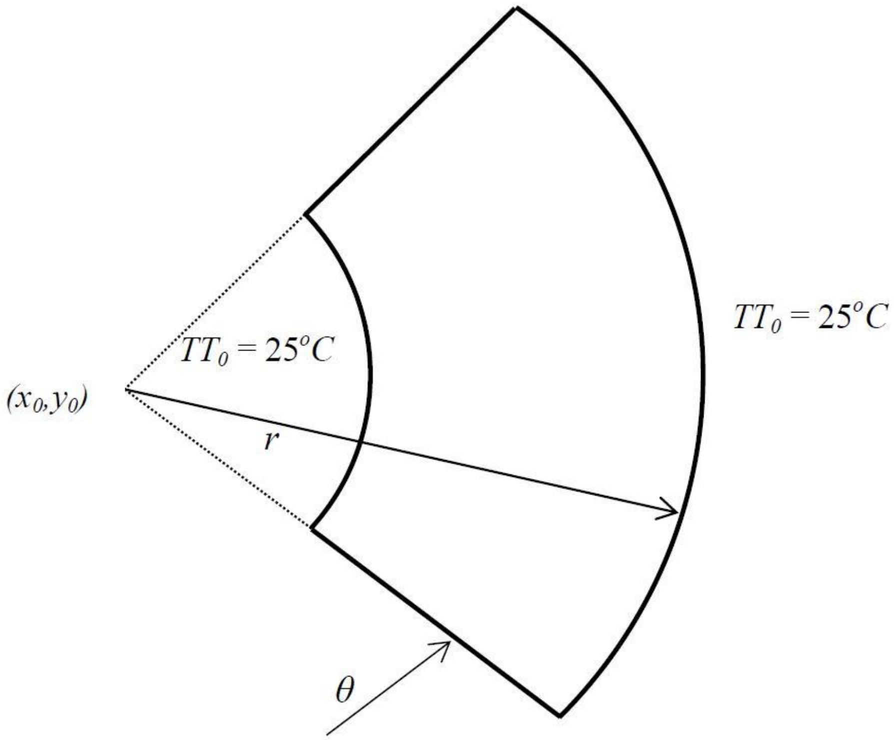

Fig.25 - Periodical temperature in circumference direction

The heat conducted between components can be calculated by using the thermal resistance according to [20, 39]:

$$R_u = R_{fluid} + R_{upper} + \frac{R_{center}}{2} = \frac{h_m}{k_{fluid}} + \frac{t_{upper}}{k_{upper}} + \frac{t_{center}}{2k_{center}} \tag{35}$$

$$R_l = R_{lower} + \frac{R_{center}}{2} = \frac{t_{lower}}{k_{lower}} + \frac{t_{washer}}{2k_{washer}} \tag{36}$$

where t is the thickness of each component; k_{fluid} is the thermal conductivity of the grease that can be determined according to the property of base oil (KF-96-10 silicone oil) in the grease; k_{upper}, k_{center} and k_{lower} are the thermal conductivity of the upper casing, center plate and lower casing, these three values can all be determined for the particular materials of the upper casing, the center plate and the lower casing; h_m is the separation of the mean surface height between upper casing and the center plate. Then the conducted heating along *z* direction for a node i in component *a* to the same location in the adjacent component *b* is:

$$q_c^i = \frac{TT_a - TT_b}{R_{a \to b}} \tag{37}$$

After all the heating parts are calculated, the volumetric heat around one node can be obtained by:

$$Q_i(r,\theta) = \frac{\left(q_f^i + q_v^i\right)}{t_i A_i} + \frac{q_c^i}{t_i} \tag{38}$$

where t_i is the thickness of the component at node i.

Since the heat convection is not considered, the temperature change in the boundary nodes can be ignored and only the internal nodes temperature change is calculated. By taking Eq. (38) into Eq. (27) and using the finite difference method, the discretized temperature ($TT_{i,j}$) expression for internal nodes solved by the energy equation is shown below:

$$TT_{i,j} = \frac{\left[\left(\frac{1}{\Delta r^2}+\frac{1}{2r\Delta r}\right)TT_{i,j}+\left(\frac{1}{\Delta r^2}-\frac{1}{2r\Delta r}\right)TT_{i-1,j}+\frac{1}{r^2\Delta\theta^2}TT_{i,j+1}+\frac{1}{r^2\Delta\theta^2}TT_{i,j-1}+\frac{1}{k}Q_{i,j}\right]}{\left(\frac{2}{\Delta r^2}+\frac{2}{r^2\Delta\theta^2}\right)} \tag{39}$$

The Gauss-Seidel method is used to solve for the temperature between two nodes in the adjacent components according to Eq. (39). Then the calculated temperature value can be put back in Eq. (14) to compute the thermal deformation.

4.3 Contact Area Ratio

Contact area ratio is a measure of how much actual area come into contact during the rotation of the thrust bearing system. When two surfaces come into contact, only asperities on the surfaces can come into contact since the existence of the roughness on the surface. Therefore, surface roughness can decrease the real area of contact. The contact area ratio around one measured point can be calculated according to Greenwood and Williamson [26]:

$$A_{ij}^{*} = \eta_s \pi R \int_{d}^{\infty} (z-h)\phi(z)dz \tag{40}$$

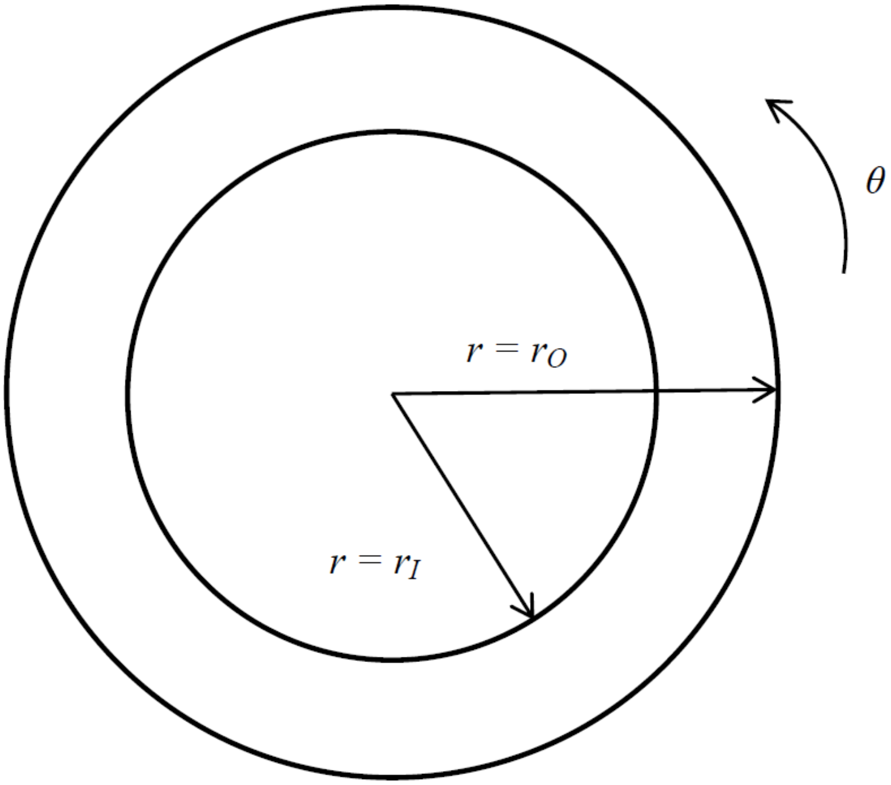

Fig.26 - Simplified drawing of the center plate

The center plate can be regarded as an annulus (see Fig.26), and the area of an annulus can be calculated by using Eq. (41). Since there are 36 pads in one center plate, then the nominal contact area for one pad is given by Eq. (42).

$$A_a = \pi(r_O^2 - r_I^2) \tag{41}$$

$$A_n = \frac{\pi(r_O^2 - r_I^2)}{36} \tag{42}$$

Fig.27 shows the nominal contact area around one point and there are 120 points in the θ direction as we illustrated previously, so that these 120 points can be regarded as 119 nominal contact areas as shown in Fig.27 in the θ direction. Therefore, the nominal contact area around one point can be calculated:

$$A_{ij} = \frac{\pi(r_O^2 - r_I^2)}{36\times 119} \tag{43}$$

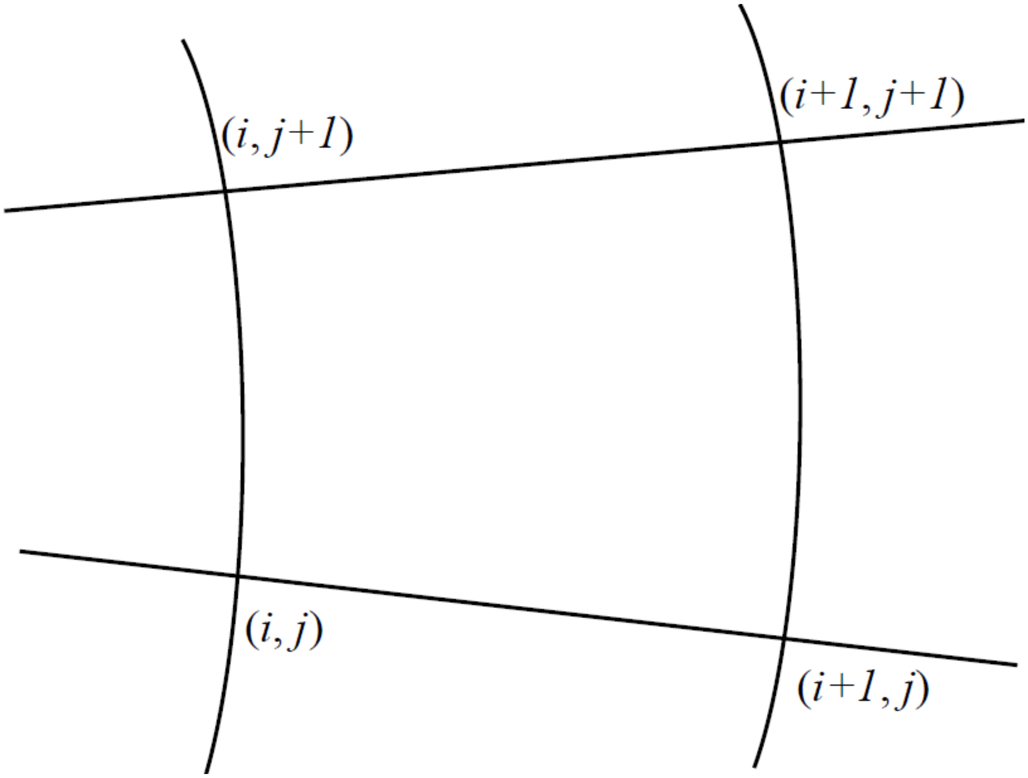

Fig.27 - Nominal contact area around one point

Eq. (44) describes the real contact area around one point. By double summing the real contact area around one point and dividing the nominal contact area of one pad, the contact area ratio can be calculated (shown in Eq. (45)).

$$(A_r)_{ij} = A_{ij}^* \cdot A_{ij} \tag{44}$$

$$A^* = \frac{\sum\sum(A_r)_{ij}}{A_n} \tag{45}$$

The real contact area will later be considered when analyzing the bearing bearings.

4.4 Load Carrying Capacity and Frictional Torque

According to Fig.4, after the solid contact pressure and the fluid pressure are calculated based on Eq. (1) and Eq. (3), the values of the load carrying capacity and the frictional torque from the solid contact and the fluid can be computed. By adding the load carrying capacity and the frictional torque values from the solid contact and the fluid, the total load carrying capacity and the frictional torque for the thrust bearing system can be obtained.

It should be noted that during the calculation of the pressure from the hydrodynamic part, the periodic boundary conditions in θ direction are considered:

$$p(r,\theta_0) = p(r,\theta_1) \tag{46}$$

$$\frac{\partial p}{\partial r}(r,\theta_0) = \frac{\partial p}{\partial r}(r,\theta_1) \tag{47}$$

where θ_0 and θ_1 are angles of the edges of the pad without grooves.

4.4.1 Load carrying capacity and frictional torque from solid contact

According to Eq. (3), the solid contact pressure can be calculated, and the expression of load carrying capacity acting on the periodic center plate generated by the solid contact part is:

$$L_s = \int_{\theta_0}^{\theta_1} \int_{r_i}^{r_o} p_s(r,\theta) r dr d\theta \tag{48}$$

Fig.28 shows the direction of shear stress components, τ_{zr} and $\tau_{z\theta}$, acting on one pad generated by the contact asperities. Since τ_{zr} has no contribution to the solid contact frictional torque, T_s, during the rotation, $\tau_{z\theta}$ (referred as τ_s) is the only shear stress considered when calculating the frictional torque from solid contact. The expression of τ_s has been shown in Eq. (32), and the frictional torque generated by the solid contact, T_s, can be evaluated by the double integral of τ_s:

$$T_s = \int_{\theta_0}^{\theta_1} \int_{r_i}^{r_o} \tau_s(r,\theta) r^2 dr d\theta \tag{49}$$

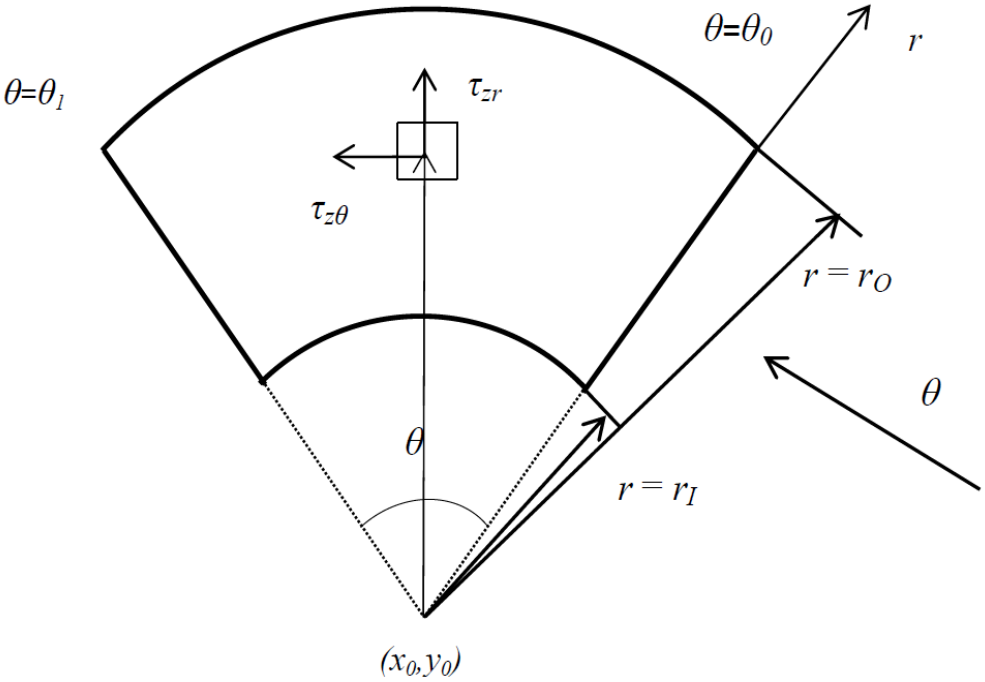

Fig.28 - Shear stress components on the upper casing

4.4.2 Load carrying capacity and frictional torque from fluid

The fluid pressure can be calculated based on Eq. (1). The expression of load carrying capacity acting on the periodic pad generated by the fluid follows the same form as the expression of load carrying capacity generated by the solid contact part:

$$L_f = \int_{\theta_0}^{\theta_1} \int_{r_i}^{r_o} p_f(r,\theta) r dr d\theta \tag{50}$$

Since the lubricant we used is grease, the shear stress from fluid, τ_f, can be calculated by the Herschel-Bulkley model (H-B model) [38] (see Eq. (34)). By double integrating τ_f, the frictional torque generated from the fluid, T_f, can be obtained:

$$T_f = \int_{\theta_0}^{\theta_1} \int_{r_i}^{r_o} \tau_f(r,\theta) r^2 dr d\theta \tag{51}$$

4.4.3 Total Load carrying capacity and frictional torque

The total pressure acting on the pad can be calculated by adding the pressure from the solid contact,p_s, and the fluid, p_f, together and the total load carrying capacity can be calculated according to Eq. (53):

$$p_{total} = p_s + p_f \tag{52}$$

$$L_{total} = \int_{\theta_0}^{\theta_1} \int_{r_i}^{r_o} p_{total}(r,\theta) r dr d\theta \tag{53}$$

After the shear stresses from the solid contact, τ_s, and the fluid, τ_f, are obtained, the total shear stress acting on the pad can be computed by adding these two shear stresses together:

$$\tau_{total} = \tau_s + \tau_f \tag{54}$$

Then the total frictional torque can be evaluated by double integrating the total shear stress, τ_{total}:

$$T_{total} = \int_{\theta_0}^{\theta_1} \int_{r_i}^{r_o} \tau_{total}(r,\theta) r^2 dr d\theta \tag{55}$$

Chapter 5

Results and Analysis for New Bearing Model

5.1 Results with Consideration of Thermal Effects

This chapter shows the results of the indicators of thrust bearing system in this work. The results are based on a coupled model of the mechanical deformation, thermo-elastic deformation, hydrodynamic lubrication, solid contact and grease influence together. It should be noted here that since the surface is deconstructed according to the cut-off frequency, the results shown below are for a specific case when the cut-off frequency, f_c, is 33,300 m^{-1}, and the initial surface separation, h_s is 1 μm. The angular velocity used for the specific case based on an application of this bearing is 0.14 *rad/s* based on an application of this bearing.

Fig.29 shows the film thickness distribution between the center plate and the upper casing, and the film thickness is very small at the boundary of the center plate. Fig.30 shows the temperature distribution of the center plate according to Eq. (39). The temperature is much higher at the boundary of the center plate than at the inside of the center plate.

It is obvious that a thinner local film thickness generates much higher temperature by comparing Figs. 29 and 30. Because there will be more solid contact at local small film thickness and solid contact can generate more friction and heat than fluid shearing, most of the temperature is from the frictional heating.

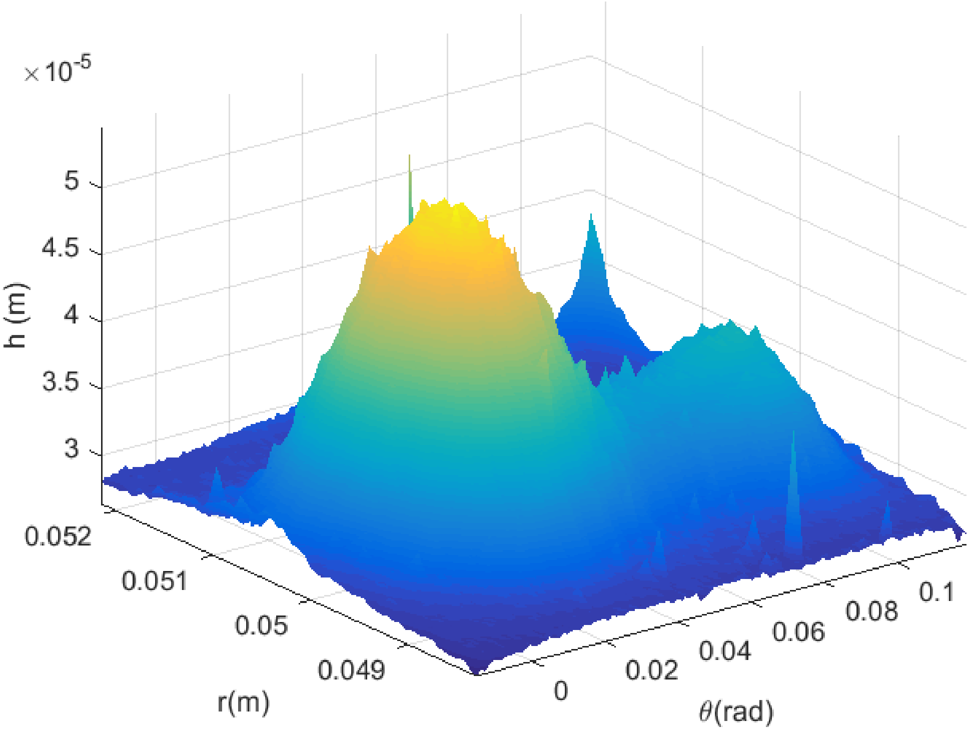

Fig.29 - Film thickness distribution between one pad of the center plate and the upper case (f_c = 33,300 m^{-1}, h_s = 1 μm, ω = 0.14 *rad/s*)

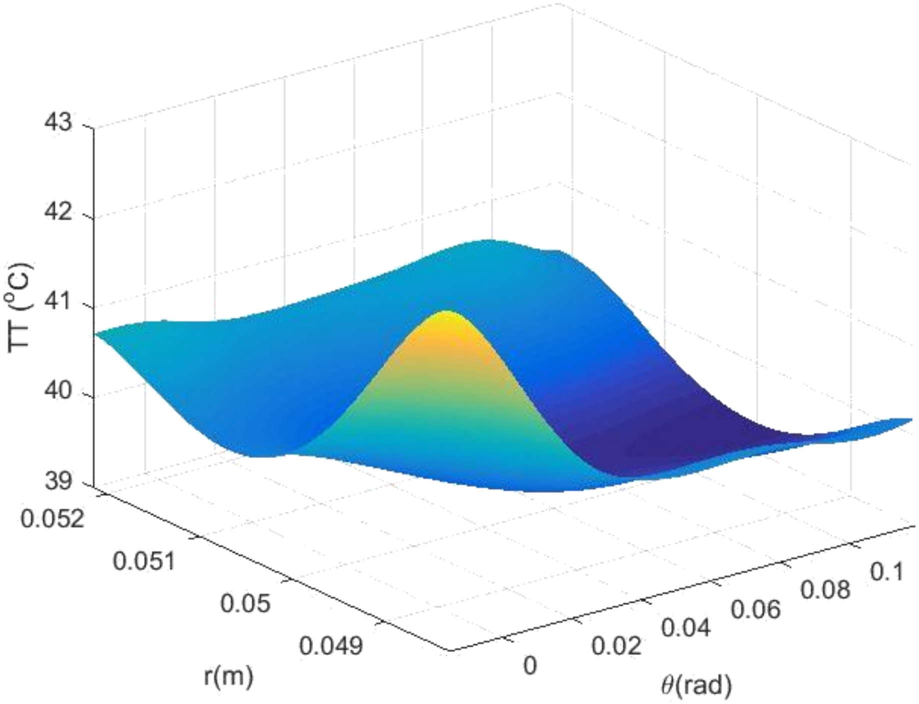

Fig.30 - Temperature distribution on one pad of the center plate (f_c = 33,300 m^{-1}, h_s = 1 μm, ω = 0.14 *rad/s*)

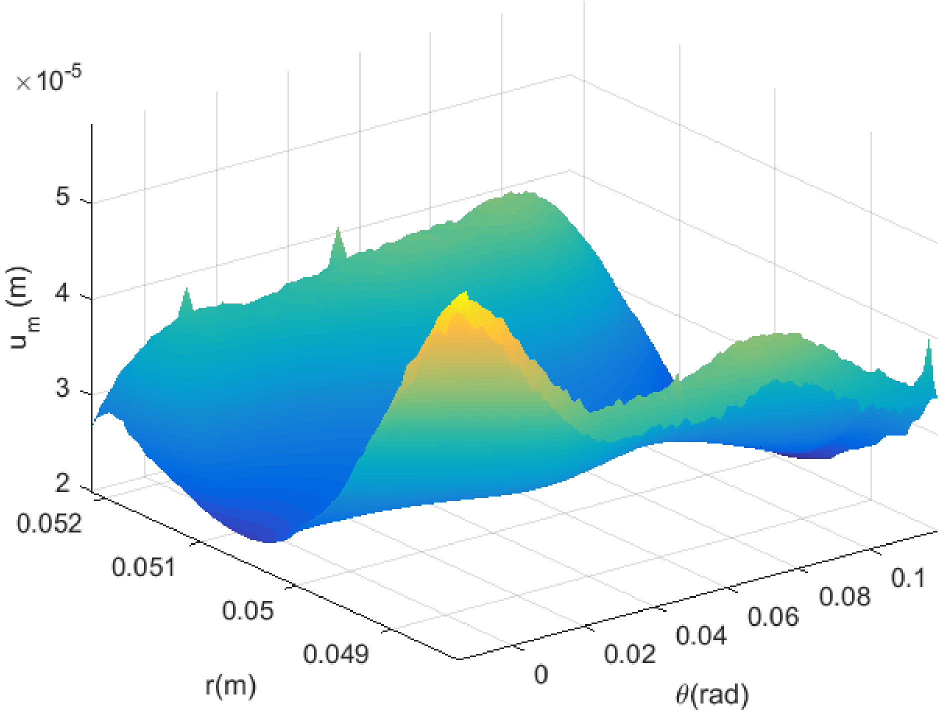

Fig.31- Mechanical deformation of one pad in the center plate (f_c = 33,300 m^{-1}, h_s = 1 μm, ω = 0.14 *rad/s*)

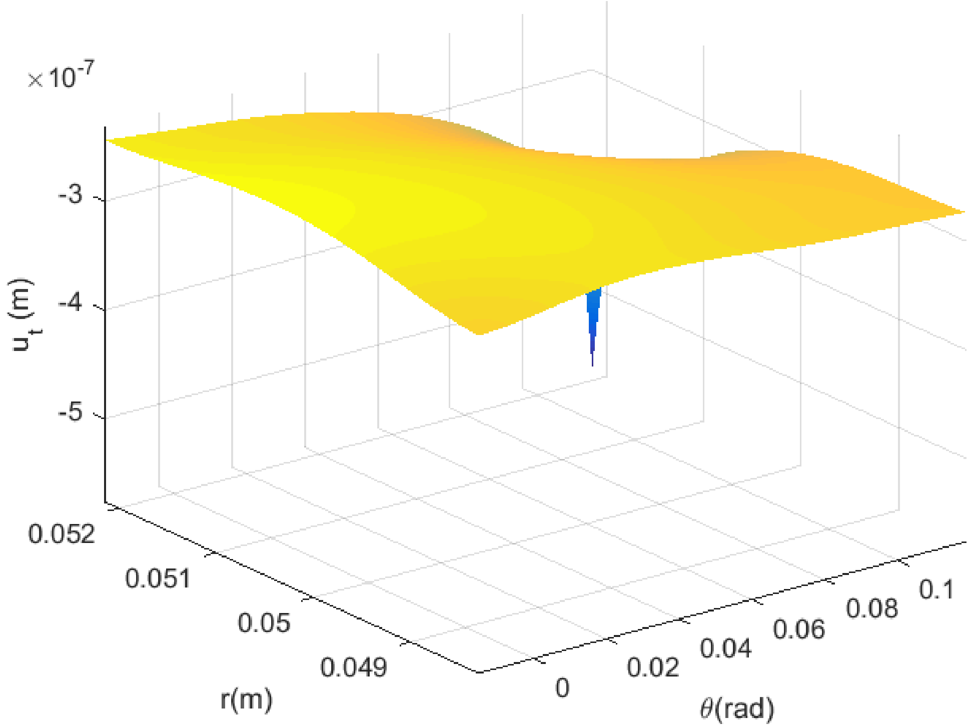

Fig.32 - Thermal deformation of one pad in the center plate (f_c = 33,300 m^{-1}, h_s = 1 μm, ω = 0.14 *rad/s*)

Fig.31 and Fig.32 shows the mechanical deformation calculated based on Eq. (9) and thermal deformation calculated according to Eq. (14), respectively. It can be seen that the mechanical deformation is larger than the thermal deformation which means most of the deformation of the center plate is from the mechanical deformation, and higher mechanical deformations also occurs at thinner local film thickness. More lubricant exists at the locations with thickening local film thickness, so that more lift can be generated by the lubricant to separate two surfaces. Therefore, the lubricant can decrease the mechanical deformation of the center plate.

Fig.33 shows the contact area ratio at each node on the center plate, the boundary has higher contact area ratio which means more real area of contact happens at the boundary. The solid contact pressure distribution, the fluid pressure distribution and the total pressure distribution of the thrust bearing system are shown in Fig.34, Fig.35 and Fig.36. It is obvious that the higher solid contact pressure is generated at the boundary where the contact area ratio is higher by comparing Fig.33 and Fig.36. The pressure from fluid is generated in the inside of the thrust bearing surface based on Fig.35. In addition, most of the total pressure is from solid contact pressure by comparing Fig.34 and Fig.36.

The frictional torque and the load carrying capacity can be calculated according to the total pressure distribution. The results are listed in Table 5. It can be seen from Table 5 that most of the load carrying capacity value and the frictional torque value are from the solid contact.

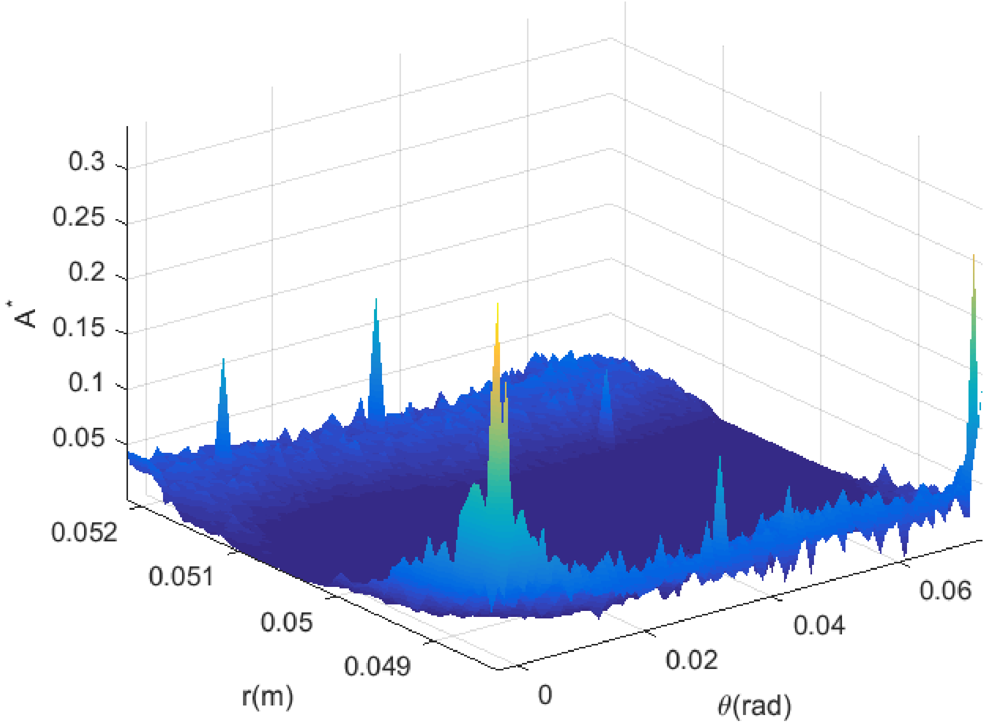

Fig.33 - Contact area ratio at each node on the center plate (f_c = 33,300 m^{-1}, h_s = 1 μm, ω = 0.14 *rad/s*)

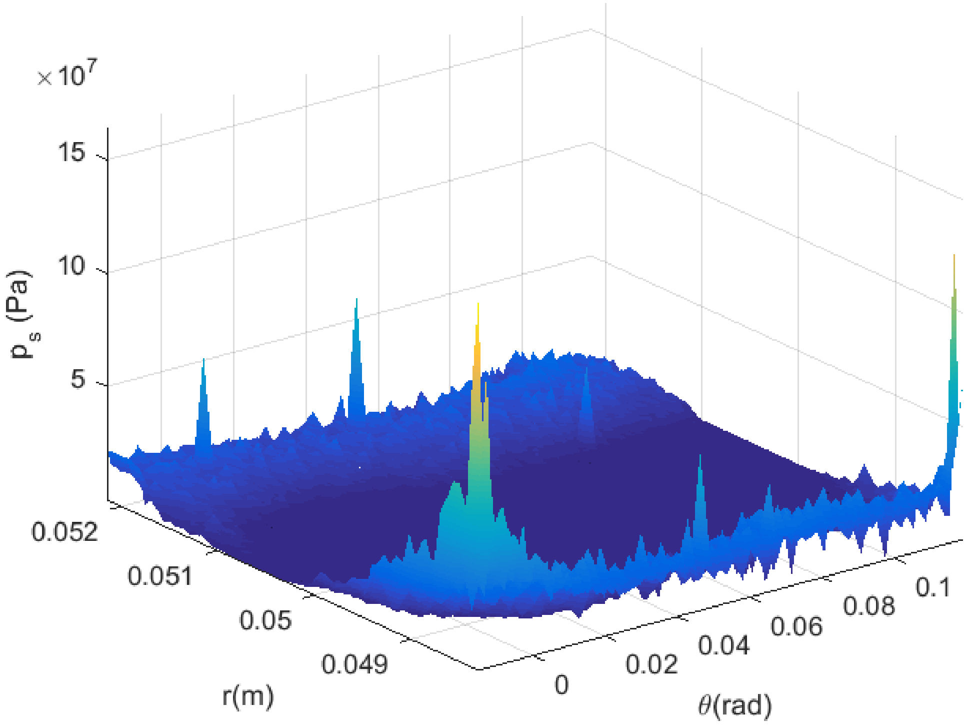

Fig.34 - Pressure distribution generated by the solid contact on the center plate (f_c = 33,300 m^{-1}, h_s = 1 μm, ω = 0.14 *rad/s*)

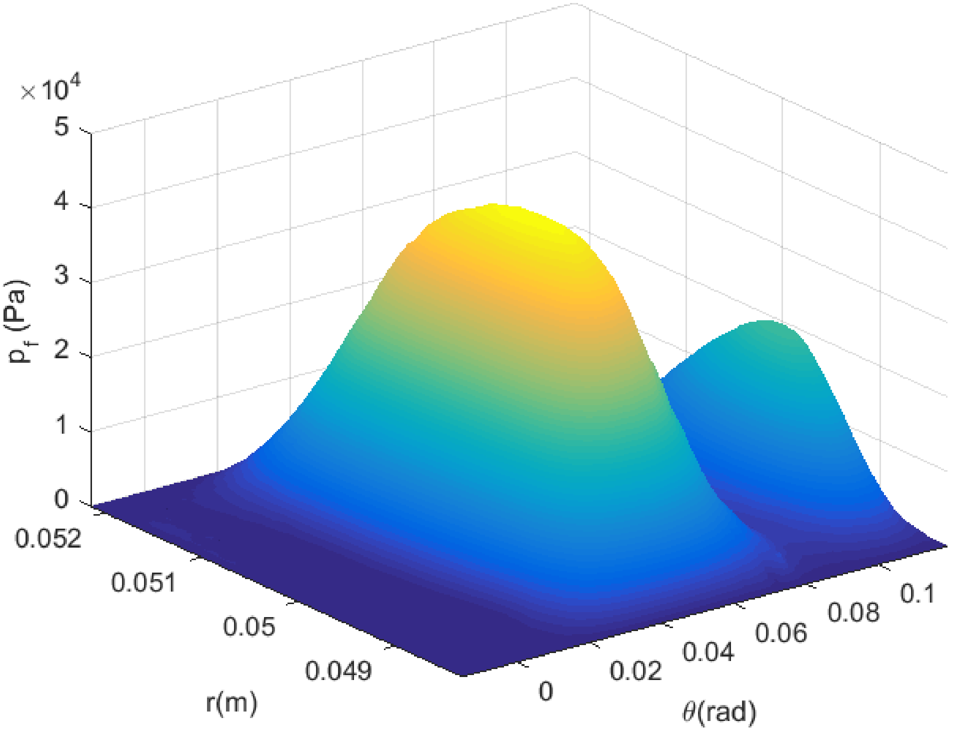

Fig.35 - Pressure distribution generated by the fluid on the center plate (f_c = 33,300 m^{-1}, h_s = 1 μm, ω = 0.14 *rad/s*)

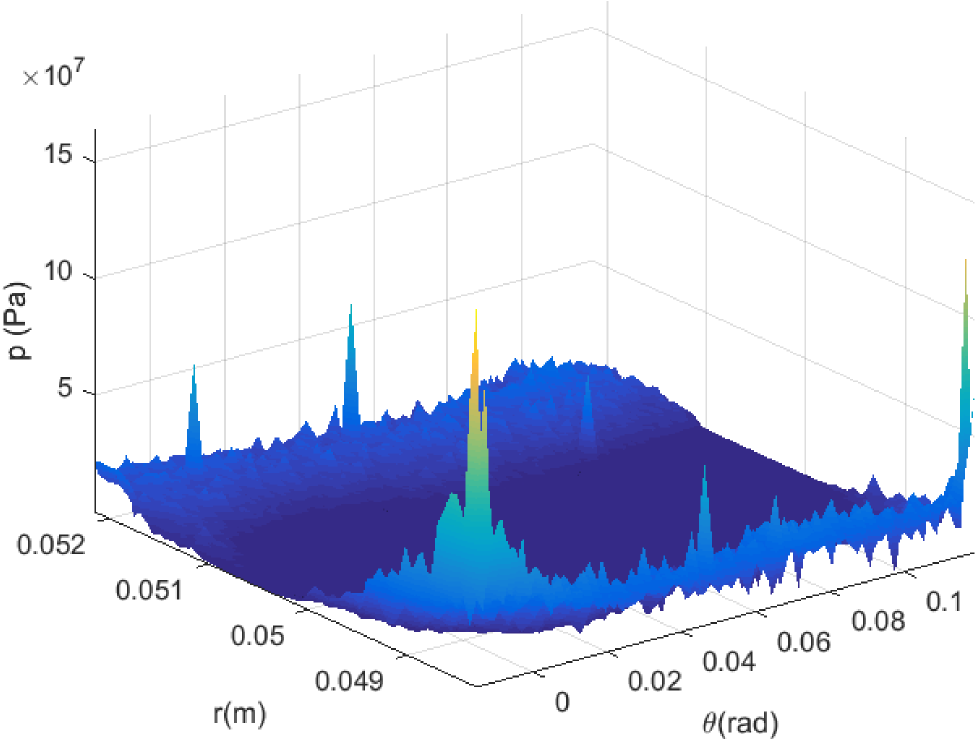

Fig.36 - Total pressure distribution on the center plate (f_c = 33,300 m^{-1}, h_s = 1 μm, ω = 0.14 *rad/s*)

Table 5 - Values of load carrying capacity and the frictional torque with considering thermal (f_c = 33,300 m^{-1}, h_s = 1 μm, ω = 0.14 *rad/s*)

	From solid contact	From fluid shearing	Total	Percentage from solid contact
Load carrying capacity, *L*	5.4496×10^3 *N*	9.9495 *N*	5.4641×10^3 *N*	99.74%
Frictional torque, *T*	7.3754 *N·m*	0.0502 *N·m*	7.4256 *N·m*	99.32%

5.2 Results without Consideration of Thermal Effects

For a better comparison, the results of thrust bearing indicators without thermal effects at the same specific case (f_c = 33,300 m^{-1}, h_s = 1 μm, ω = 0.14 *rad/s*) as considering the thermal effects are also calculated. The calculated process under this situation is shown in Fig.37. It can be found by comparing Fig.4 and Fig.37 that the thermal deflection is neglected when the thermal effects are not considered. Since temperature rise can also influence the viscosity of the lubricant, the temperature influence on the lubricant is also not considered in this situation.

Fig.38 to Fig.43 show the film thickness distribution, the mechanical deformation, the contact area distribution, the pressure distribution from solid contact, the pressure distribution from fluid and the total pressure distribution, separately. All these plots are predicted without considering the thermal effects.

As we concluded in the situation with considering the thermal influence, the mechanical deformation happens at the place where the film thickness is thin based on the Figs. 38 and 39. Fig.40 shows more real area of contact occurs at the boundary.

Meanwhile, the higher pressure is generated at the boundary where the contact area is higher and most of the total pressure is from solid contact pressure, the same phenomena also happen for the situation without considering the thermal effects according to Figs. 40 - 43. The calculated load carrying capacity and frictional torque values for this situation are listed in Table

6. It can also be concluded that most of the load carrying capacity and the friction torque are still generated by the solid contact.

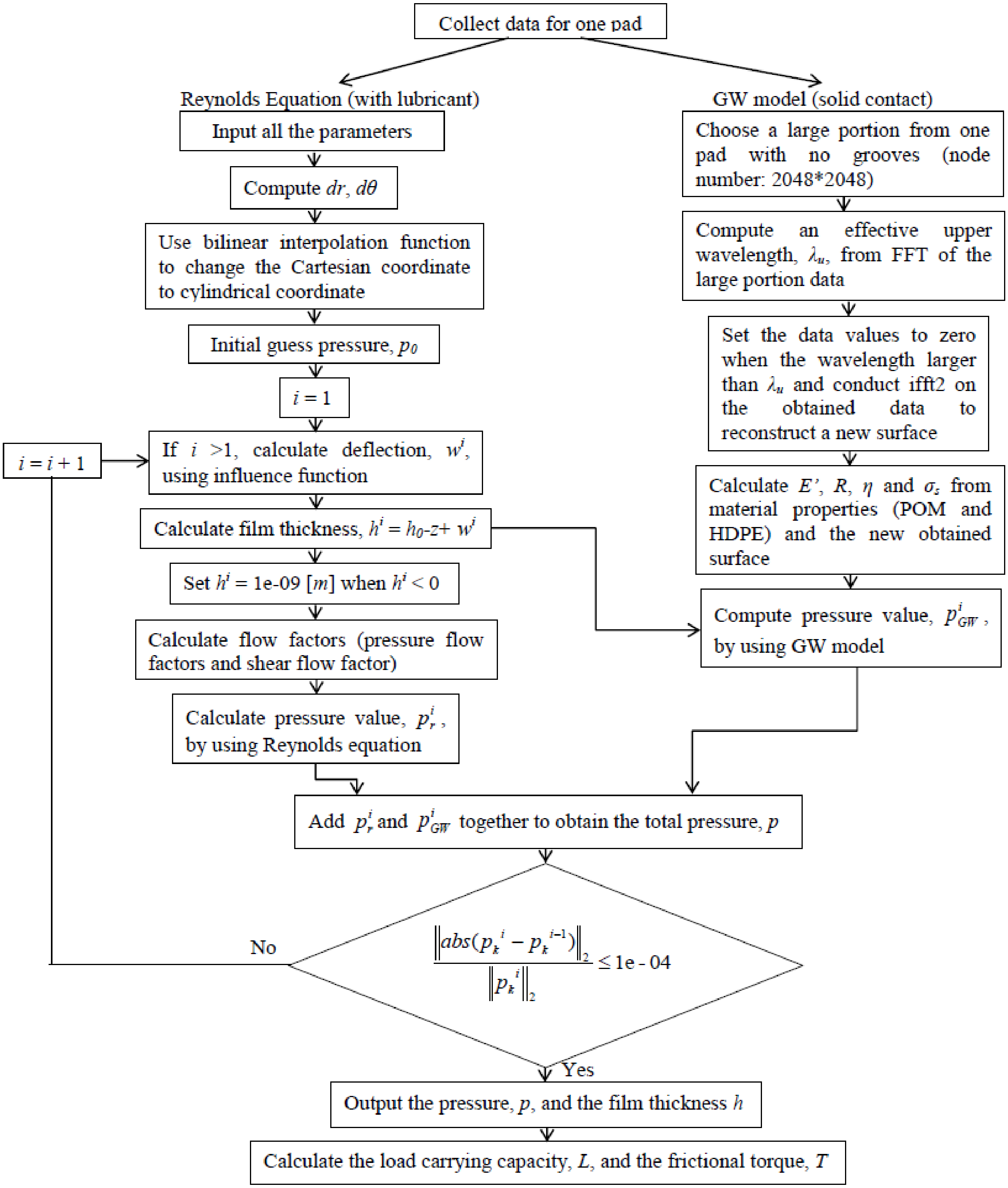

Fig.37 - Flow chart of the mixed lubrication calculation without thermal effects

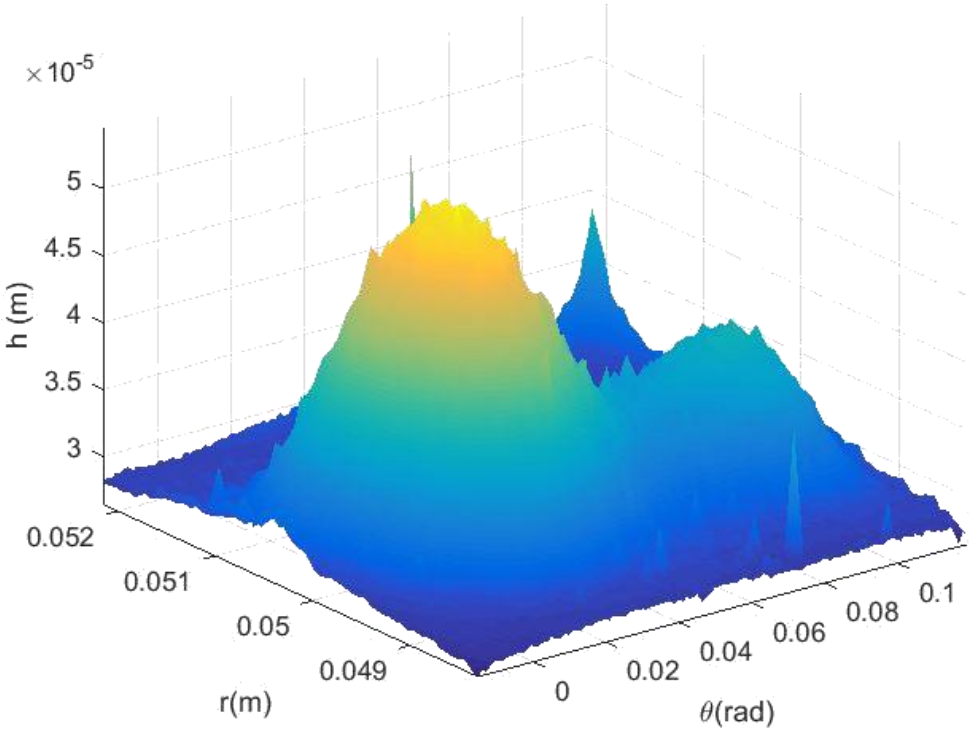

Fig.38 - Film thickness distribution between one pad of the center plate and the upper case without thermal influence (f_c = 33,300 m^{-1}, h_s = 1 μm, ω = 0.14 *rad/s*)

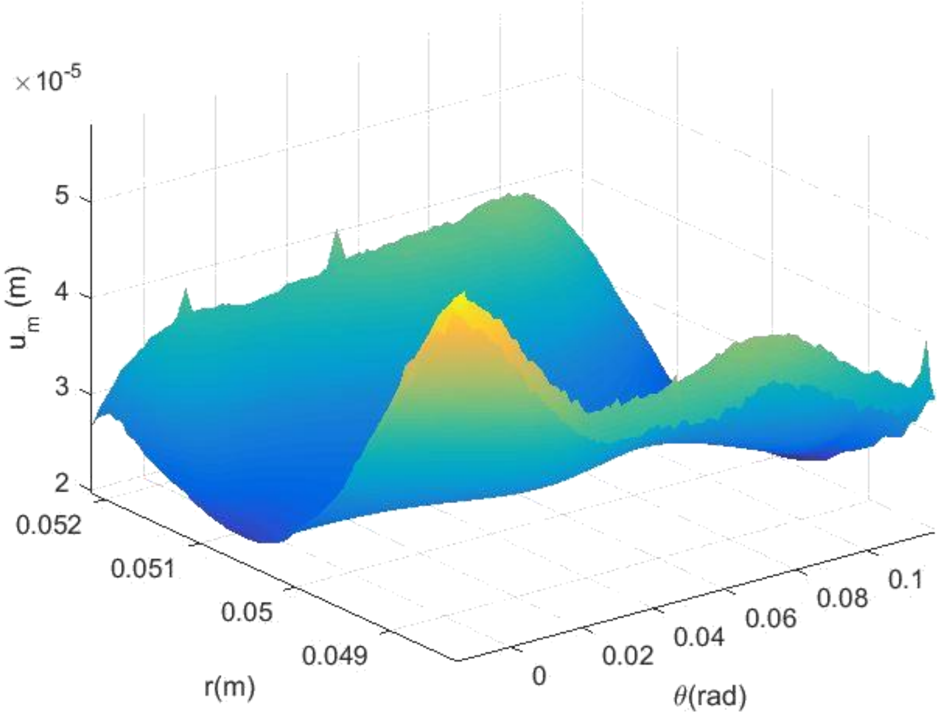

Fig.39 - Mechanical deformation of one pad in the center plate without thermal influence (f_c = 33,300 m^{-1}, h_s = 1 μm, ω = 0.14 rad/s)

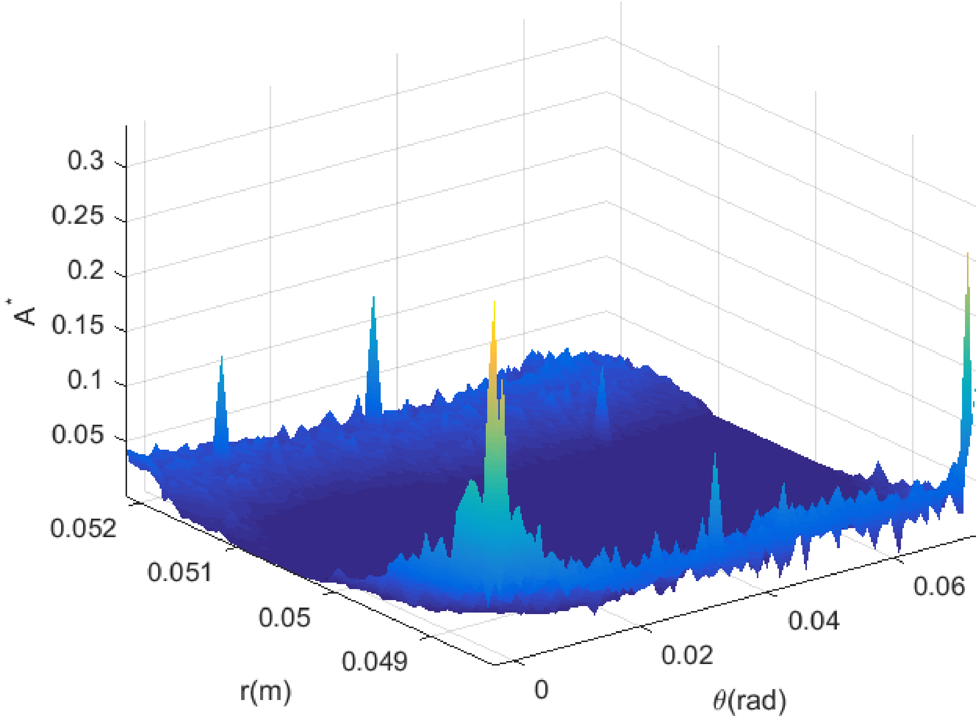

Fig.40 - Contact area distribution of one pad in the center plate without thermal influence (f_c = 33,300 m^{-1}, h_s = 1 μm, ω = 0.14 rad/s)

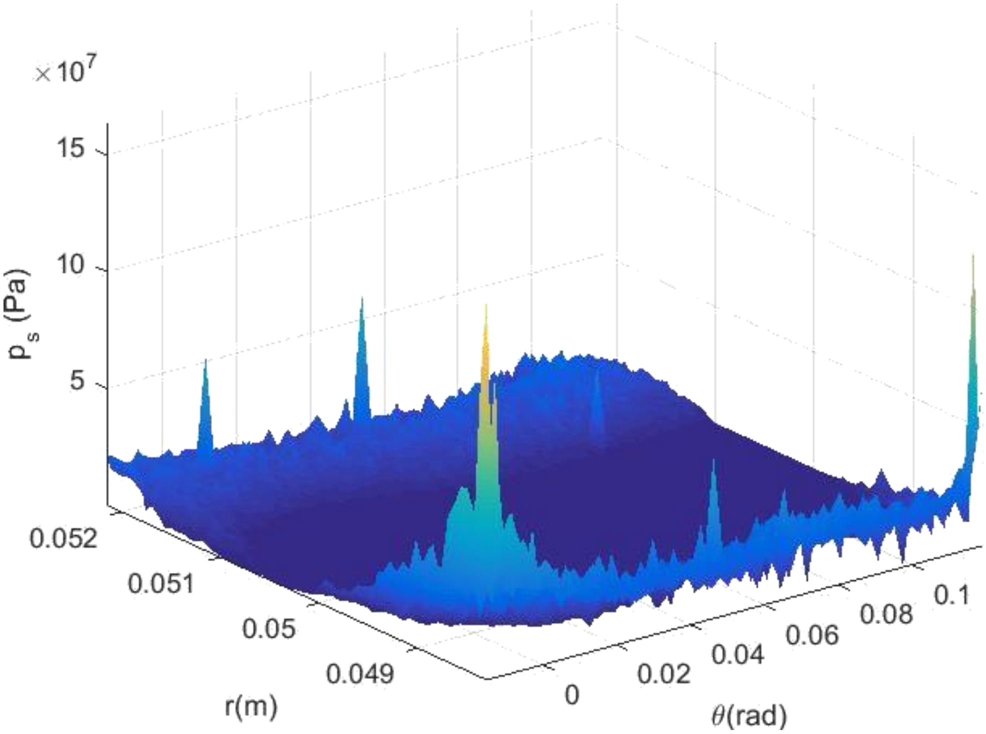

Fig.41- Pressure distribution from solid contact on one pad of the center plate without thermal influence (f_c = 33,300 m^{-1}, h_s = 1 μm, ω = 0.14 *rad/s*)

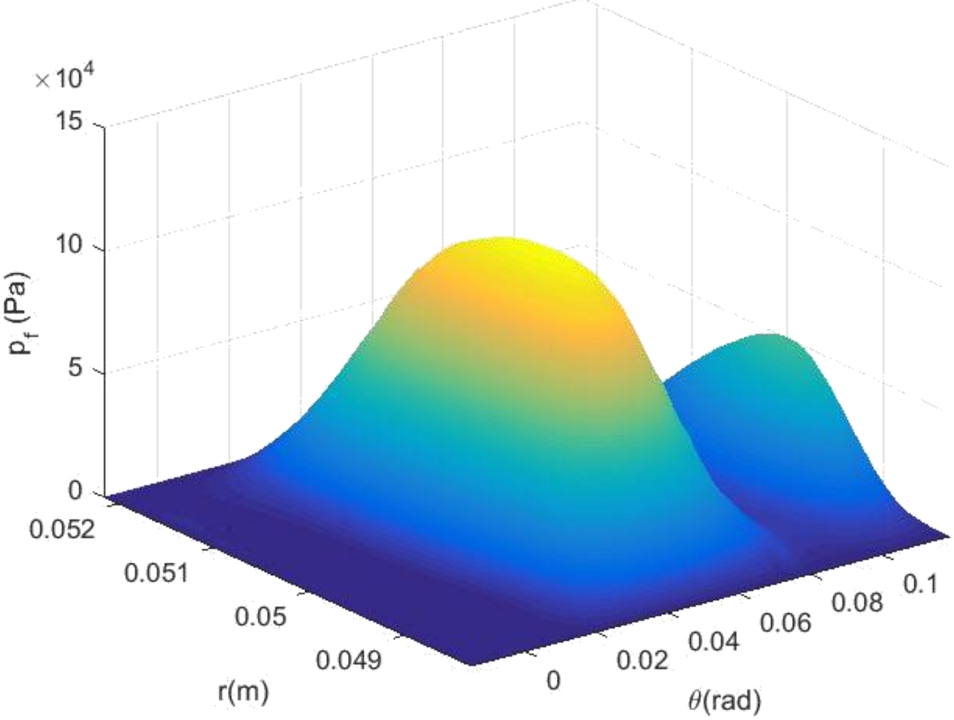

Fig.42 - Pressure distribution from fluid on one pad of the center plate without thermal influence (f_c = 33,300 m^{-1}, h_s = 1 μm, ω = 0.14 *rad/s*)

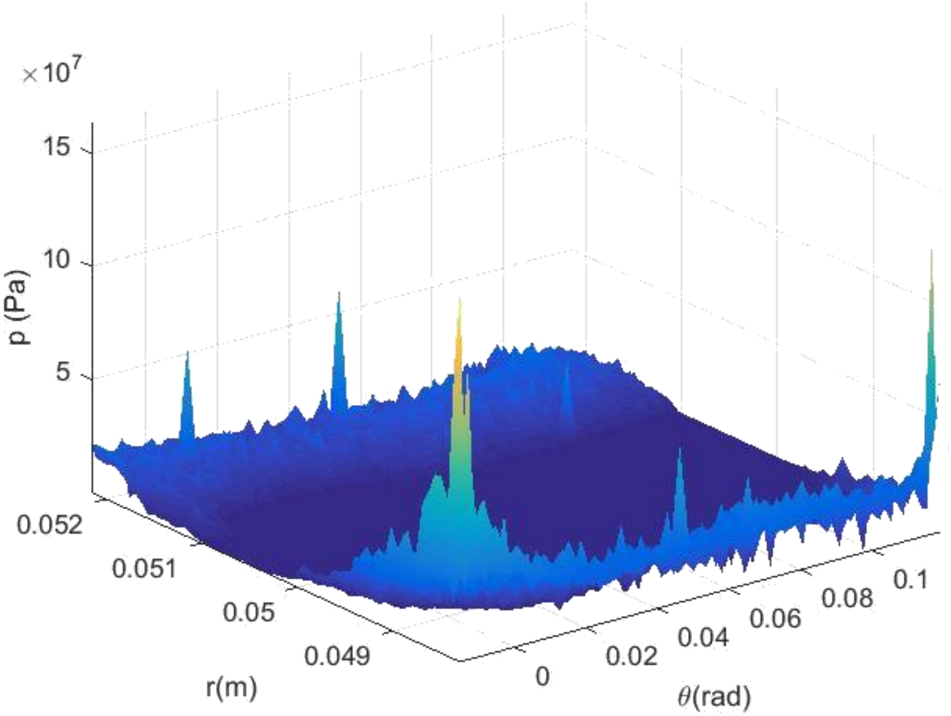

Fig.43 - Total pressure distribution on one pad of the center plate without thermal influence (f_c = 33,300 m^{-1}, h_s = 1 μm, ω = 0.14 *rad/s*)

Table 6 - Values of load carrying capacity and the frictional torque without considering thermal effects (f_c = 33,300 m^{-1}, h_s = 1 μm, ω = 0.14 *rad/s*)

	From solid contact	From fluid shearing	Total	Percentage from solid contact
Load carrying capacity, *L*	5.3963×10^3 *N*	26.2716 *N*	5.4231×10^3 *N*	99.51%
Frictional torque, *T*	7.3028 *N·m*	0.0918 *N·m*	7.3946 *N·m*	98.76%

5.3 Comparison of the Results with and without Considering Thermal Effects

For a better comparison of these two situations with and without considering thermal effects, the relationship between the minimum film thickness (h_{min}) and the contact area ratio (A^*), the load carrying capacity (L_{total}), the frictional torque (T_{total}), and the ratio for the contribution of the fluid part and the solid contact part on the load carrying capacity and the frictional torque with the same initial surface separation (h_s = 1 μm) are studied. The results are plotted in Figs. 44 to 48.

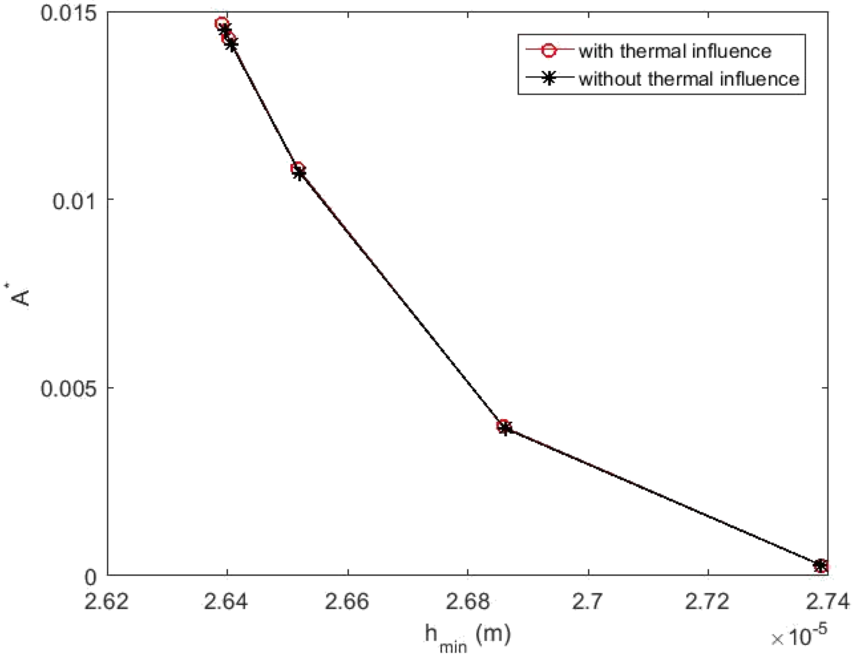

Fig. 44 - Relationship between the minimum film thickness (h_{min}) and the contact area ratio (A^*) for the situations with and without considering thermal influence

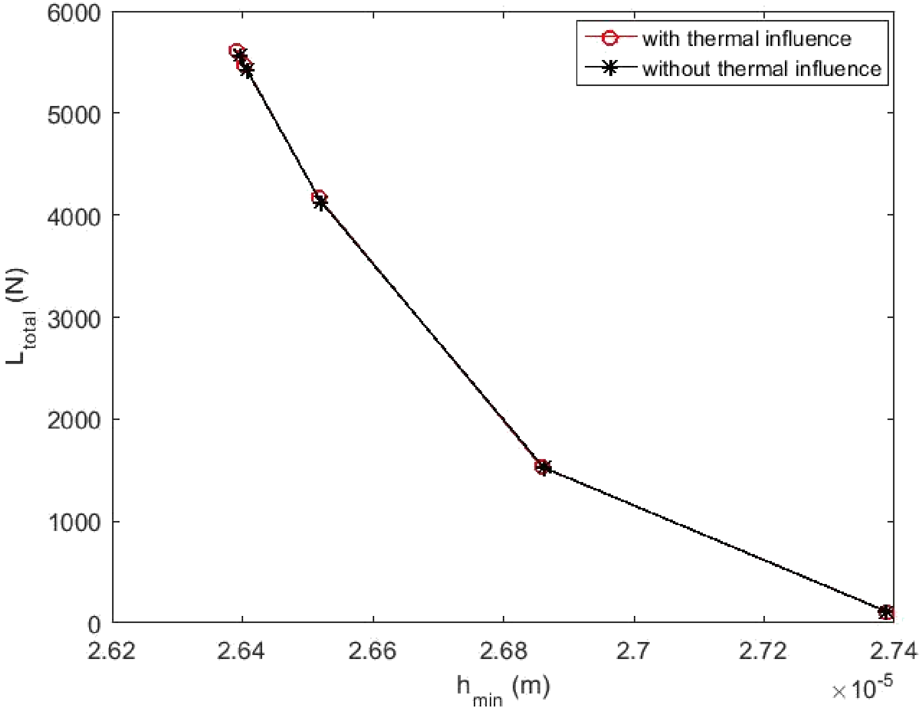

Fig.45 - Relationship between the minimum film thickness (h_{min}) and the load carrying capacity (L_{total}) for the situations with and without considering thermal influence

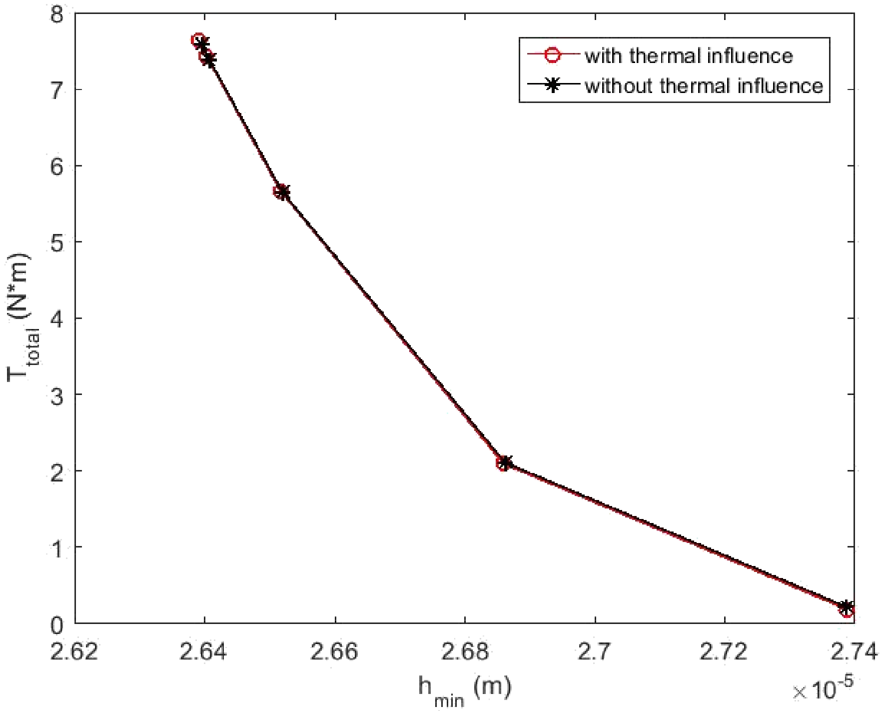

Fig.46 - Relationship between the minimum film thickness (h_{min}) and the frictional torque (T_{total}) for the situations with and without considering thermal influence

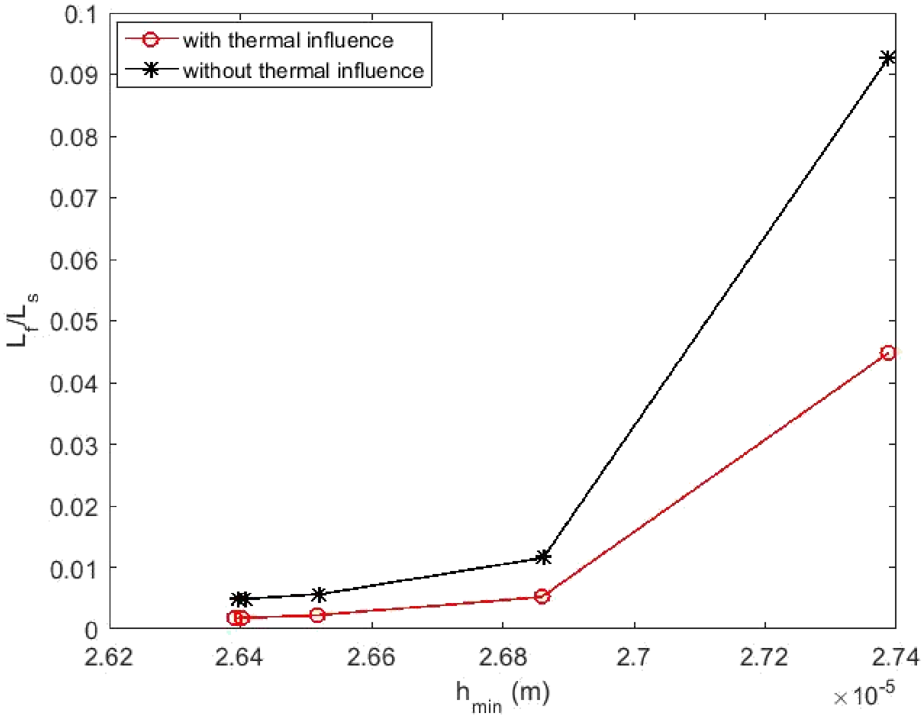

Fig.47 - Relationship between the minimum film thickness (h_{min}) and the ratio of the load carrying capacity from fluid (L_f) and the load carrying capacity from solid contact (L_s)

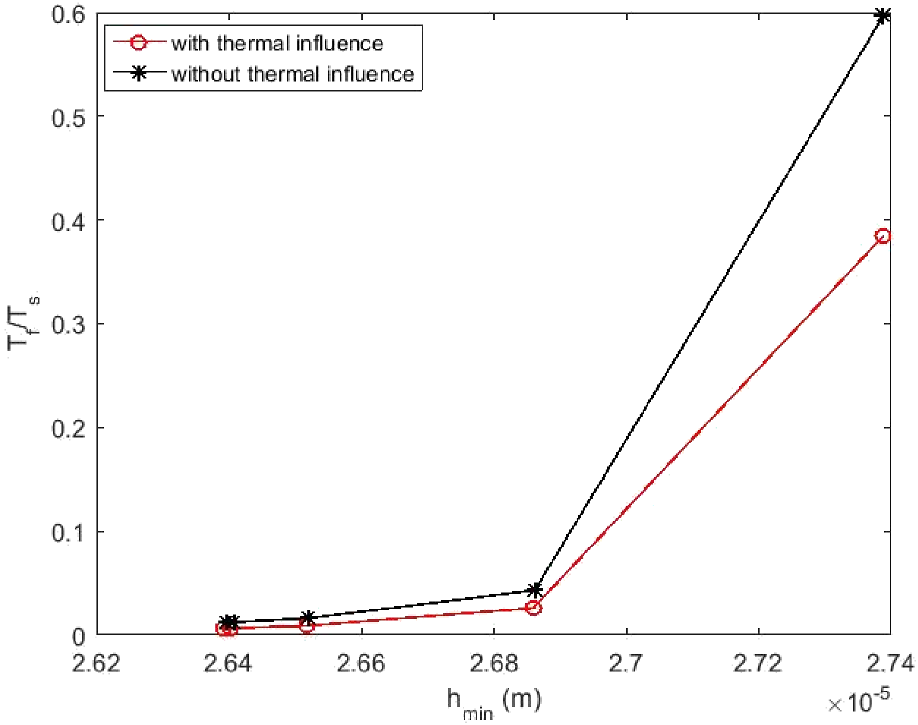

Fig.48 - Relationship between the minimum film thickness (h_{min}) and the ratio of the frictional torque from fluid (T_f) and the frictional torque from solid contact (T_s)

5.4 Results and Discussions

It can be concluded from the Figs. 45 and 46 that the difference between the total load carrying capacity and the total frictional torque for the situations with and without considering the thermal influence are very small (the angular velocity considered here is $\omega = 0.14$ *rad/s*). According to the trend lines in Figs. 47 and 48, the proportions of the load carrying capacity and the frictional torque from fluid decrease when the thermal effects are considered during the analysis. This is because the temperature in the thrust bearing system will increase when the thermal effects are considered, which will make the viscosity of the lubricant becomes lower. Therefore, the lift force between two surfaces will become smaller and more solid contact will happen.

Yu and Sadeghi [18] concluded that thermal effects can reduce the load carrying capacity and the frictional torque. However, the total load carrying capacity and the total frictional torque do not change too much when considering the thermal effects and the thermal effects only reduce the load carrying capacity and the frictional torque from fluid. Perhaps this is because the angular velocity considered here is very low and the thrust bearing is in the mix lubrication regime, most of the load carrying capacity and the frictional torque are carried by the solid contact. In the work of Yu and Sadeghi, the bearing they considered is under the hydrodynamic regime and the load carrying capacity value and the frictional torque value are all generated by the fluid.

The angular velocity is also increased in this work (which will be discussed in Chapter 7), the thrust bearing will tend to be a hydrodynamic bearing with the increase of the angular velocity and more load carrying capacity and the frictional torque will be carried by the fluid. Then the changing trend of the load carrying capacity and the frictional torque will probably become closer to the analysis of Yu and Sadeghi. Otherwise, the lubricant they used is not the same as what we used in our experiment, which will also make different changes of the total load carrying capacity and the total frictional torque.

5.5 Conclusions

In this part, a mixed lubrication thermo-elastic model of a sectored thrust bearing is created. This model is able to provide predictions of important quantities such as frictional torque, load carrying capacity, minimum film thickness, temperature rise, contact pressure. However, this model requires further development verification with the experimental results and the results from the other existed models.

In addition, for a thrust bearing system under the mixed lubrication regime, more solid contact will happen when considering the thermal effects and the thermal effects can reduce the load carrying capacity and the frictional torque from fluid when the angular velocity of the thrust bearing system is small.

Furthermore, the code we programmed for the model can also be used to investigate the influence of various design parameters on thrust bearing performance.

CHAPTER 6

SURFACE CHARACTERIZATION

In Chapter 4, a new thrust bearing model is established and the results are analyzed in Chapter 5. Even with the existence of the lubricant between two surfaces during the rotation of thrust bearings, surface asperities can still come into contact to influence the performance of the thrust bearings. Therefore, the characterization of the rough surface is very important in studying the thrust bearing system. This chapter focuses more on the surface characterization.

6.1 Measured Surface Fractal Characterization

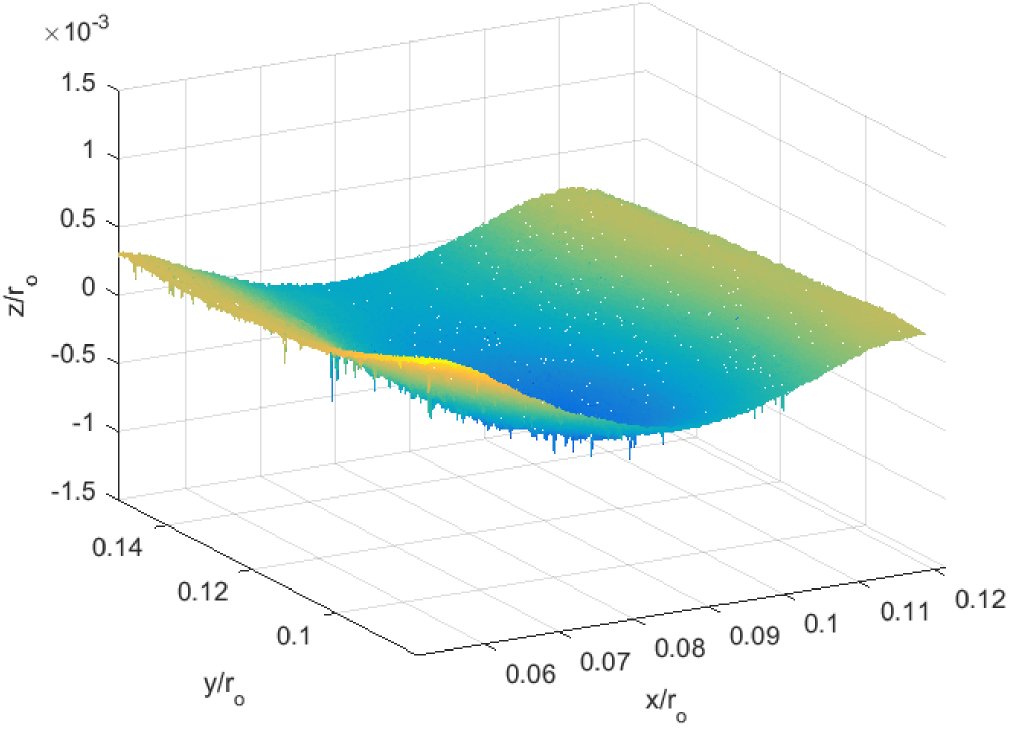

Fig.49 - Rough surface with 2048 × 2048 nodes from thrust bearing

In this chapter, the rough surface of a single pad with 2048×2048 nodes (46.54% of the refined pad surface) is chosen from the refined pad surface (see Fig.17) as shown in Fig.49 (the coordinate values are normalized by the outer radius value of the thrust bearing (r_o)), and the surface data is leveled to make sure the average slope of the surface is zero before calculating the surface parameters. The reason we choose 2048×2048 nodes on the measured surface is that the Fast Fourier transform (FFT) method will be used in the analysis, it is the most efficient when the number of samples is a power of 2. In addition, other common statistical parameters, like root mean square roughness (R_q), skewness (Sk) and kurtosis (K) as in Table 3 are also calculated for the chosen rough surface.

Since this chapter is only considered the fractal characterization, the thermal influence is not considered for the simplification. The calculation process is the same as shown in Fig.37.

The 1-D roughness-length method is used to calculate the fractal dimension of surface profiles in our previous work [32, 33]. The 3-D roughness-length method [34] (as we illustrated in Chapter 2) is used here to calculate the fractal dimension value of the measured rough surface (see Eq. (16)). Fig.50 shows the plot of the roughness-length method [34] in calculating the fractal dimension value. The calculated fractal dimension value is also listed in Table 9.

As discussed in Chapter 4, the same mapping process and the surface deconstruction process are conducted on the measured surface shown in Fig.49. Then the film thickness, the mechanical deformation, the contact area distribution, the solid contact pressure, the fluid pressure and the total pressure of the measured surface for the specific case (when the cut-off frequency $f_c = 33{,}300\ m^{-1}$, the initial surface separation is $h_s = 1\ \mu m$ and the angular velocity $\omega = 0.14\ rad/s$) is obtained.

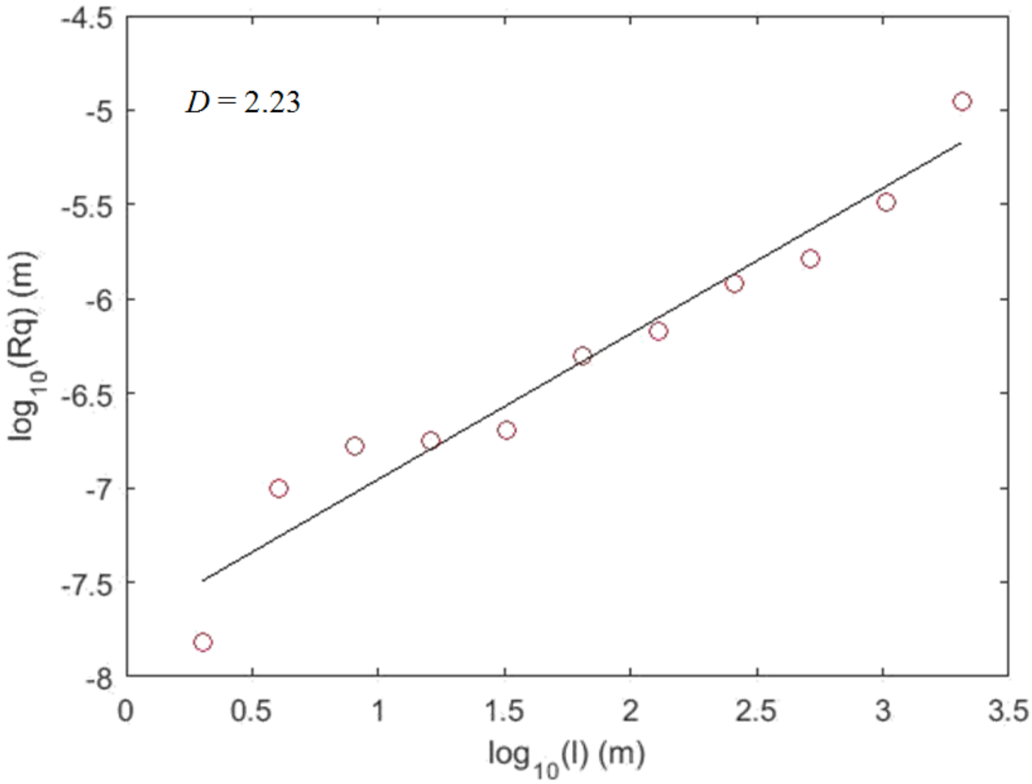

Fig.50 - Plot of the roughness-length method in calculating fractal dimension value for the measured surface

Fig.51 shows the film thickness distribution between the center plate and the upper casing, the film thickness in the inside of the rough surface is larger than that at the boundary. Fig.52 shows the mechanical deformation of the center plate and Fig.53 shows the contact area ratio of each node on the center plate. It can be found that the larger the mechanical deformation is, the higher the contact area ratio happens by comparing Fig.52 and Fig.53.

The solid contact pressure distribution, the fluid pressure distribution and the total pressure distribution are shown in Fig.54, Fig.55 and Fig.56. According to these three figures, most of the pressure is carried by the solid contact, and the larger pressure values occur at the boundary. After the pressure and shear stress are obtained, the frictional torque and load carrying capacity of the thrust bearing can be calculated which listed in Table 7. It reveals that most of the load carrying capacity value and the total frictional torque value are from the solid contact.

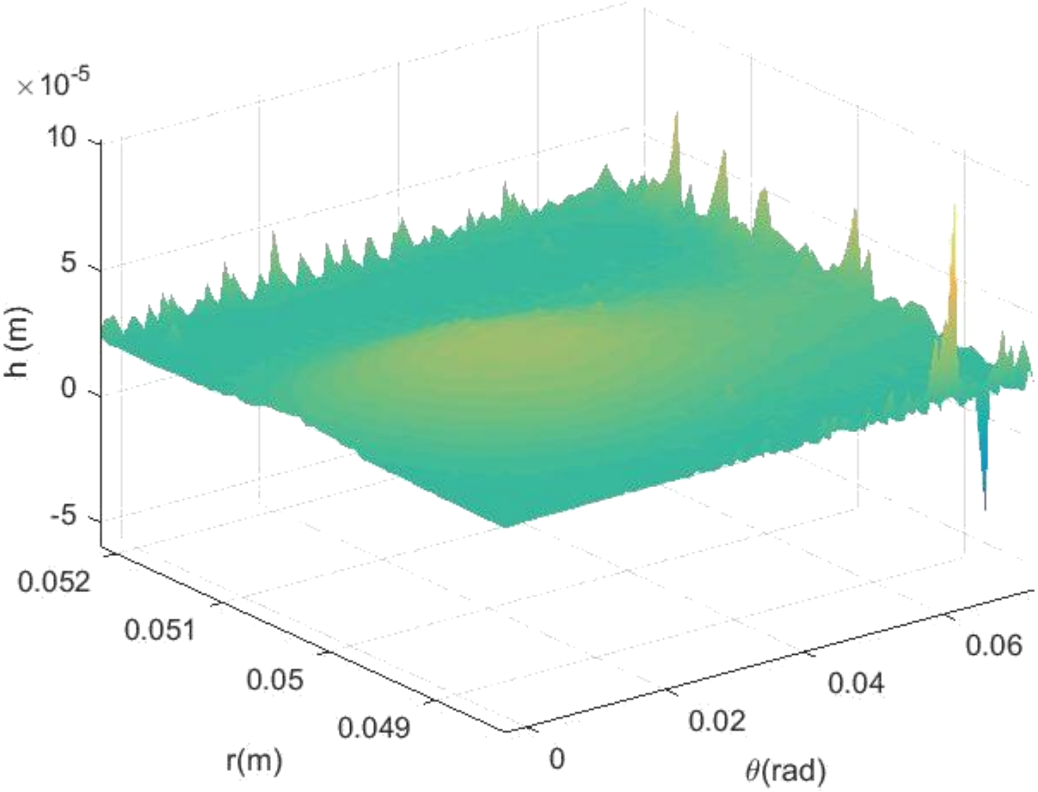

Fig.51 - Film thickness between the measured surface and the upper casing (f_c = 33,300 m^{-1}, h_s = 1 μm, ω = 0.14 *rad/s*)

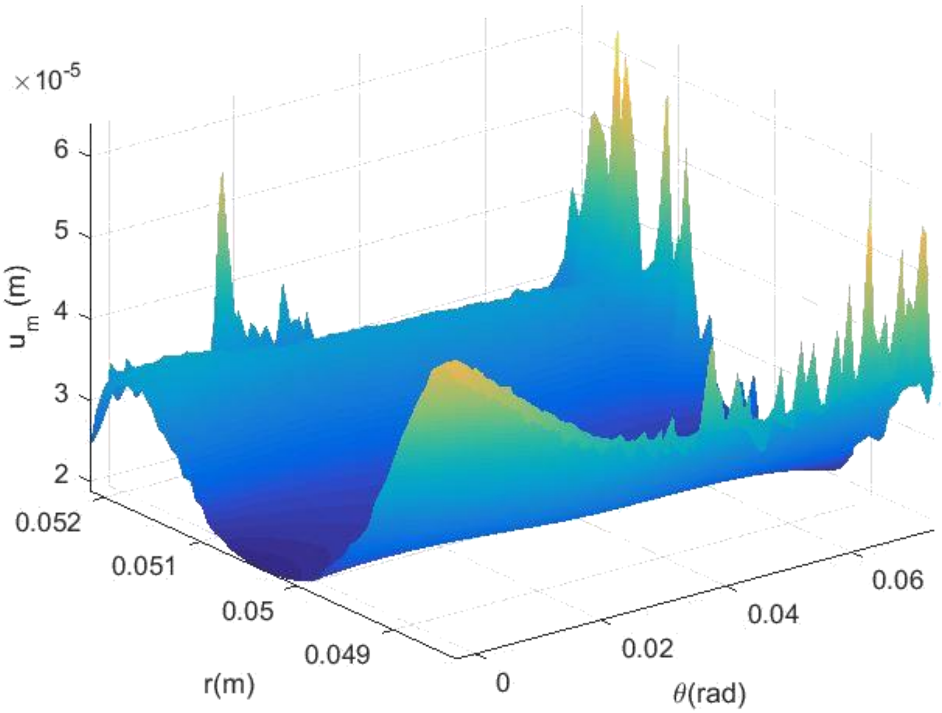

Fig.52 - Mechanical deformation of the measured surface (f_c = 33,300 m^{-1}, h_s = 1 μm, ω = 0.14 *rad/s*)

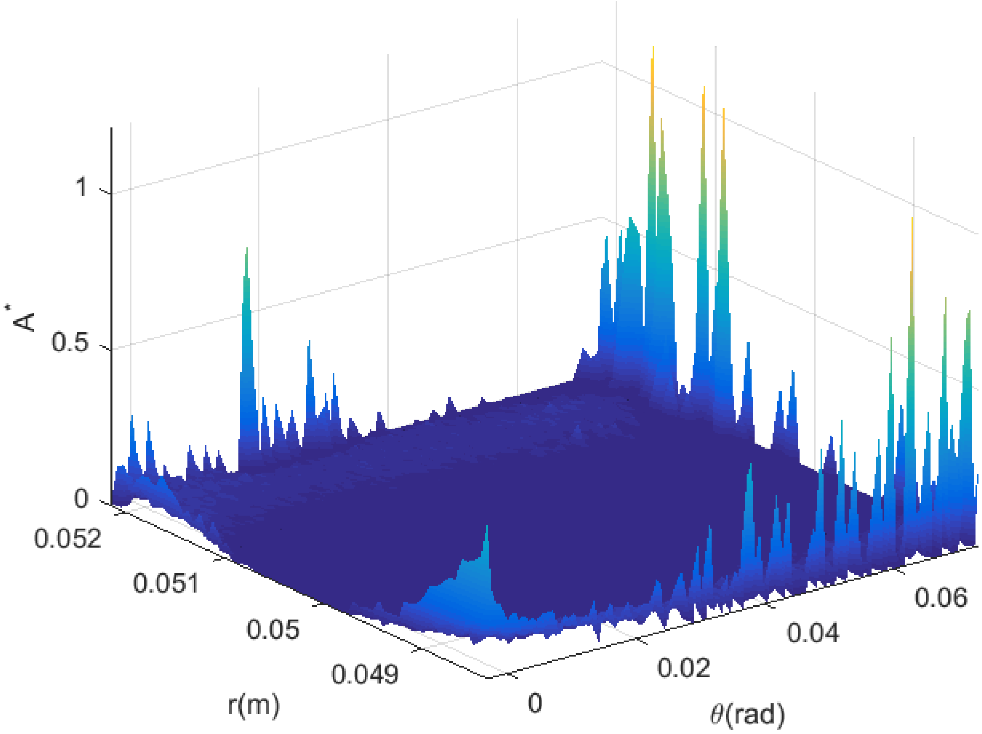

Fig.53 - Contact area ratio on each node of the measured surface (f_c = 33,300 m^{-1}, h_s = 1 μm, ω = 0.14 *rad/s*)

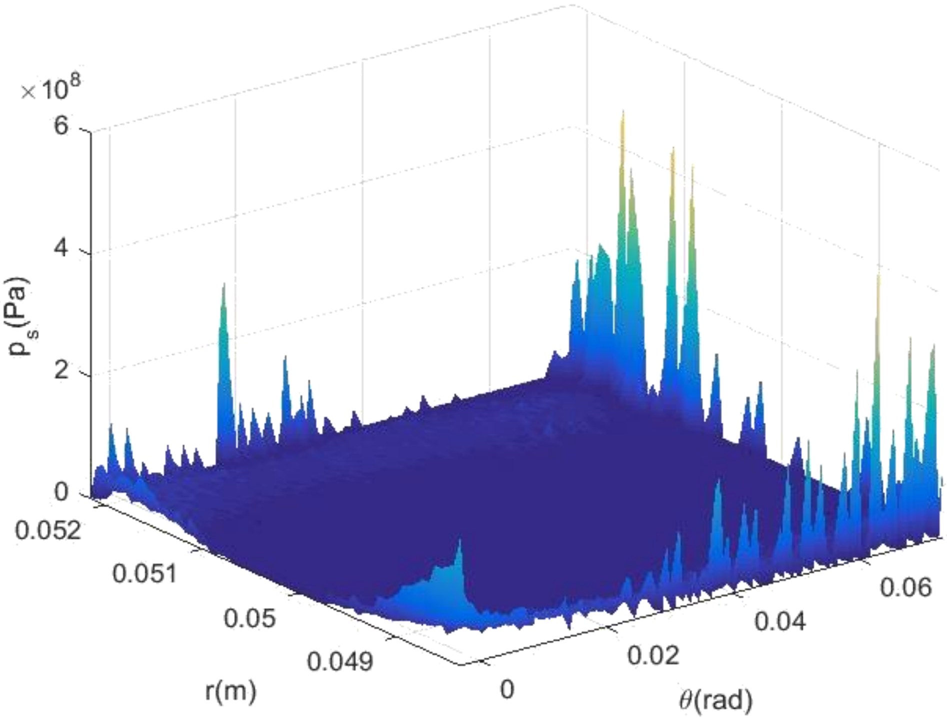

Fig.54 - Solid contact pressure distribution on the measured surface (f_c = 33,300 m^{-1}, h_s = 1 μm, ω = 0.14 *rad/s*)

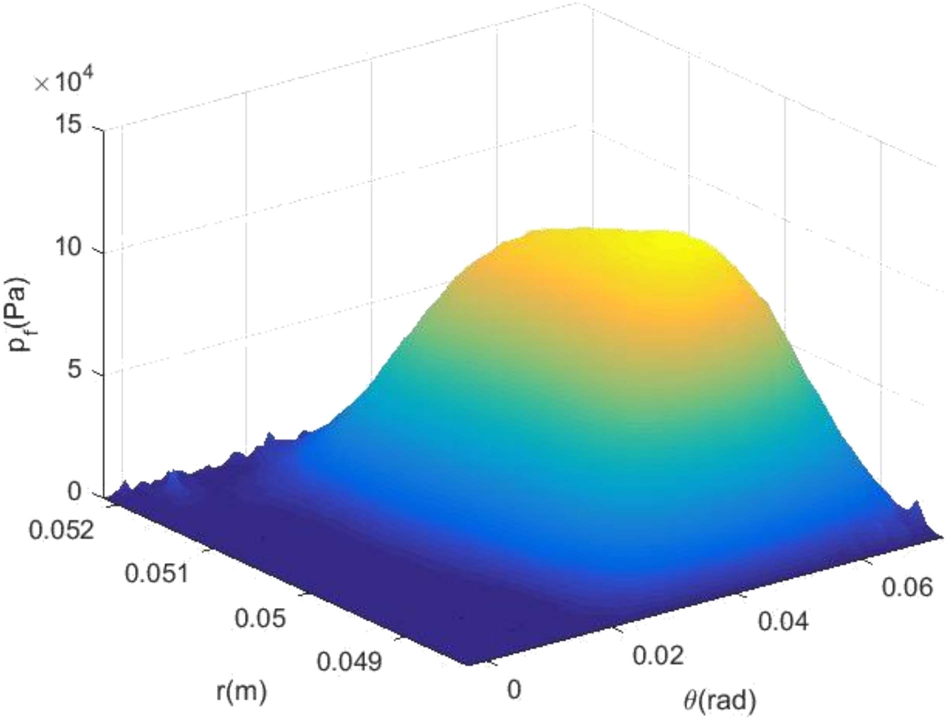

Fig.55 - Fluid pressure distribution on the measured surface (f_c = 33,300 m^{-1}, h_s = 1 μm, ω = 0.14 *rad/s*)

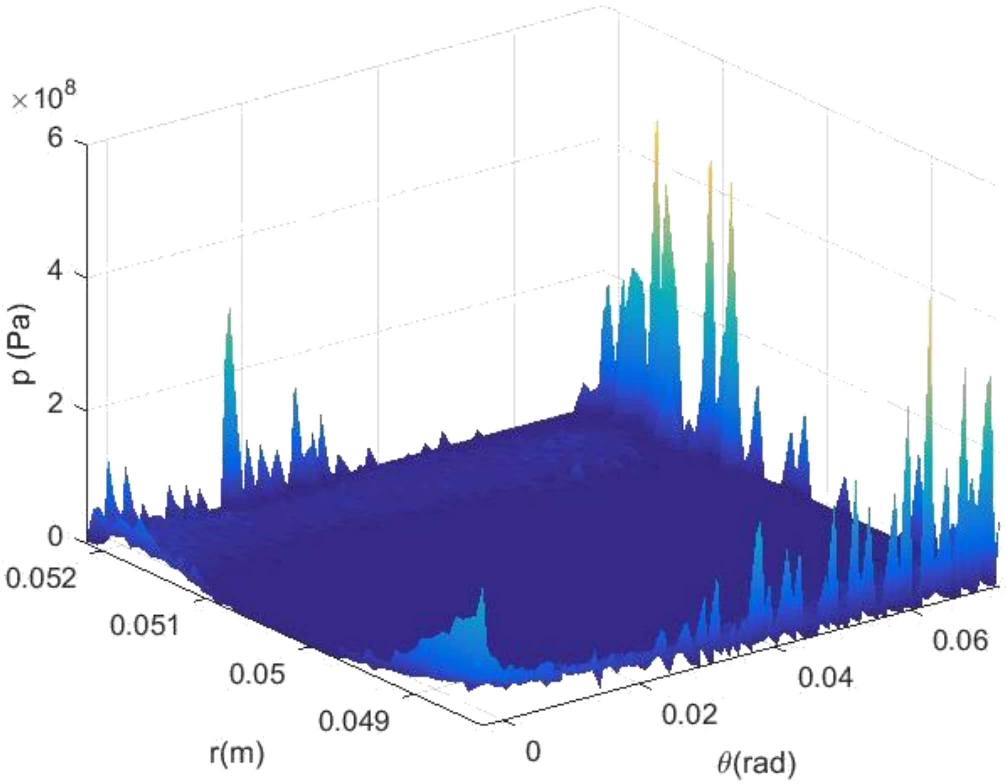

Fig.56 - Total pressure distribution on the measured surface (f_c = 33,300 m^{-1}, h_s = 1 μm, ω = 0.14 *rad/s*)

Table 7 - Values of the load carrying capacity and the frictional torque for the measured surface (f_c = 33,300 m^{-1}, h_s = 1 μm, ω = 0.14 *rad/s*)

	From solid contact	From fluid shearing	Total	Percentage from solid contact
Load carrying capacity, *L*	3.3039×10^3 *N*	17.5720 *N*	3.3301×10^3 *N*	99.21%
Frictional torque, *T*	4.4741 *N·m*	0.0545 *N·m*	4.5286 *N·m*	98.80%

6.2 Surface Generation Methods

Two different methods are used to artificially generate rough surfaces with the same fractal dimension calculated from the measured rough surface. One is the 3D PSD-iFFT method, which is short for the inverse Fourier transform based on a prescribed Power Spectral Density. The other one is the midpoint displacement method, which can be abbreviated as MDM. The fractal dimension value used to generate the surface is 2.23.

6.2.1 3D PSD-iFFT method

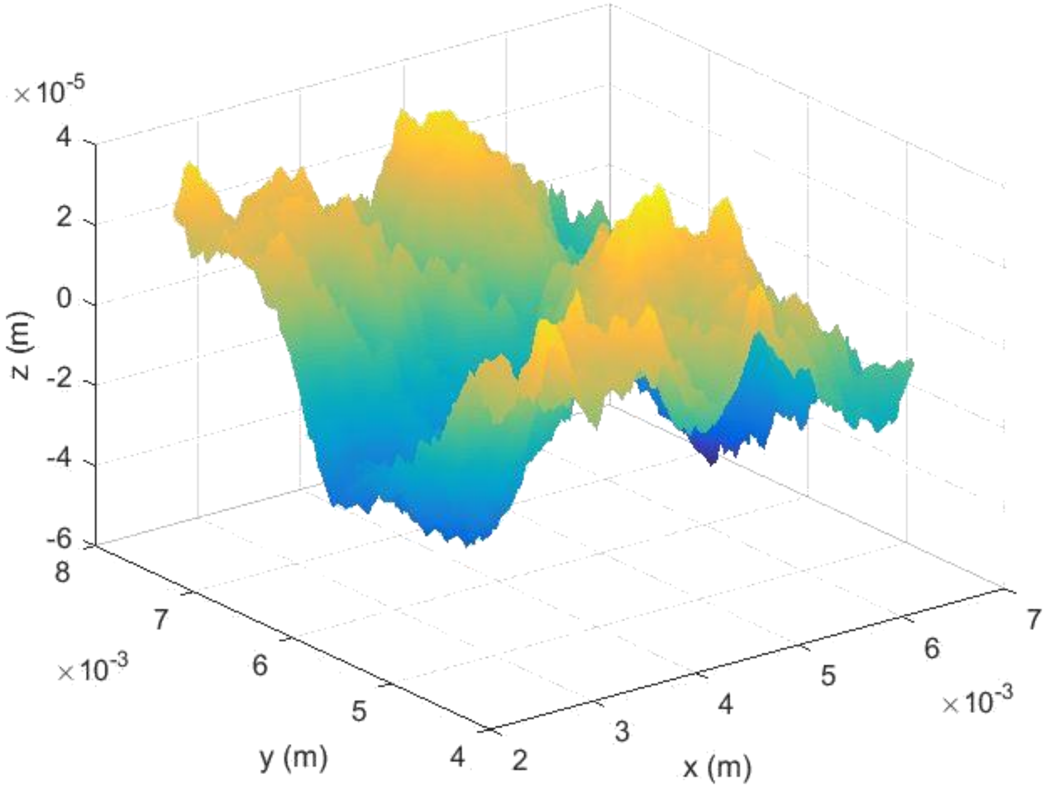

Fig.57 - Surface generated by using Eq. (52)

According to Hu and Tonder [40], the surface topographies *z*(*x*,*y*) can be generated with a power spectral density (PSD) by using a Fourier based filtering algorithm. The power spectral density equation (Eq. (60)) used in this work is based on Yastrobov [41]:

$$C(q) = C_0 \left(\frac{q}{q_0}\right)^{-2(1+H)} \tag{56}$$

$$q_0 = \frac{2\pi}{l} \tag{57}$$

where C_0 is a constant, q_0 is the cut-off wave vector, l is the length of the measured surface. After the power spectral density (PSD) is calculated by Eq. (56), the surface can be generated by applying the Hermitian symmetry and the inverse Fourier transform on the obtained PSD (which is shown in Fig.57). The mapping process and the surface deconstruction process are also conducted on this PSD generated surface. Some basic parameters and the fractal dimension value calculated by the roughness-length method [34] for the PSD generated surface are also listed in Table 8. The plot used in calculating the fractal dimension value is shown in Fig.58.

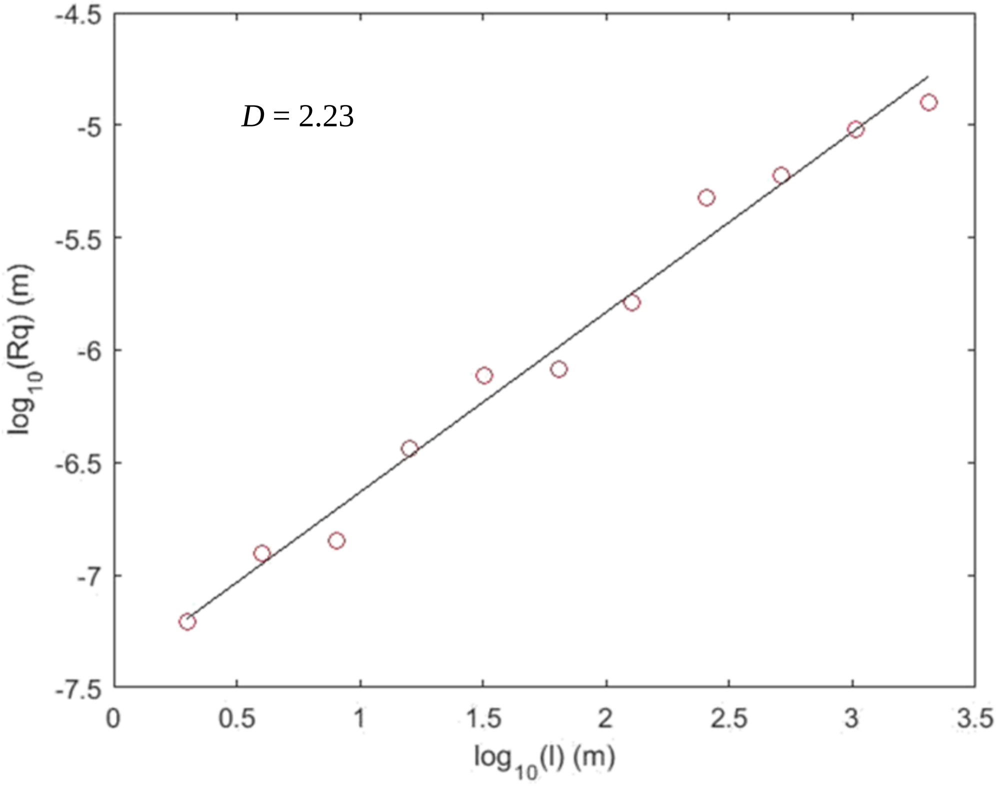

Fig.58 - Plot of the roughness-length method in calculating fractal dimension value for the surface generated by the PSD generated method

Fig.59 to Fig.61 show the film thickness, the mechanical deformation, the contact area distribution of the PSD generated surface for the same specific case as the measured surface shown in Fig.49 (f_c = 33,300 m^{-1}, h_s = 1 μm, ω = 0.14 rad/s). It can be found by comparing

Fig.59 and Fig.60 that the larger mechanical deformation happens at the place where the film thickness is smaller. Fig.61 shows that the boundary has higher contact area ratio which means the real area of contact is larger at the boundary. The larger the contact area ratio is, the higher the mechanical deformation will be.

Figs. 62 - 64 show the solid contact pressure distribution, the fluid pressure distribution and the total pressure distribution of the PSD generated surface (f_c = 33,300 m^{-1}, h_s = 1 μm, ω = 0.14 *rad/s*). Same phenomena happen as for the measured surface that most of the pressure is from solid contact and larger pressure lies at the boundary where the contact area ratio is large. Then the load carrying capacity and the frictional torque values for the PSD generated surface can be evaluated (see Table 8 for the values). Again, most of the load carrying capacity and the frictional torque are generated by the solid contact.

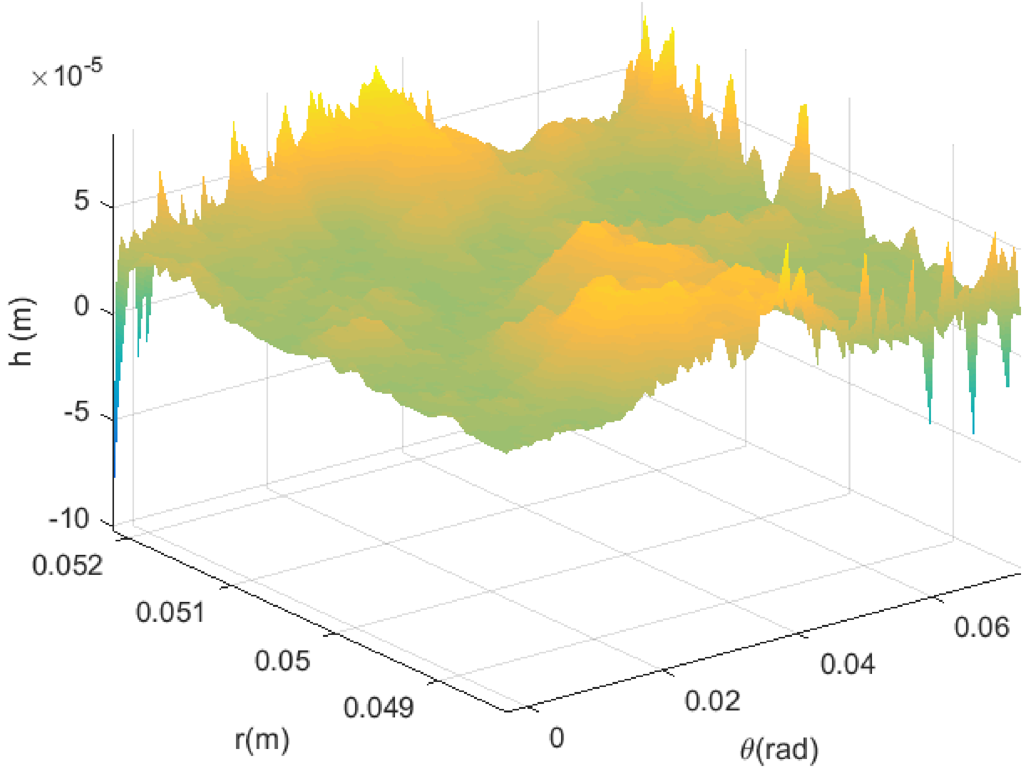

Fig.59 - Film thickness of the PSD generated surface (f_c = 33,300 m^{-1}, h_s = 1 μm, ω = 0.14 *rad/s*)

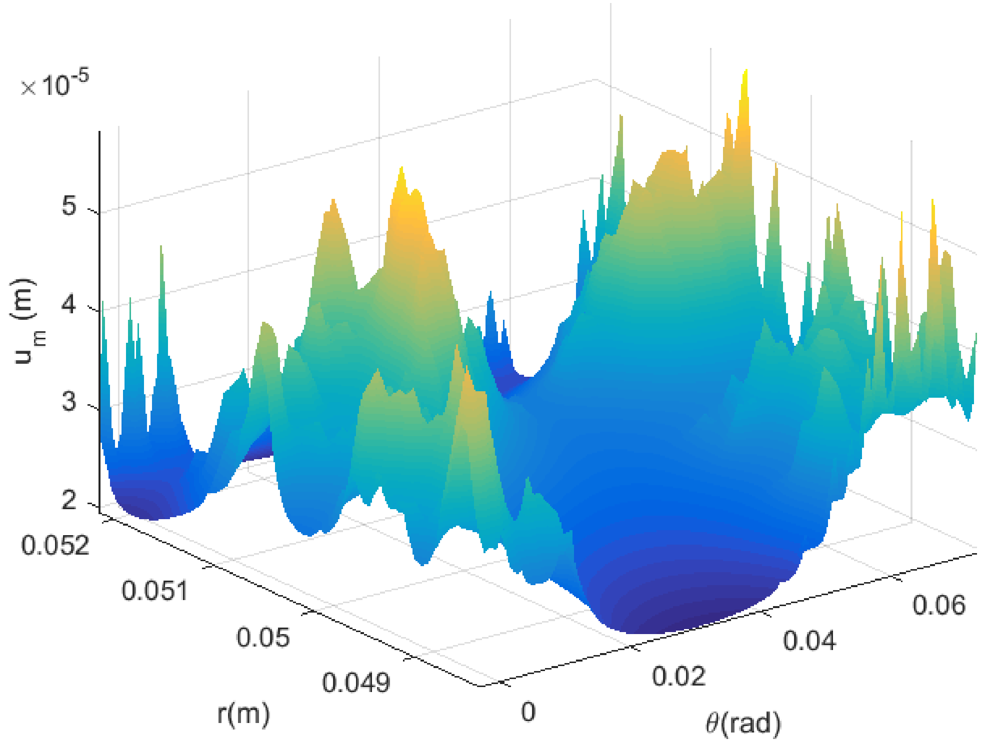

Fig.60 - Mechanical deformation of the PSD generated surface (f_c = 33,300 m^{-1}, h_s = 1 μm, ω = 0.14 rad/s)

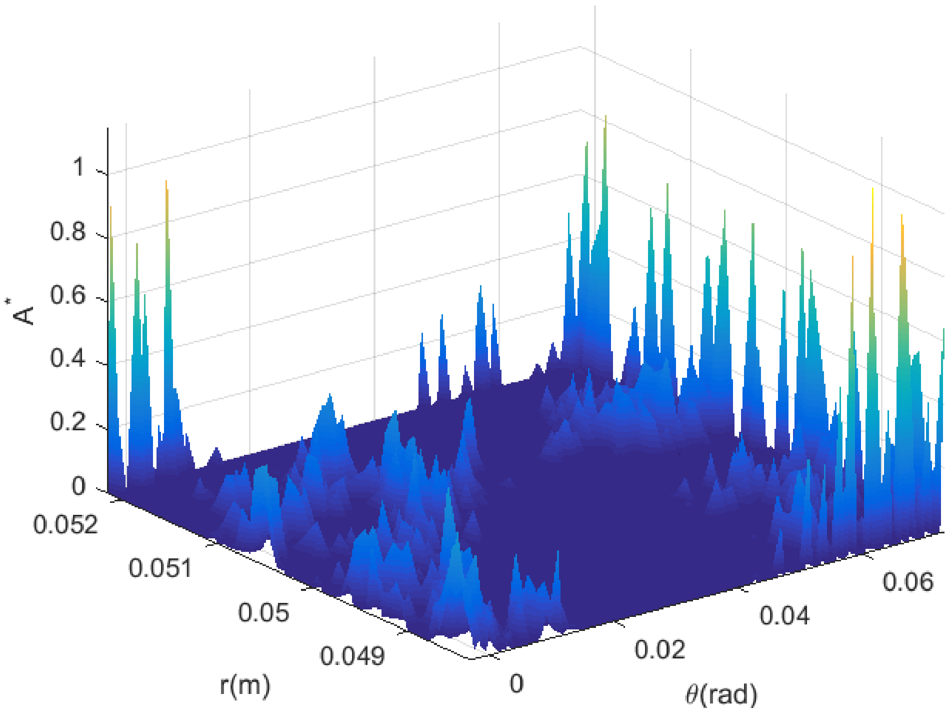

Fig.61 - Contact area ratio at each node of the PSD generated surface (f_c = 33,300 m^{-1}, h_s = 1 μm, ω = 0.14 rad/s)

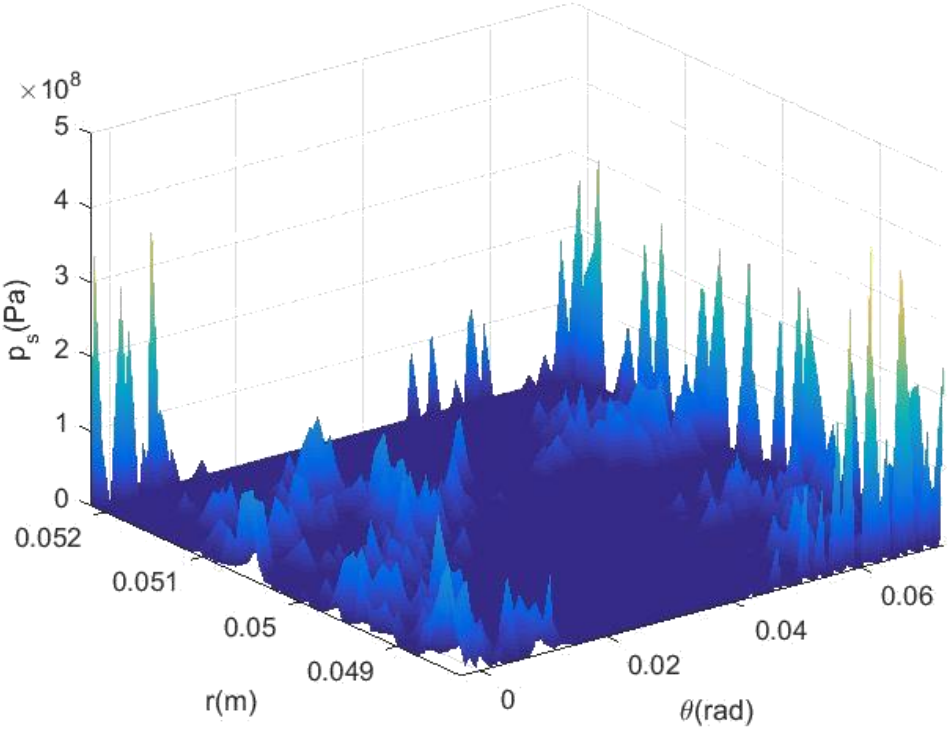

Fig.62 - Solid contact pressure distribution on the PSD generated surface (f_c = 33,300 m^{-1}, h_s = 1 μm, ω = 0.14 *rad/s*)

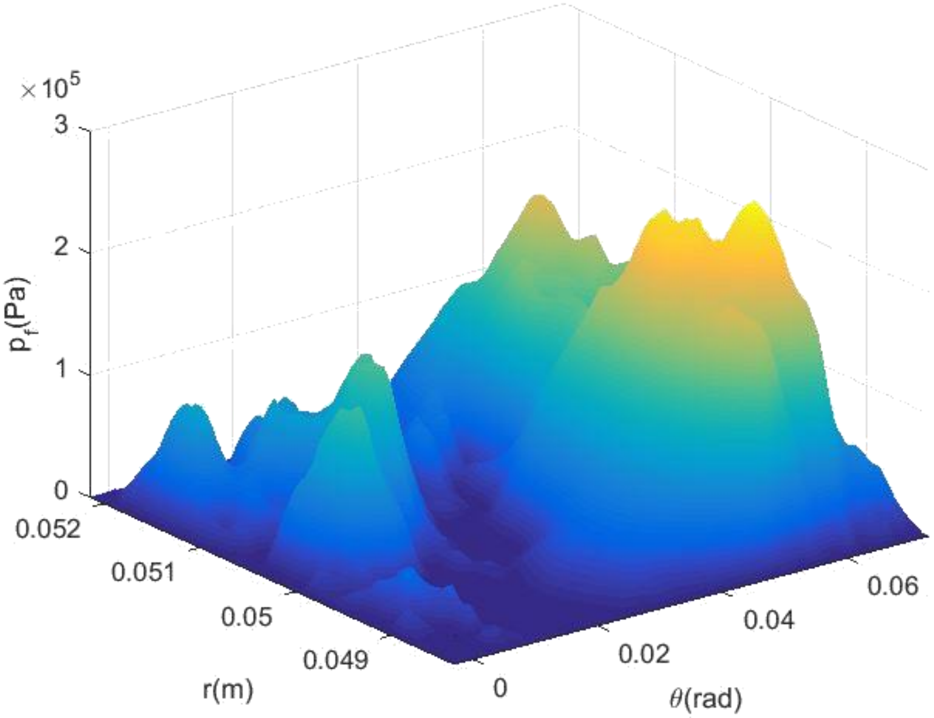

Fig.63 - Solid contact pressure distribution on the PSD generated surface (f_c = 33,300 m^{-1}, h_s = 1 μm, ω = 0.14 *rad/s*)

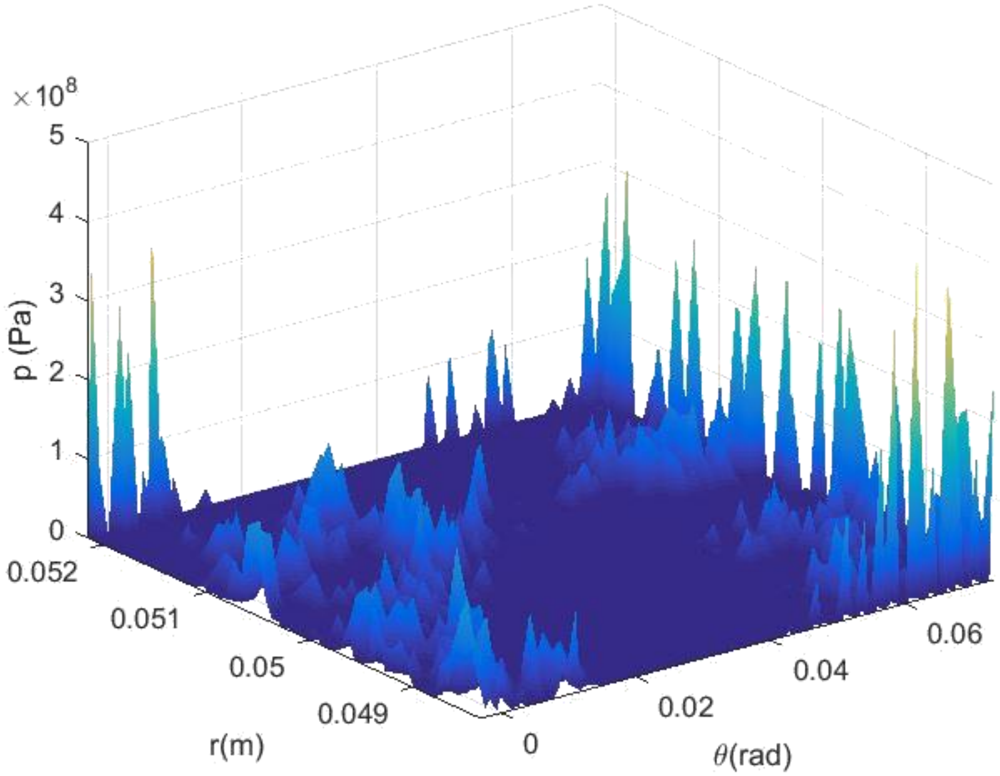

Fig.64 - Total pressure distribution on the PSD generated surface (f_c = 33,300 m^{-1}, h_s = 1 μm, ω = 0.14 *rad/s*)

Table 8 - Values of the load carrying capacity and the frictional torque for the PSD generated surface (f_c = 33,300 m^{-1}, h_s = 1 μm, ω = 0.14 *rad/s*)

	From solid contact	From fluid shearing	Total	Percentage from solid contact
Load carrying capacity, *L*	3.5712×10^3 *N*	31.2027 *N*	3.6027×10^3 *N*	99.13%
Frictional torque, *T*	4.8355 *N·m*	0.0539 *N·m*	4.8893 *N·m*	98.90%

6.2.2 Midpoint displacement method

This surface generation method was first proposed by Fournier et. al. [42] in 1982 and then discussed by Saupe [43] and Voss [44]. The generated process of this method can be summarized below (Fig.65 schematically shows the generated process of this method):

1) Considering a square in the x-z plane, the height of four corners in the plane is from the Gaussian distribution $N(\mu,\sigma^2)$;

2) Picking up the midpoint of the square, the height of the midpoint is the average value of the four corners plus a Gaussian random number $N(0,1)$ and the fractal dimension value calculated from the measured surface is also considered;

3) Calculating the height of the midpoint of every side of the square, then the initial plane can be divided into four new squares;

4) This process is repeated for each new obtained square with the original large squares until we get the desired surface resolution.

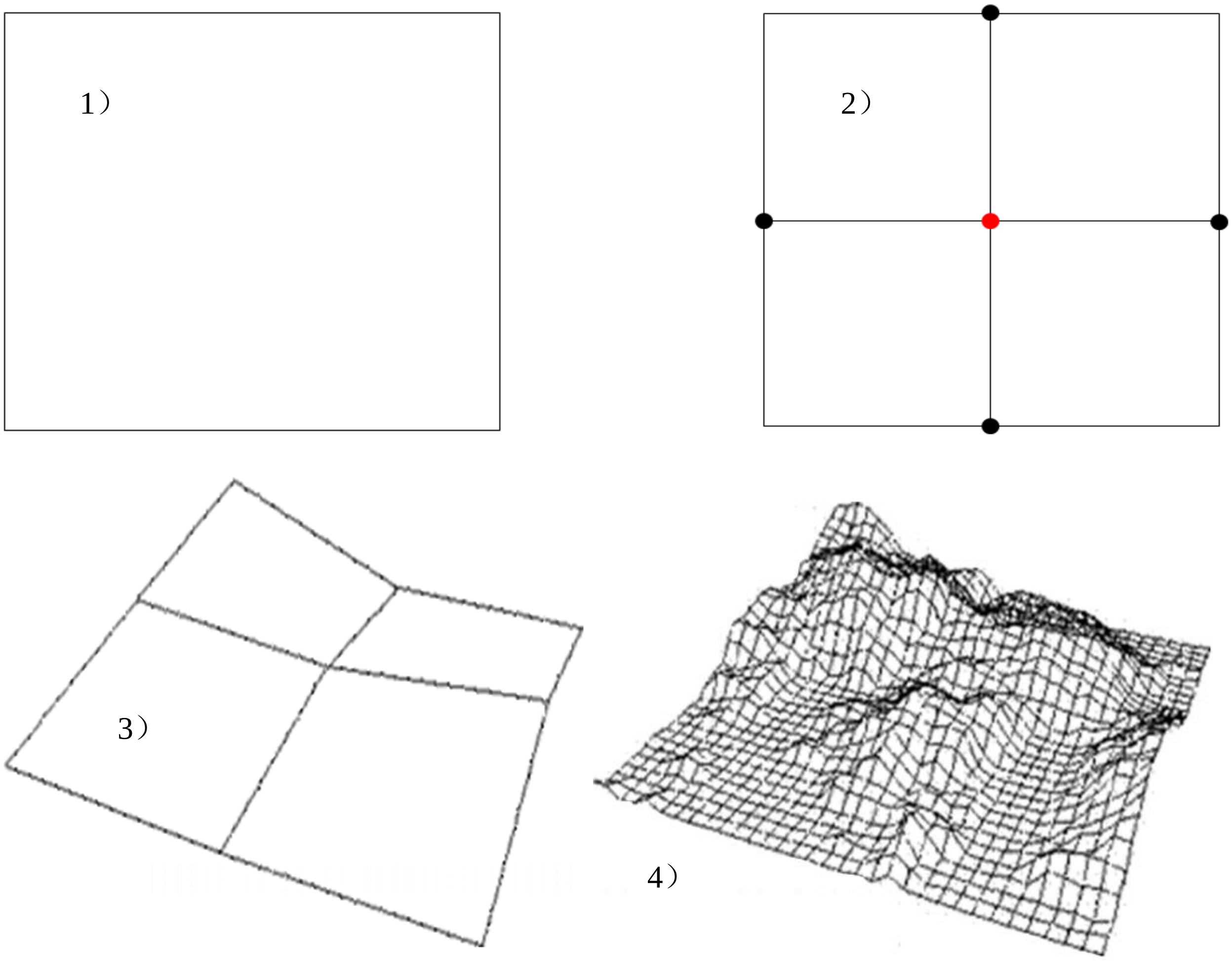

Fig.65 - Generated process of the midpoint displacement method

In this process, the expectation of the distribution, μ, and root mean square roughness, σ, values are all from the measured surface shown in Fig.49. Since the fractal dimension value D = 3-H, the fractal dimension value in step 2) is considered by using the equation below [45]:

$$\sigma_i^2 = \frac{1}{2^{2H(i+1)}}\sigma^2 \tag{58}$$

where σ_i is a modified RMS roughness in the *i-th* iteration step.

Fig.66 shows the surface generated from the midpoint displacement method (MDM). The same parameters are calculated for the MDM generated surface and listed in Table 9. The plot used for calculating fractal dimension value is shown in Fig.67. Again, the same mapping process and the surface deconstruction process are conducted on this MDM generated surface.

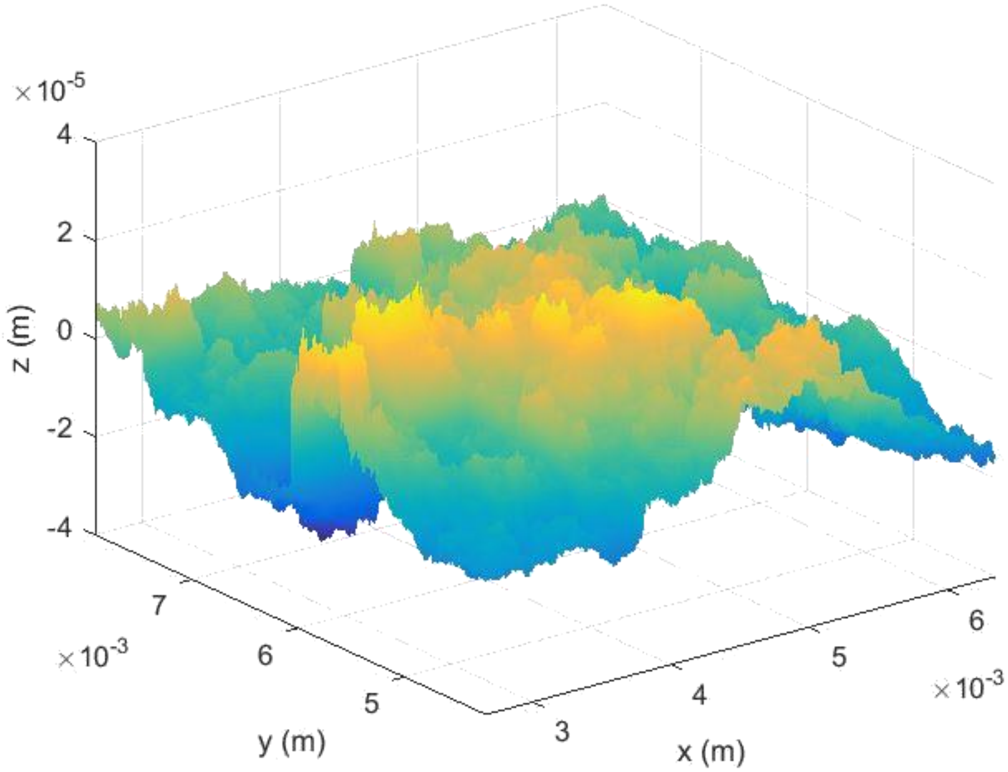

Fig.66 - Surface generated by midpoint displacement method

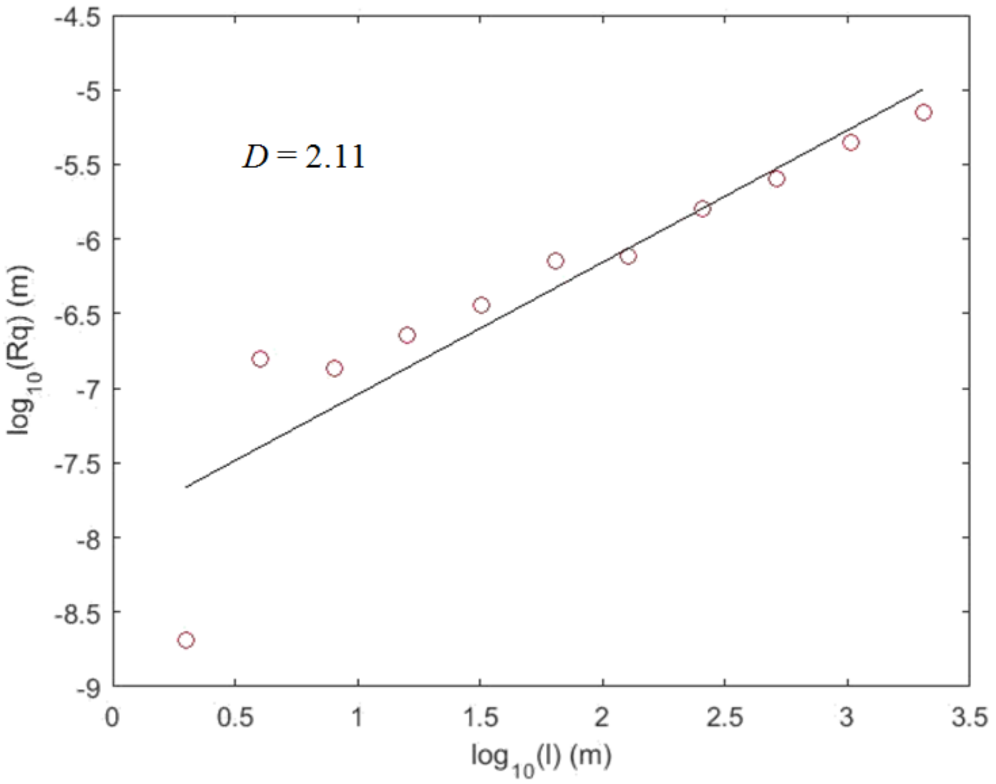

Fig.67 - Plot of the roughness-length method in calculating fractal dimension value for the MDM generated method

Table 9- Basic parameters calculated for the measured surface, the PSD generated surface and the MDM generated surface

Parameters	Measured surface	PSD generated surface	MDM generated surface
Root mean square (R_q)	1.1074×10^{-5} m	$1.2619\text{e}\times10^{-5}$ m	7.0002×10^{-6} m
Kurtosis (K)	2.8980	7.2189	4.7459
Skewness (Sk)	0.0908	-1.0941	0.0768
Asperity radius (R_A)	1.1096×10^{-5} m	1.2370×10^{-5} m	4.6311×10^{-6} m
Asperity density (η_s)	3.5170×10^{10} m^{-2}	$2.6728\text{e}\times10^{10}$ m^{-2}	7.9589×10^{10} m^{-2}
Fractal dimension (D)	2.23	2.23	2.11

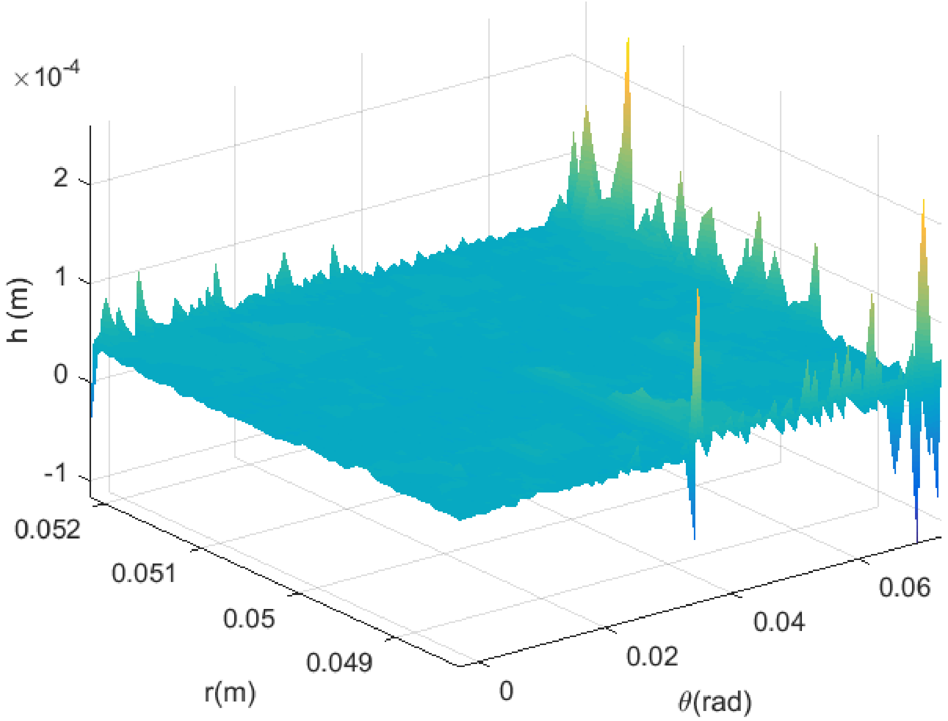

Fig.68 - Film thickness of the MDM generated surface (f_c = 33,300 m^{-1}, h_s = 1 μm, ω = 0.14 *rad/s*)

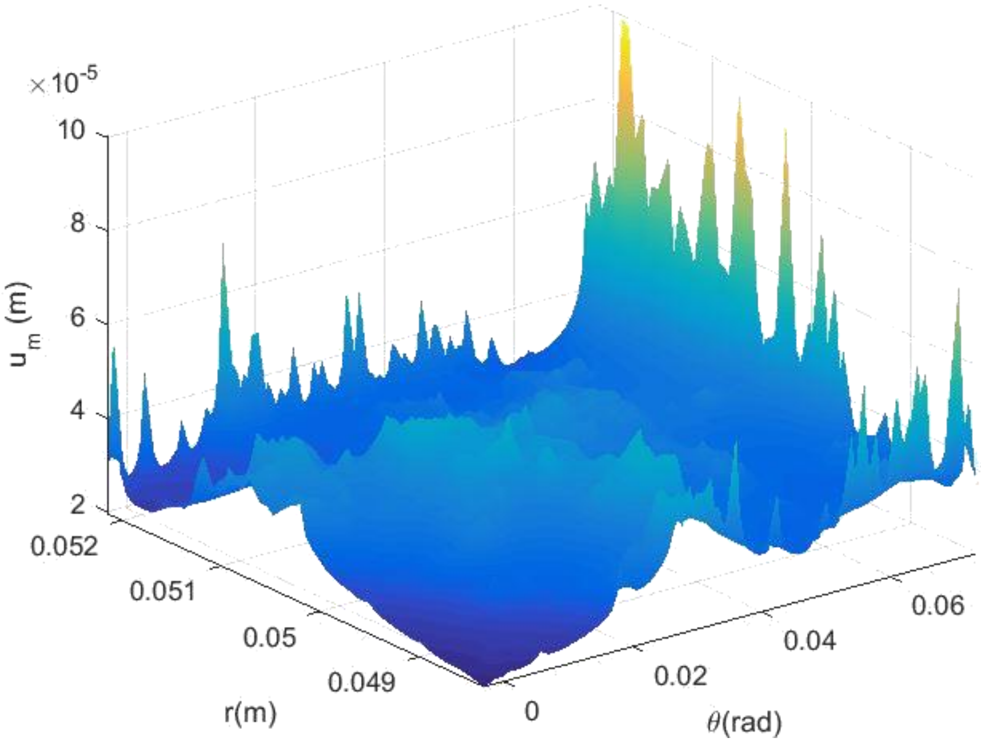

Fig.69 - Mechanical deformation of the MDM generated surface (f_c = 33,300 m^{-1}, h_s = 1 μm, ω = 0.14 *rad/s*)

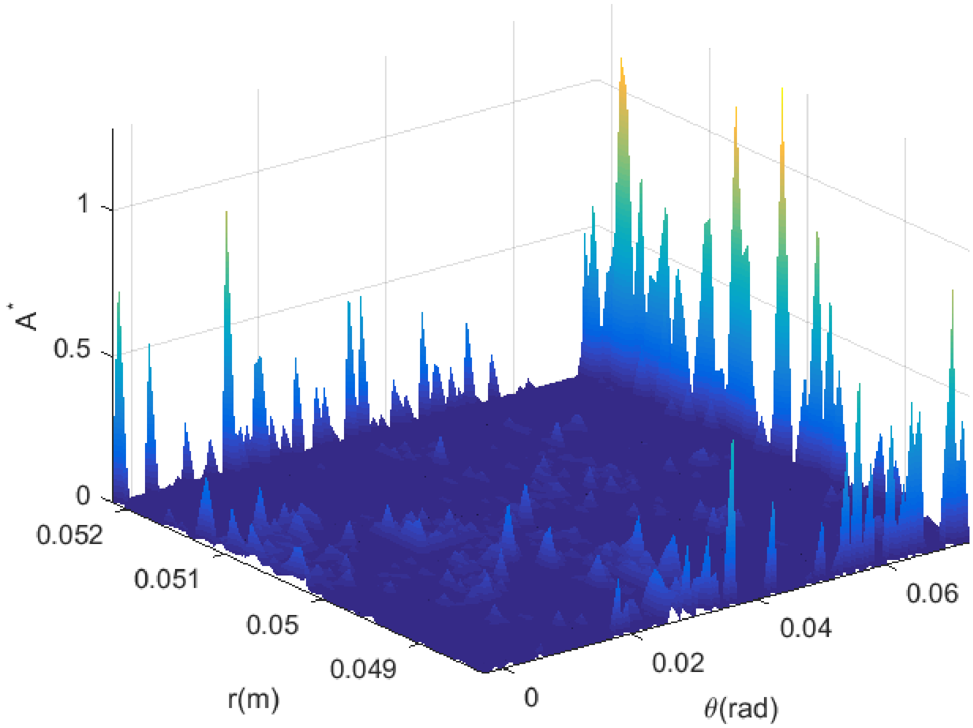

Fig.70 - Contact area distribution of the MDM generated surface (f_c = 33,300 m^{-1}, h_s = 1 μm, ω = 0.14 rad/s)

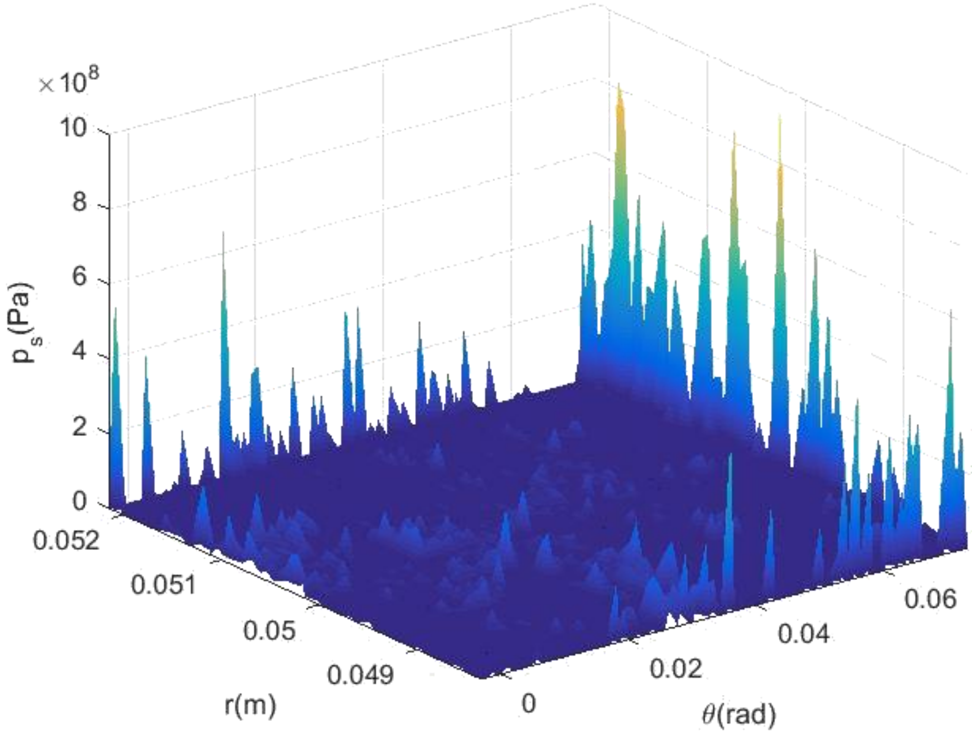

Fig.71 - Solid contact pressure distribution of the MDM generated surface (f_c = 33,300 m^{-1}, h_s = 1 μm, ω = 0.14 rad/s)

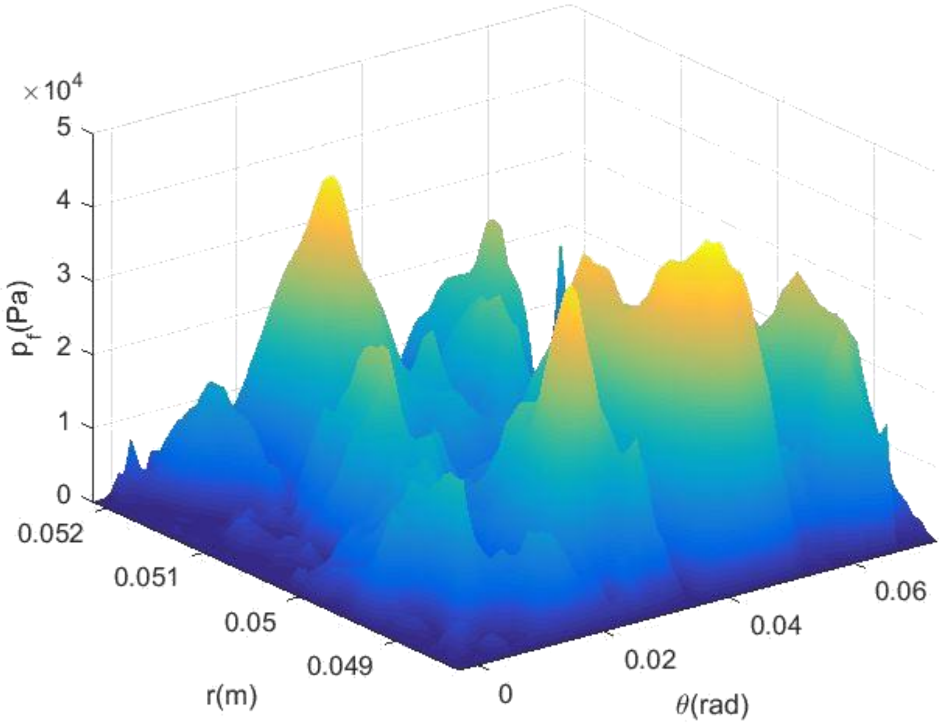

Fig.72 - Fluid pressure distribution of the MDM generated surface (f_c = 33,300 m^{-1}, h_s = 1 μm, ω = 0.14 *rad/s*)

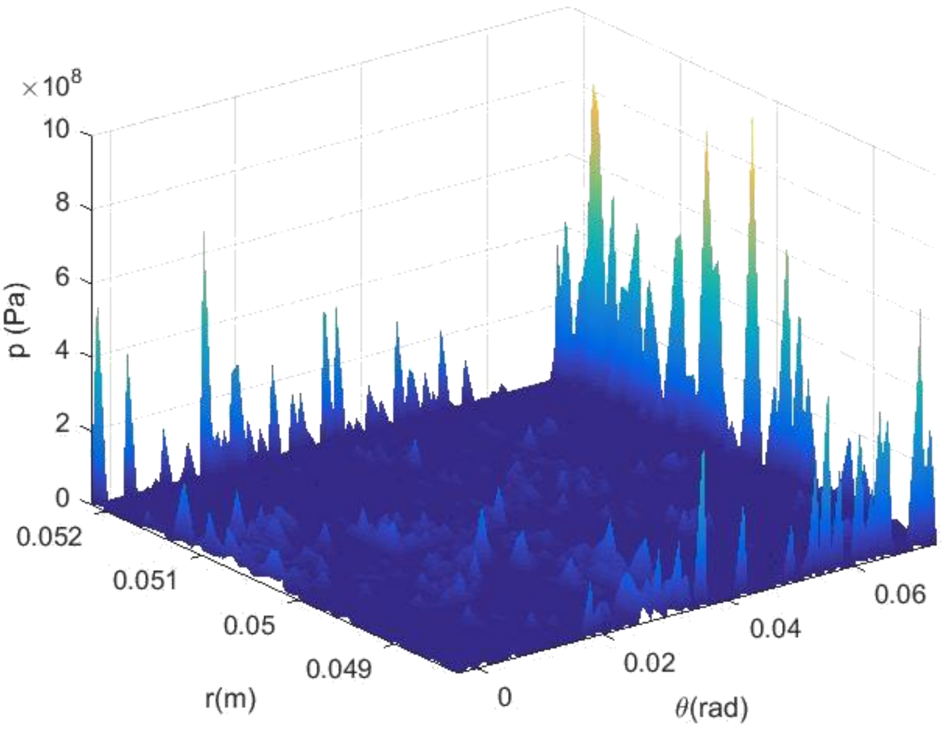

Fig.73 - Total pressure distribution of the MDM generated surface (f_c = 33,300 m^{-1}, h_s = 1 μm, ω = 0.14 *rad/s*)

Table 10 - Values of the load carrying capacity and the frictional torque for the PSD generated surface (f_c = 33,300 m^{-1}, h_s = 1 μm, ω = 0.14 *rad/s*)

	From solid contact	From fluid shearing	Total	Percentage from solid contact
Load carrying capacity, *L*	3.8371×10^3 *N*	5.4129 *N*	3.8474×10^3 *N*	99.73%
Frictional torque, *T*	5.2097 *N·m*	0.0498 *N·m*	5.2594 *N·m*	99.06%

The film thickness distribution, the mechanical deformation, the contact area distribution, the solid contact pressure distribution, the fluid pressure distribution and the total pressure distribution of the MDM generated surface based on the same specific case as the measured surface are calculated and plotted in Figs. 68 - 73 (f_c = 33,300 m^{-1}, h_s = 1 μm, ω = 0.14 *rad/s*).

Different from the measured surface and the PSD generated surface, some points at the boundary of the MDM generated surface have higher film thickness according to Fig.68. However, the larger mechanical deformation and the higher contact area ratio still happen at the place where the film thickness is thinner by comparing Fig.68, Fig.69 and Fig.70. Most of the pressure is from the solid contact as for the measured surface and the PSD generated surface based on the Figs. 71, 72 and 73.

The load carrying capacity and the frictional torque values then can be computed for the MDM generated surface, which are listed in Table 10 (most of the load carrying capacity and the frictional torque are generated by the solid contact).

Chapter 7

ANALYSIS OF MEASURED AND GENERATED SURFACES

7.1 Influence of the Angular Velocity

It can be found from the pressure distribution results in Chapter 5 and Chapter 6 that the pressure contribution from the fluid is very small compared to the values from solid contact, so that the contribution of load carrying capacity from the fluid is also very small for this application case. As we mentioned previously, these cases are for a relatively low angular velocity of 0.14 *rad/s* based on an application of this bearing. Therefore, the influence of angular velocity at values larger than this on the load carrying capacity and the frictional torque are also investigated. With the constant cut-off frequency (f_c = 33,300 m^{-1}) and the same initial surface separation (h_s = 30 μm), the angular velocity is changed from 0.14 *rad/s* to 419 *rad/s*. Figs. 74 and 77 show the relationships between the total load carrying capacity (L_{total}) and the total frictional torque (T_{total}) as a function of the angular velocity (ω) for these three surfaces.

The changing trends of the ratio for the contribution of the fluid part and the solid contact part on the load carrying capacity and the frictional torque with the changing of the angular velocity (ω) for these three surfaces are shown in Figs. 76 and 79. Figs. 75 and 78 show the changing trends of the load carrying capacity from the solid contact (L_s) and the frictional torque from the solid contact (T_s) along with the angular velocity (ω).

In addition, the relationship between the contact area ratio (A^*) and the angular velocity (ω) for these three surfaces and the relationship between the minimum film thickness (h_{min}) and the angular velocity (ω) are also plotted in Fig.80 and Fig.81, separately.

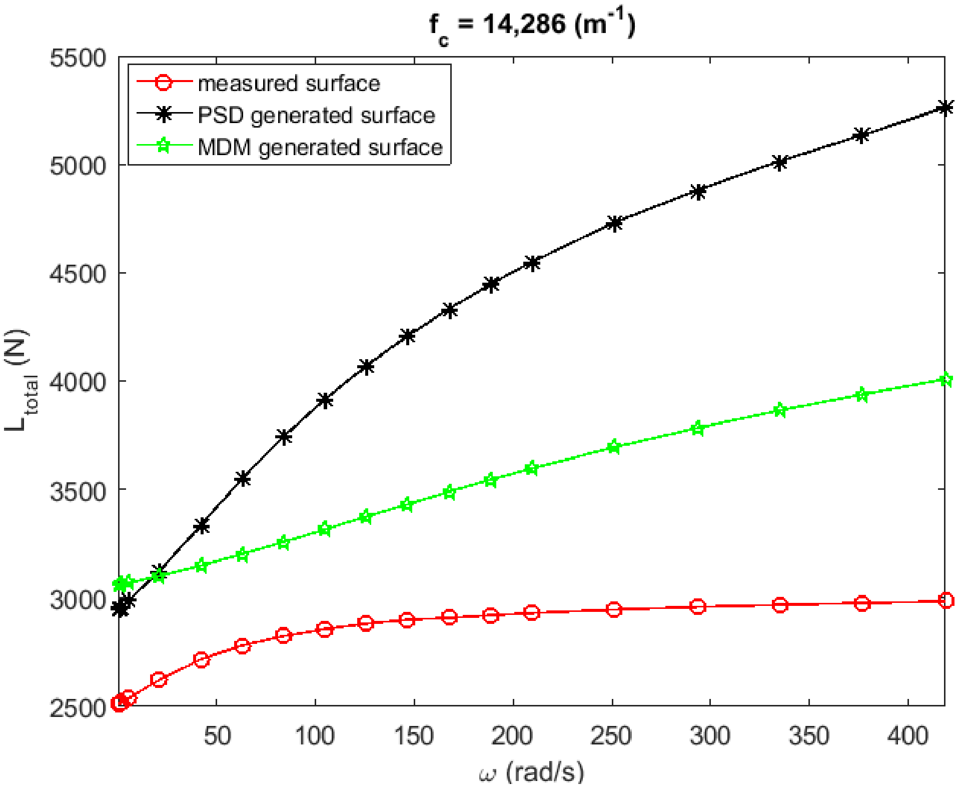

Fig.74 - Relationship between the total load carrying capacity (L_{total}) and the angular velocity (ω)

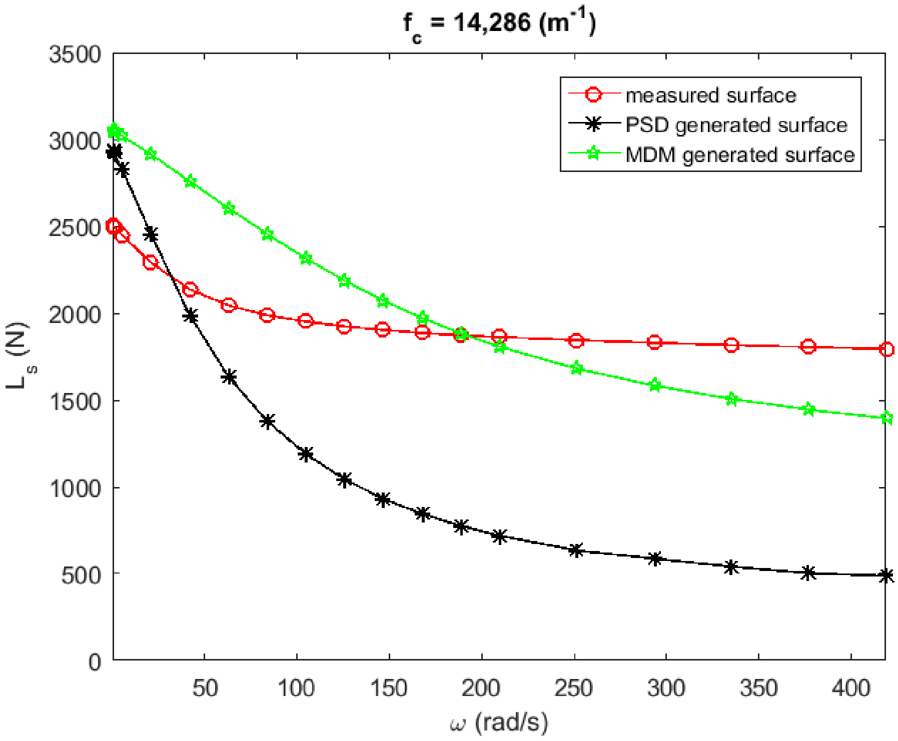

Fig.75 - Relationship between the load carrying capacity from the solid contact (L_s) and the angular velocity (ω)

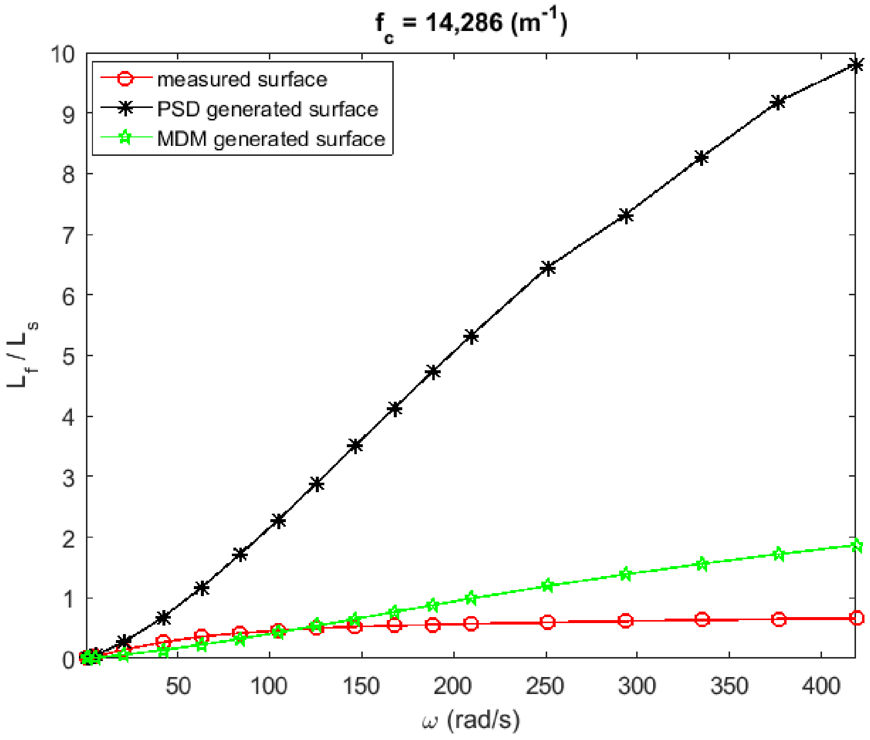

Fig.76 - Relationship between the ratio of the load carrying capacity from the fluid (L_f) and the load carrying capacity from the solid contact (L_s) and the angular velocity (ω)

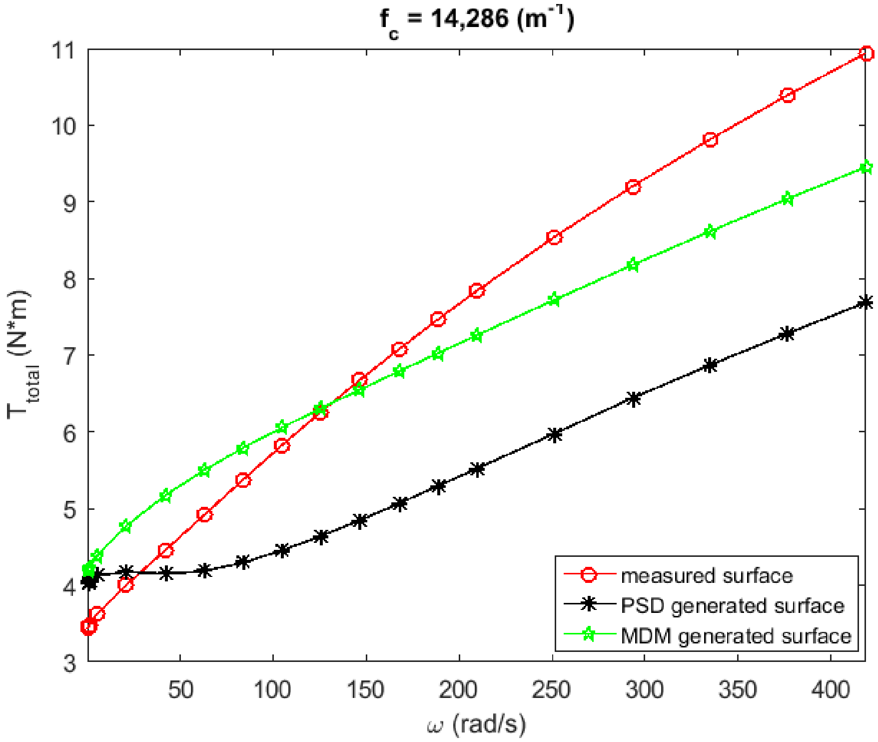

Fig.77 - Relationship between the total frictional torque (T_{total}) and the angular velocity (ω)

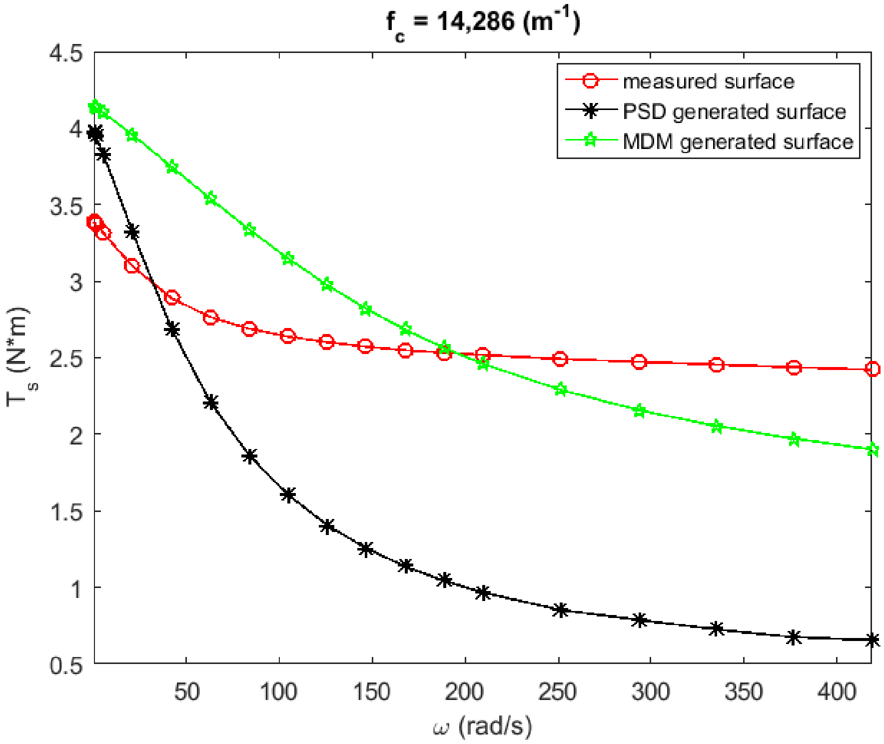

Fig.78 - Relationship between the frictional torque from the solid contact (T_s) and the angular velocity (ω)

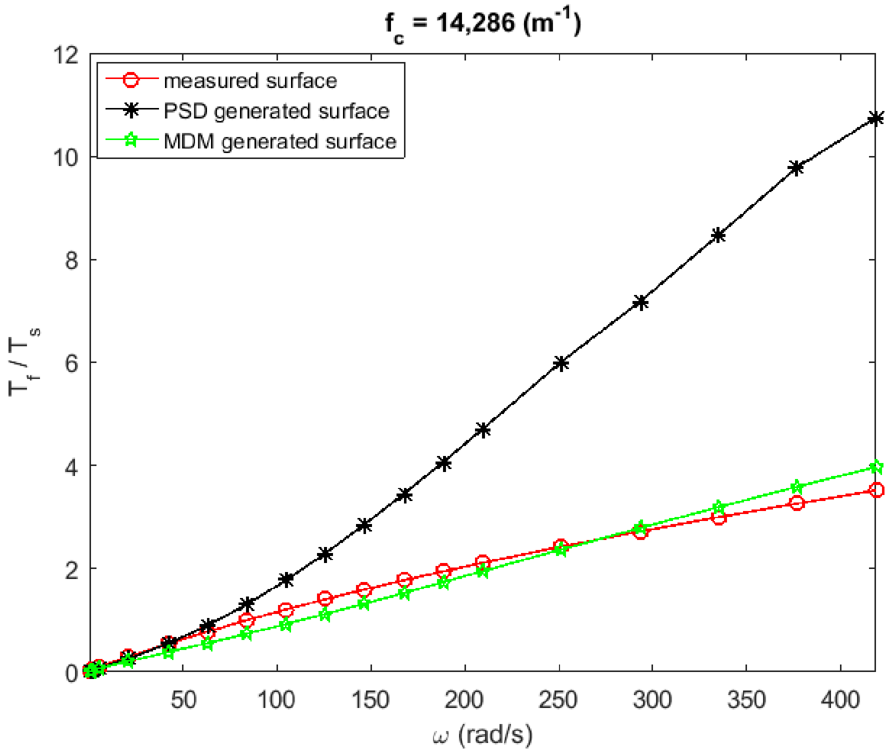

Fig.79 - Relationship between the ratio of the frictional torque from the fluid (T_f) and the frictional torque from the solid contact (T_s) and the angular velocity (ω)

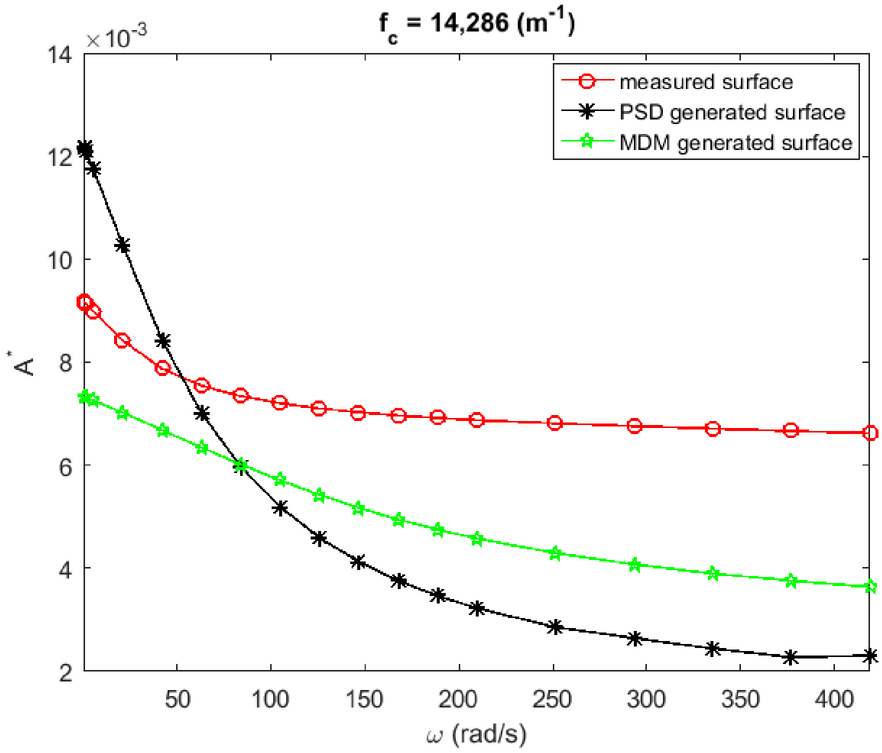

Fig.80 - Relationship between the contact area ratio (A^*) and the angular velocity (ω)

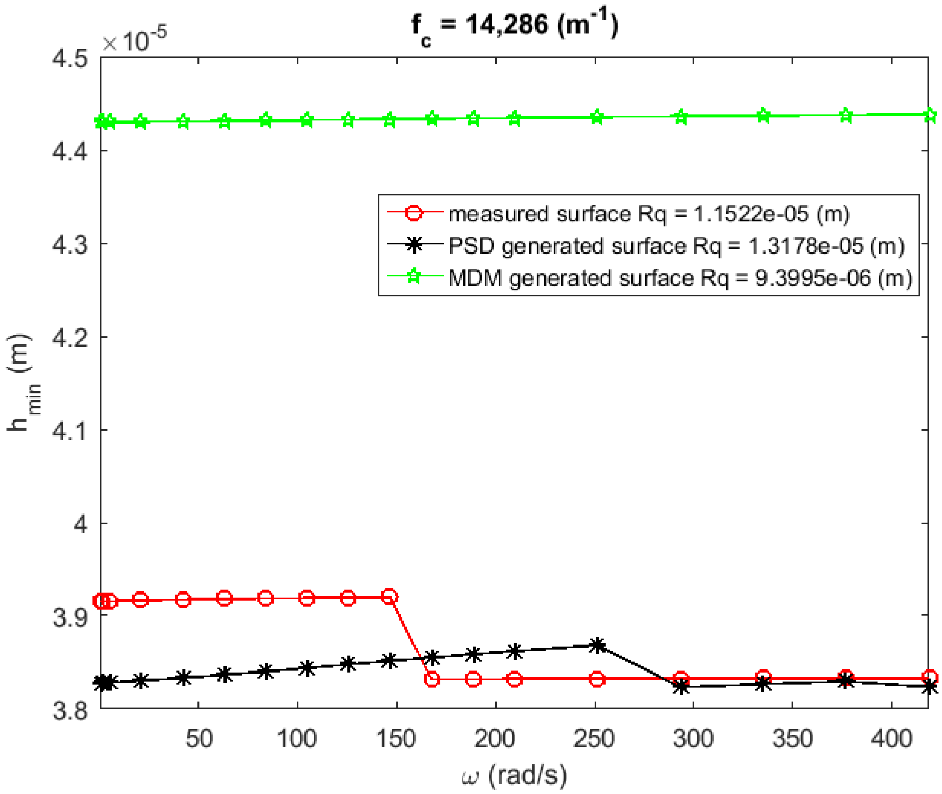

Fig.81 - Relationship between the minimum film thickness (h_{min}) and the angular velocity (ω)

Fig.74 indicates that with the increase of the angular velocity, the load carrying capacity increases, which is in agreement with typical hydrodynamic bearing behavior. Again note that the original surface separation is held constant, but the actual surface separation can increase due to deformation. The slope of the load carrying capacity with speed is the steepest for the PSD generated surface. The slope of the load for the measured surface is the least. Meanwhile, for the same angular velocity, the load carrying capacity value from the PSD generated surface is larger than the other two surfaces when the angular velocity is larger than 20 *rad/s*.

Fig.75 shows that the load carrying capacity value from the solid contact (L_s) decrease when the angular velocity becomes larger for these three surfaces. The slope of the decrease speed for the PSD generated surface is the steeper than that for the other two surfaces and the decrease speed for the generated surface is the least.

The proportion of the load carrying capacity also increases with the growth of the angular velocity, which means the proportion of the load carrying capacity from fluid has become significant. The ratio for the MDM generated surface is the smallest at the low angular velocity, but the ratio (L_f/L_s) from the measured surface becomes the smallest as angular velocity becomes much larger (Fig.76). It should also be noted from Fig.76 that the ratio (L_f/L_s) for the measured surface is not larger than one, but the ratio (L_f/L_s) for the other two generated surfaces all become larger than one with the increase of the angular velocity. It means much of the load is carried more by the fluid if the ratio (L_f/L_s) is larger than one. This is more desirable for a typical fluid-film bearing. This may be due to clear differences in the larger scale geometries of the generated surfaces compared to the measured surface.

The same phenomena have also been predicted for the frictional torque according to Figs. 77, 78 and 79. The frictional torque values from these three surfaces increase with the increase of the angular velocity, the measured surface increases the most, while the PSD generated surface increase the least. The frictional torque value from the solid contact (L_s) decreases for these three surfaces (T_s). Meanwhile, the contribution of the frictional torque from fluid has increased with the growth of the angular velocity for these three surfaces.

The ratios (L_f/L_s and T_f/T_s) from the PSD generated surface is the largest for all cases. The proportion of the load carrying capacity and the frictional torque from the fluid increases significantly with the growth of the angular velocity and becomes much larger than the load carrying capacity and the frictional torque from solid contact for the PSD generated surface. The increase of the ratios (L_f/L_s and T_f/T_s) with the angular velocity for the measured surface and the

MDM generated surface is much less. The ratios (L_f/L_s and T_f/T_s) from the measured surface becomes the smallest gradually, which means that the contact area in the measured surface is larger than the contact area in the other two generated surfaces at the same angular velocity.

According to Fig.80, the contact area ratio for these three surfaces decreases with the increase of the angular velocity. The PSD generated surface has the highest contact area ratio at the initial angular velocity, and then it decreases more steeply. When the angular velocity is larger than 70 *rad/s*, the contact area ratio for the measured surface becomes the largest. Since the contact area ratio is a measure of the degree of asperity contact during the rotation, the larger the contact area ratio is, the larger the real area of contact is. Fig.80 can also illustrate that the proportion of the load carrying capacity and the frictional torque from the fluid increases with the increase of the angular velocity.

The minimum film thickness with the deformation (h_{min}) for the MDM generated surface is larger than the other two surfaces based on the plot in Fig. 81, but it does not change too much when the angular velocity (ω) becomes larger. The minimum film thickness with the deformation (h_{min}) value for the measured surface decreases when the angular velocity (ω) is larger than 150 *rad/s* and then start to increase. For the PSD generated surface, the minimum film thickness with the deformation (h_{min}) increases first with the increase of the angular velocity (ω) and then decrease when the angular velocity is larger than 250 *rad/s*.

It can be concluded from the analysis above that the angular velocity influences each of the surfaces differently when comparing the two generated surfaces from the measured surface. Therefore, the two surface generation methods are not suitable in representing the measured surface.

7.2 Influence of the Cut-off Frequency

In the case we discussed above, the cut-off frequency we used to deconstruct the surface is f_c = 33,300 m^{-1} (the wavelength, λ, is 30 μm). More cases with different cut-off frequencies are run for these three different surfaces (the angular velocity is held constant during this process at ω = 250 *rad/s* and the initial surface separation h_s = 1 μm), and the plots of the relationship between the cut-off frequency and the total load carrying capacity and the total frictional torque for these three surfaces are shown in Figs. 82 and 83. The plots of the relationship between the cut-off frequency (f_c) and the total load carrying capacity (L_{total}) and the total frictional torque (T_{total}) for more cases with different angular velocity (the initial surface separation is held constant at h_s = 1 μm) are shown in Appendix A and Appendix B, separately.

It can be seen from Figs. 82 and 83 that the load carrying capacity value and the frictional torque value from the two generated surfaces are very large when the cut-off frequency is very small. Whereas, the load carrying capacity value and the frictional torque value from two generated surfaces decrease with the increase of the cut-off frequency. Meanwhile, the predictions of these two values from two generated surfaces become coincident with the values for the measured surface if the cut-off frequency becomes large enough. The load carrying capacity and the frictional torque values from the MDM generated surface are much closer to the values from the measured surfaces than the PSD generated surface. It should also be noted that the change of the load carrying capacity value and the frictional torque value from the measured surface is very small with the increase of the cut-off frequency.

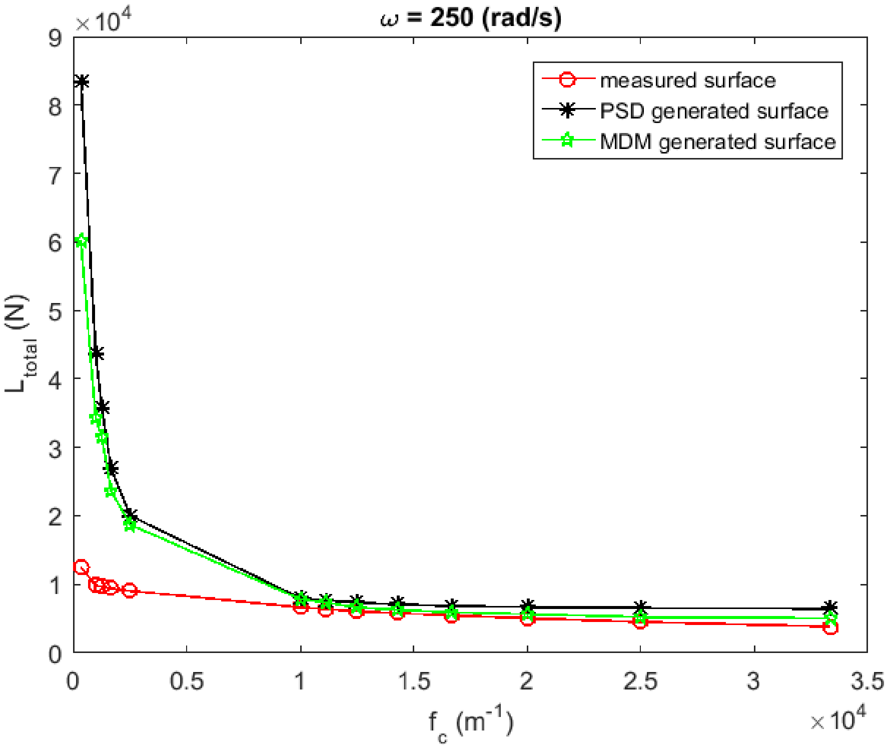

Fig.82 - Relationship between the total load carrying capacity (L_{total}) and the cut-off frequency (f_c)

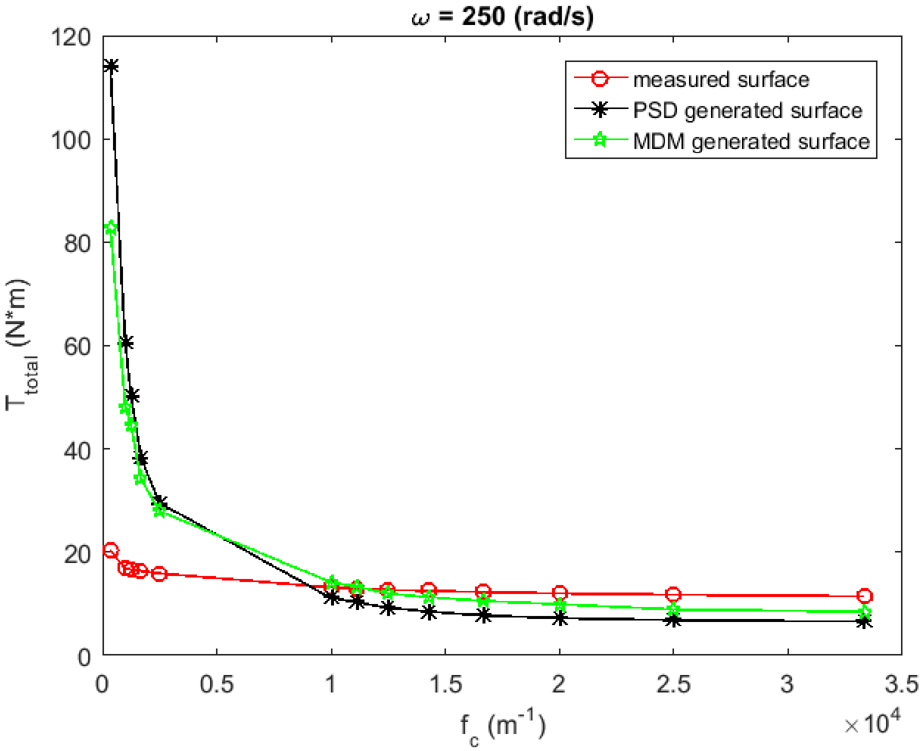

Fig.83 - Relationship between the total frictional torque (T_{total}) and the cut-off frequency (f_c)

From the analysis above, when the cut-off frequency used to deconstruct the surface is small, both of the PSD generated surface and the MDM generated surface are not very suitable in representing the measured surface. However, these two generated surfaces can represent the measured surface when the cut-off frequency becomes large. It means that the characterization ability of the generated surfaces depends heavily on the cut-off frequency.

By comparing the parameter values in Table 8, the *Rq* values of the measured surface, the PSD generated surface and the MDM generated surface have little difference. The *Sk* and *K* values for the MDM generated surface are much closer to the measured surface than the PSD generated surface, but the values of asperity radius and asperity density calculated from the MDM generated surface are not as consistent as the values calculated by the PSD generated surface when comparing with the values of the measured surface. Clearly, these two regenerated fractal surfaces are structured fundamentally different than the measured surface. This will result in different behavior in the mix-lubrication regime.

It should be noted that both of the two generated surface methods consider the fractal dimension value when generating the surface, and the generated surfaces based on these two methods are not consistent in characterizing the measured surface. Therefore, it should be considered carefully if the generated surface based on the fractal dimension can be used to represent a measured surface. Due to the differences of the predicted results, the fractal dimension is not a reliable value to solely characterize the measured surface. However, if other parameters could be considered in the generation process as well, improvement might be made.

However, since only a few generated surfaces are evaluated due to the computational limitations, the results cannot be considered generalized.

7.3 Influence of the Initial Surface Separation

In this section, the influence of the different initial surface separations (h_s) on the indicators of these three surfaces is investigated with the constant cut-off frequency value (f_c = 33,300 m^{-1}) and the different angular velocity values. Figs. 84 to 98 show the plot of the relationships between the angular velocity and the contact area ratio, the load carrying capacity, the frictional torque, L_f/L_s and T_f/T_s with different initial surface separations for the measured surface, the PSD generated surface and the MDM generated surface.

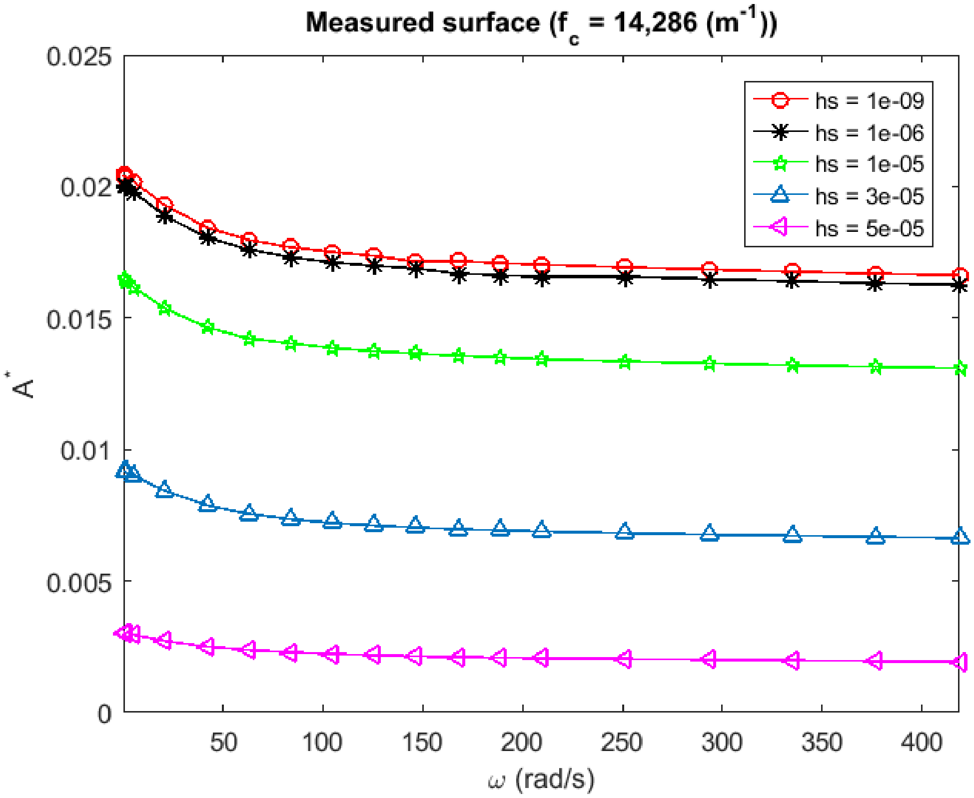

Fig.84 - Relationship between the contact area ratio (A^*) and the angular velocity (ω) at different initial surface separations for the measured surface

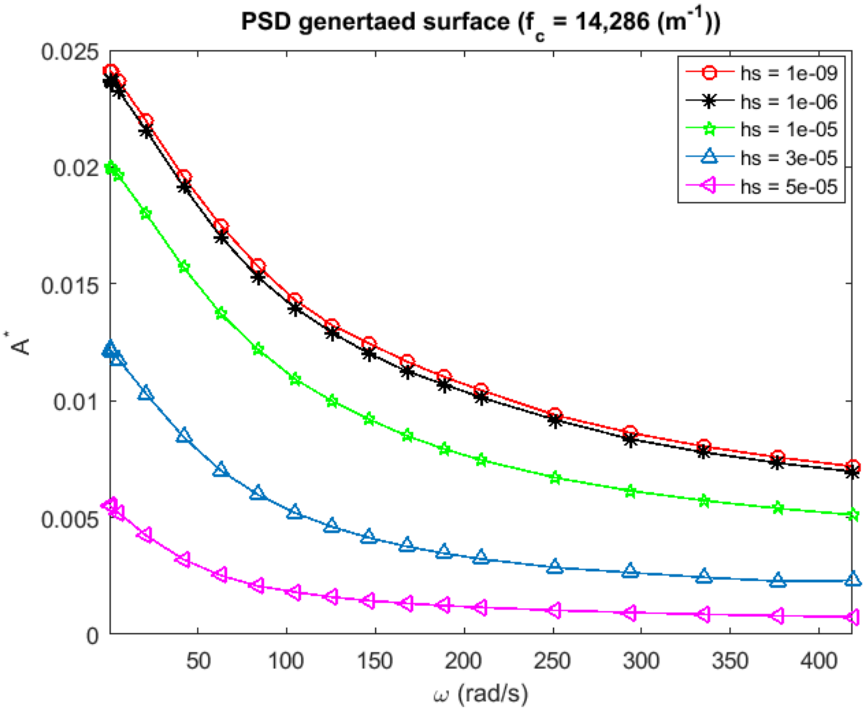

Fig.85 - Relationship between the contact area ratio (A^*) and the angular velocity (ω) at different initial surface separations for the PSD generated surface

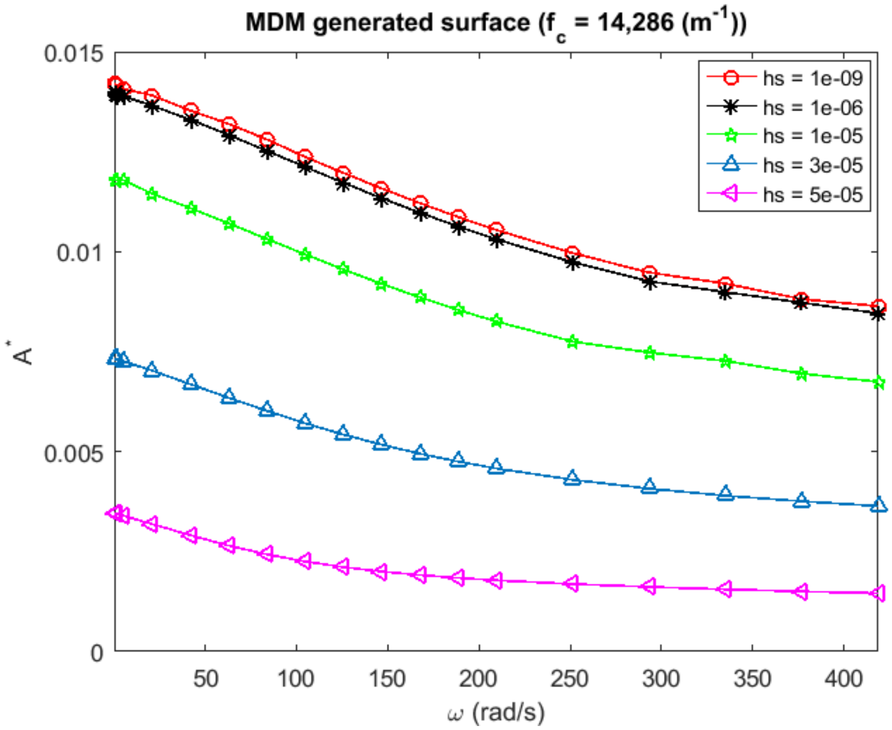

Fig.86 - Relationship between the contact area ratio (A^*) and the angular velocity (ω) at different initial surface separations for the MDM generated surface

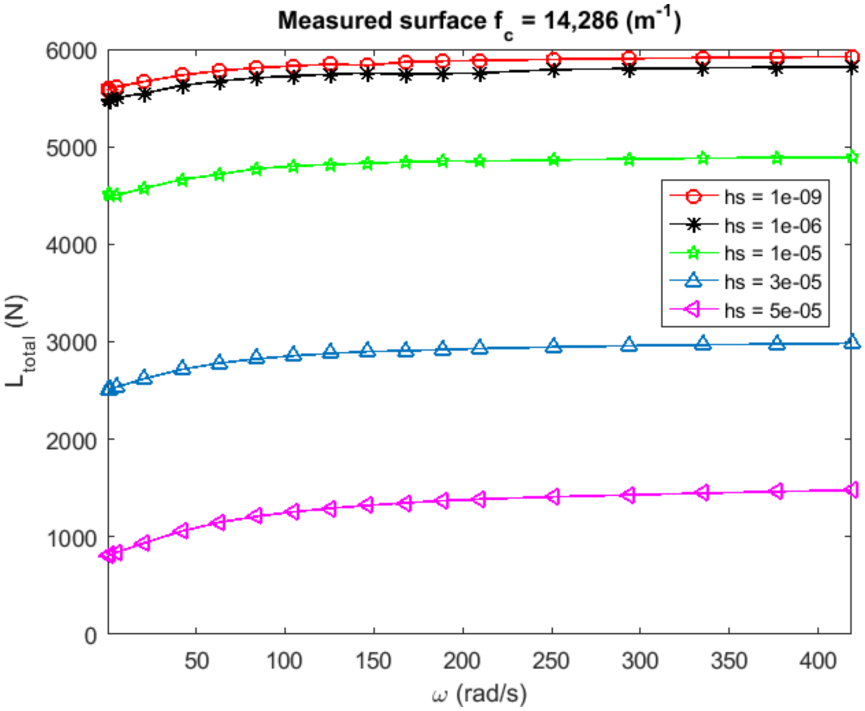

Fig.87 - Relationship between the load carrying capacity (L_{total}) and the angular velocity (ω) at different initial surface separations for the measured surface

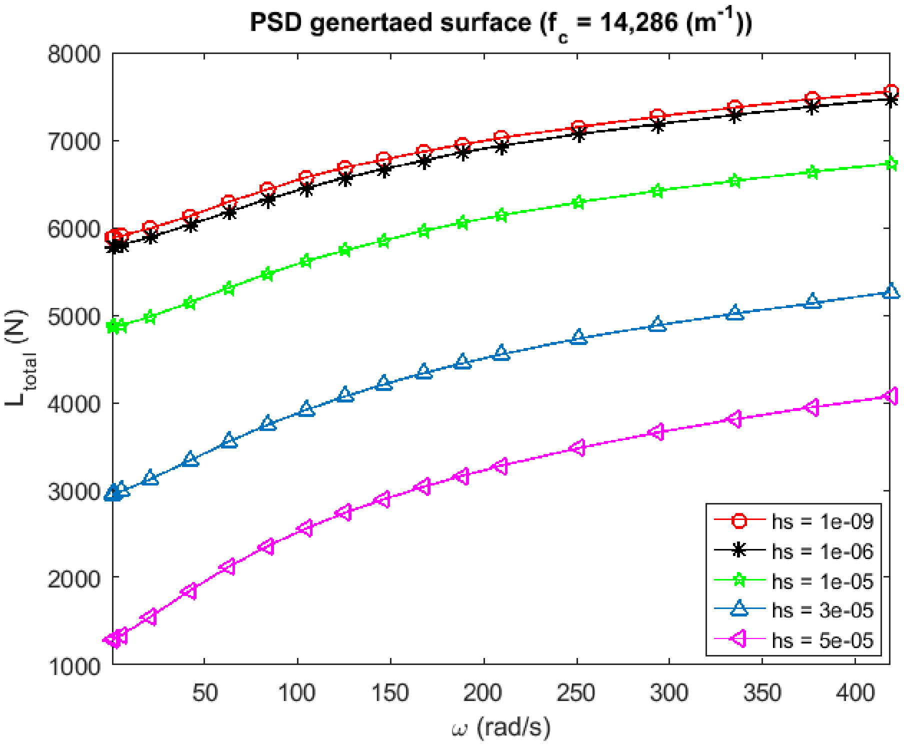

Fig.88 - Relationship between the load carrying capacity (L_{total}) and the angular velocity (ω) at different initial surface separations for the PSD generated surface

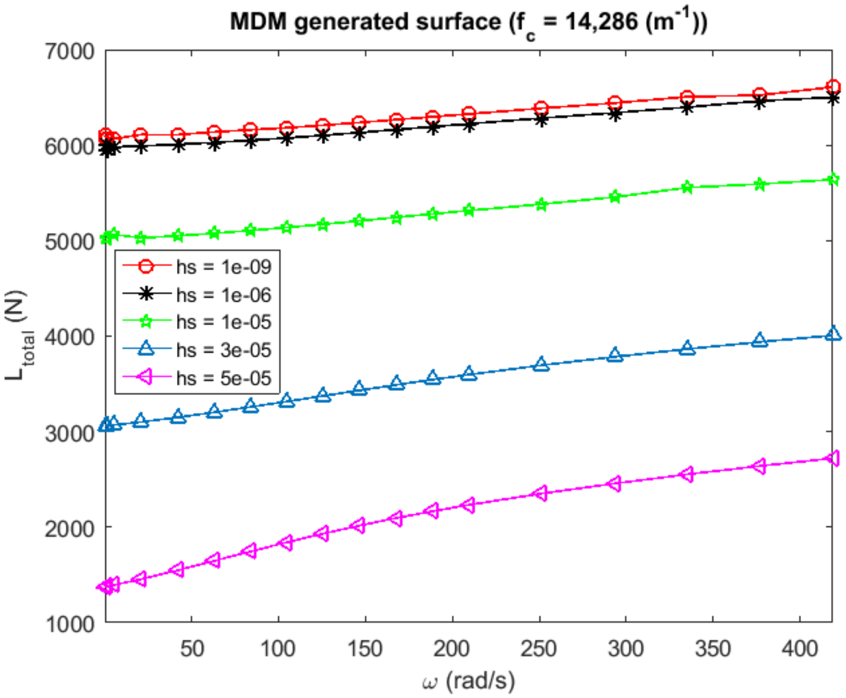

Fig.89 - Relationship between the load carrying capacity (L_{total}) and the angular velocity (ω) at different initial surface separations for the MDM generated surface

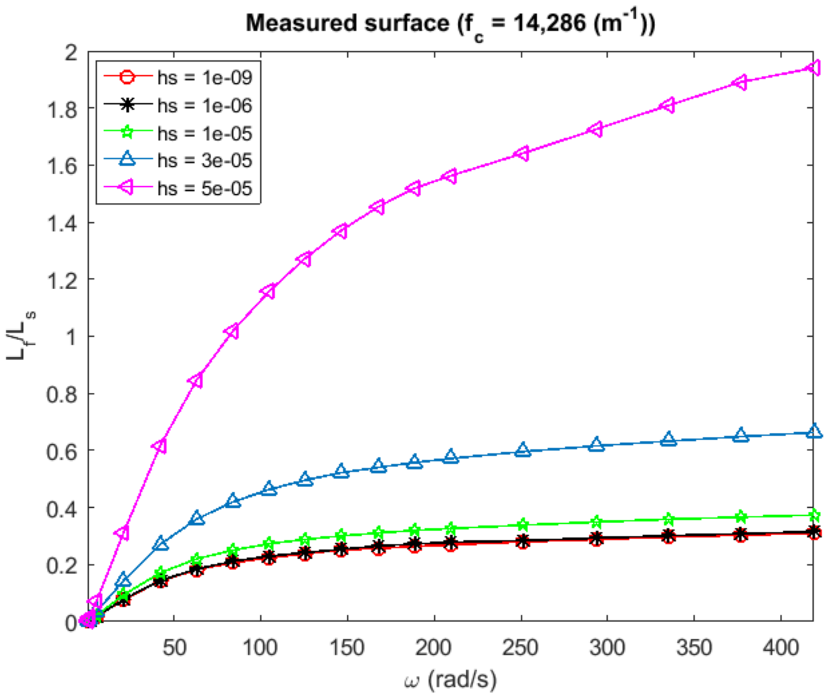

Fig.90 - Relationship between the ratio (L_f/L_s) of the load carrying capacity from fluid and the load carrying capacity from solid contact and the angular velocity (ω) at different initial surface separations for the measured surface

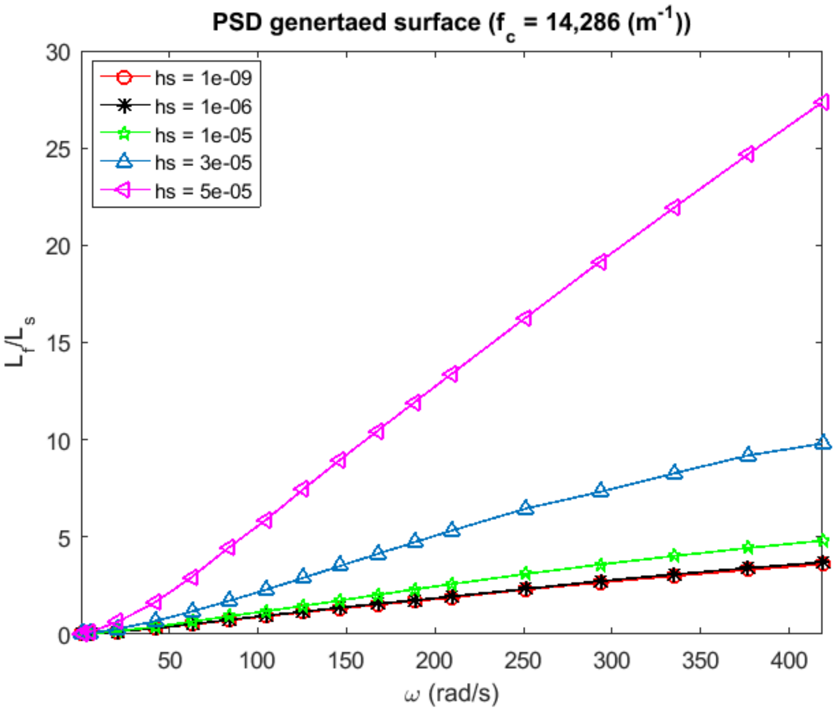

Fig.91 - Relationship between the ratio (L_f/L_s) of the load carrying capacity from fluid and the load carrying capacity from solid contact and the angular velocity (ω) at different initial surface separations for the PSD generated surface

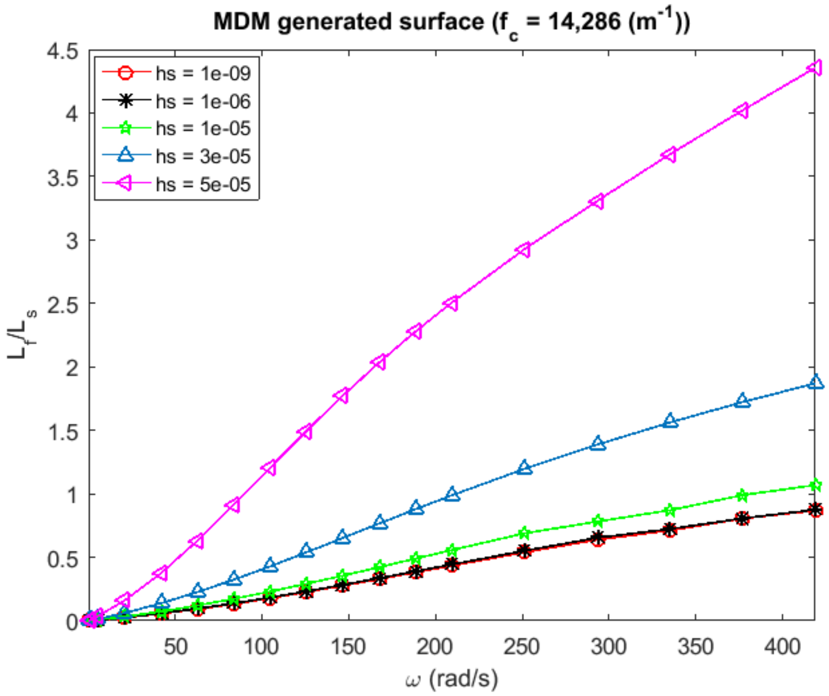

Fig.92 - Relationship between the ratio (L_f/L_s) of the load carrying capacity from fluid and the load carrying capacity from solid contact and the angular velocity (ω) at different initial surface separations for the MDM generated surface

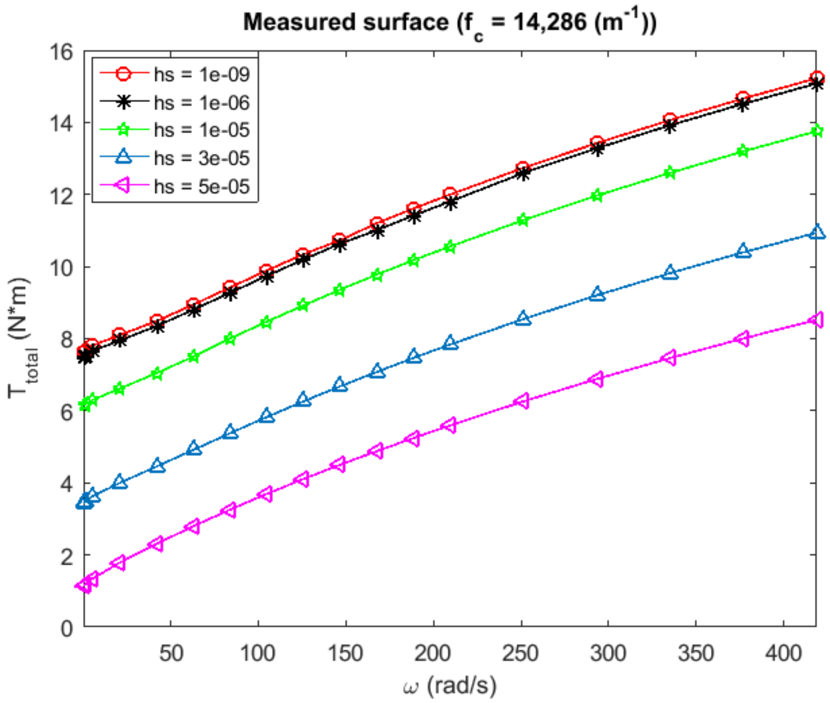

Fig.93 - Relationship between the total frictional torque (T_{total}) and the angular velocity (ω) at different initial surface separations for the measured surface

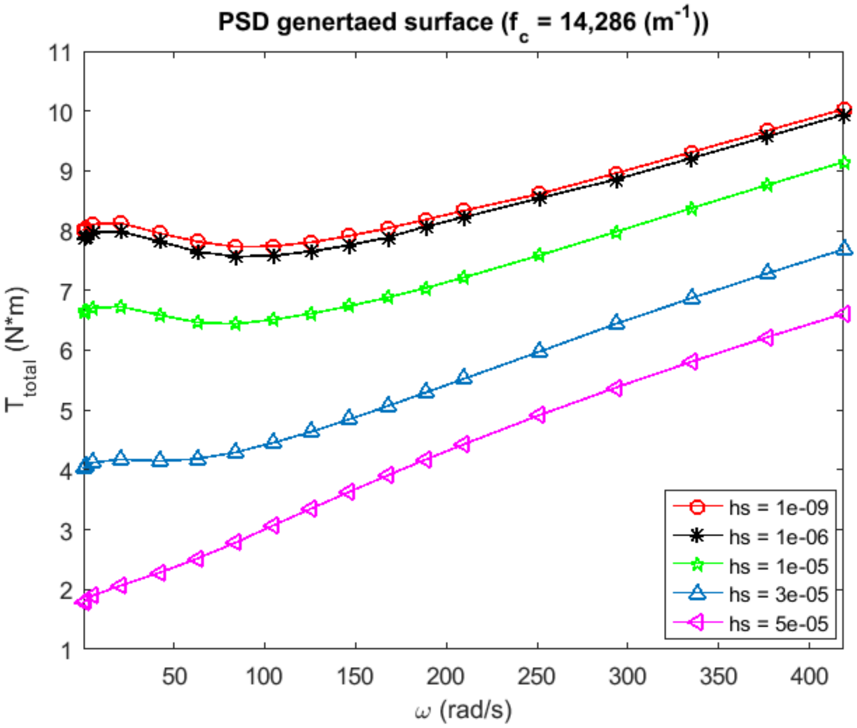

Fig.94 - Relationship between the total frictional torque (T_{total}) and the angular velocity (ω) at different initial surface separations for the PSD generated surface

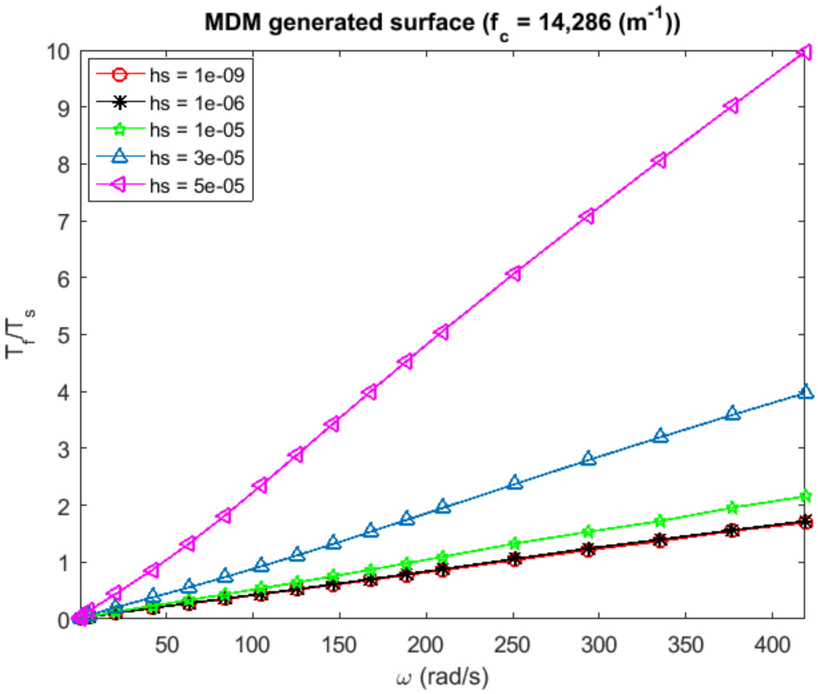

Fig.95 - Relationship between the total frictional torque (T_{total}) and the angular velocity (ω) at different initial surface separations for the MDM generated surface

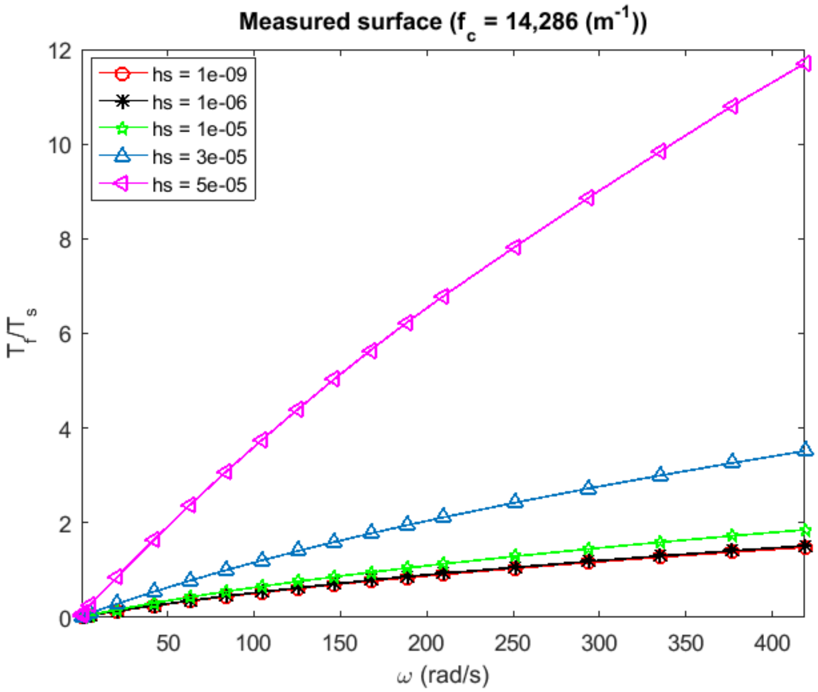

Fig.96 - Relationship between the ratio (T_f/T_s) of the frictional torque from fluid and the frictional torque from solid contact and the angular velocity (ω) at different initial surface separations for the measured surface

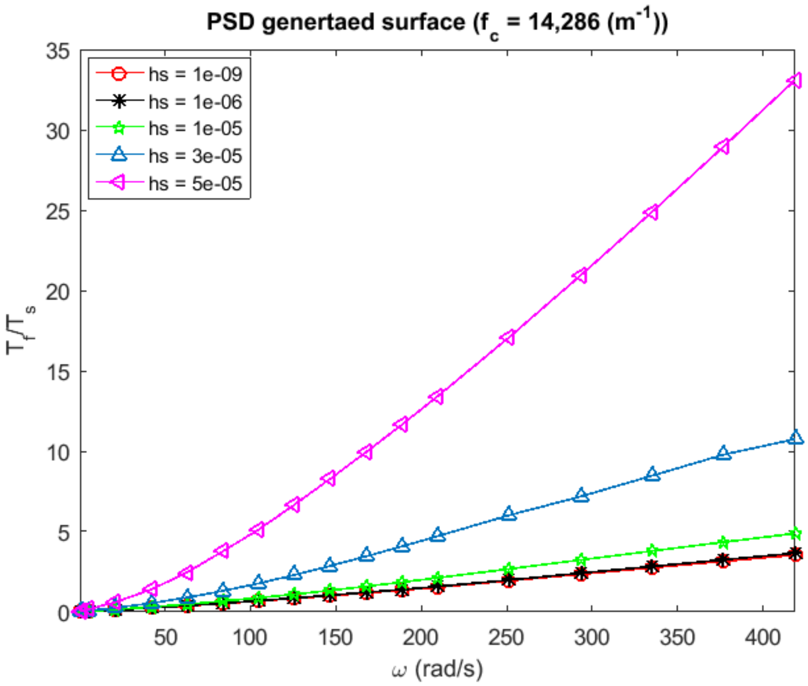

Fig.97 - Relationship between the ratio (T_f/T_s) of the frictional torque from fluid and the frictional torque from solid contact and the angular velocity (ω) at different initial surface separations for the PSD generated surface

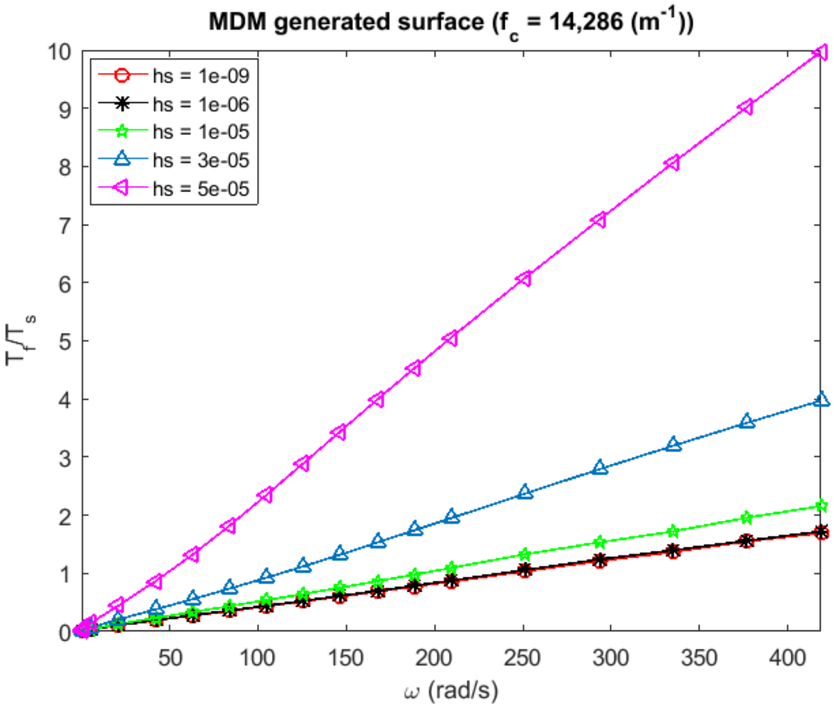

Fig.98 - Relationship between the ratio (T_f/T_s) of the frictional torque from fluid and the frictional torque from solid contact and the angular velocity (ω) at different initial surface separations for the PSD generated surface

According to Figs. 84, 85 and 86, the contact area ratio decreases with the increase of the initial surface separation for the same angular velocity, which means the solid contact between asperities decreases for these three surfaces, as expected.

As we discussed above, the load carrying capacity, the frictional torque, the ratios (L_f/L_s and T_f/T_s) all increase with the increase of the angular velocity for these three surfaces. The load carrying capacity and the frictional torque values decrease with the increase of the initial surface separation when the same angular velocity value is picked up for these five situations according to Figs. 87-89 and Figs. 93-95, which means less asperities come into contact when the initial surface separation becomes large for these three surfaces.

However, the ratios (L_f/L_s and T_f/T_s) increase with the increase of the initial surface separation for a constant angular velocity according to Figs. 90-92 and Figs. 96-98. Therefore, the higher the initial surface separation value is set, the more contribution of the fluid for the load carrying capacity and the frictional torque value provides for these three surfaces.

In addition, the thrust bearing tends to be a hydrodynamic bearing with the increase of the angular velocity and the same phenomena still have happened when the angular velocity becomes larger for these three surfaces. Hence, the initial surface separation value can also influence the performance of a thrust bearing under hydrodynamic lubrication regime.

7.4 Influence of the Small Scale Roughness and Large Scale Roughness

Meanwhile, two new surfaces (surface A and surface B) are also constructed based on the small scale roughness and the large scale roughness of the measured surface and the PSD generated surface using the following method (see Figs. 99 and 100):

(1) Surface A: combine large scale roughness from the measured surface with small scale roughness from the PSD generated surface;

(2) Surface B: combine small scale roughness from the measured surface with large scale roughness from the PSD generated surface.

This analysis allows one to determine which scale of roughness is more important and which can be generated.

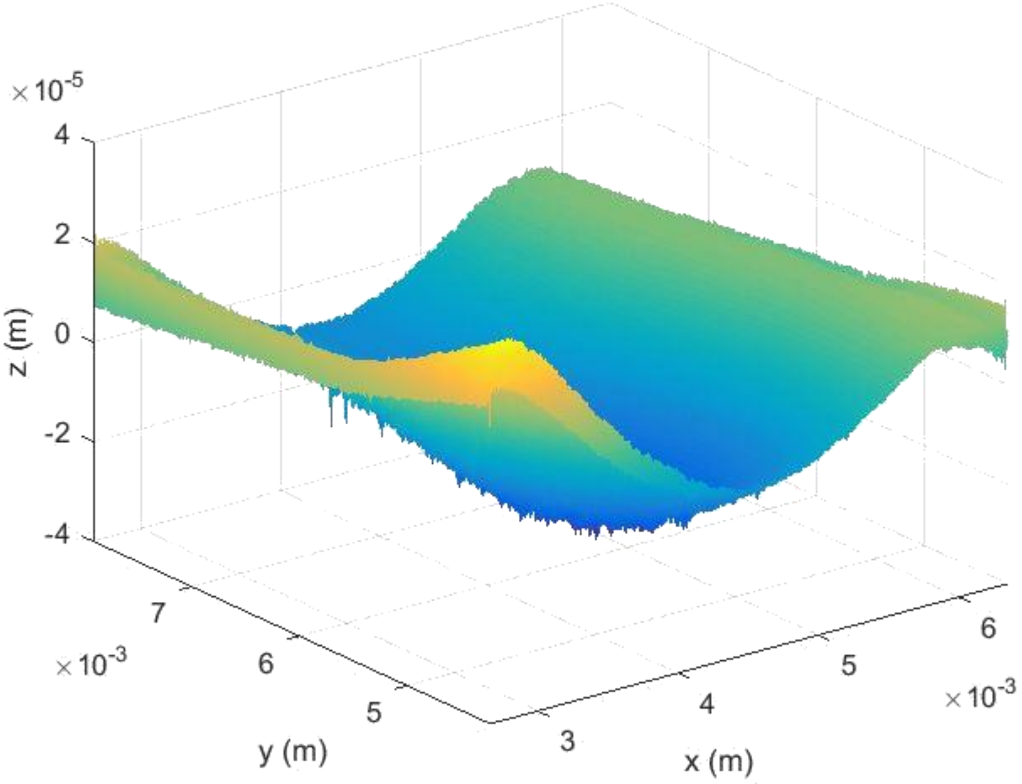

Fig.99 - New generated surface (surface A) based on large scale roughness of the measured surface data and small scale roughness of the PSD generated surface data

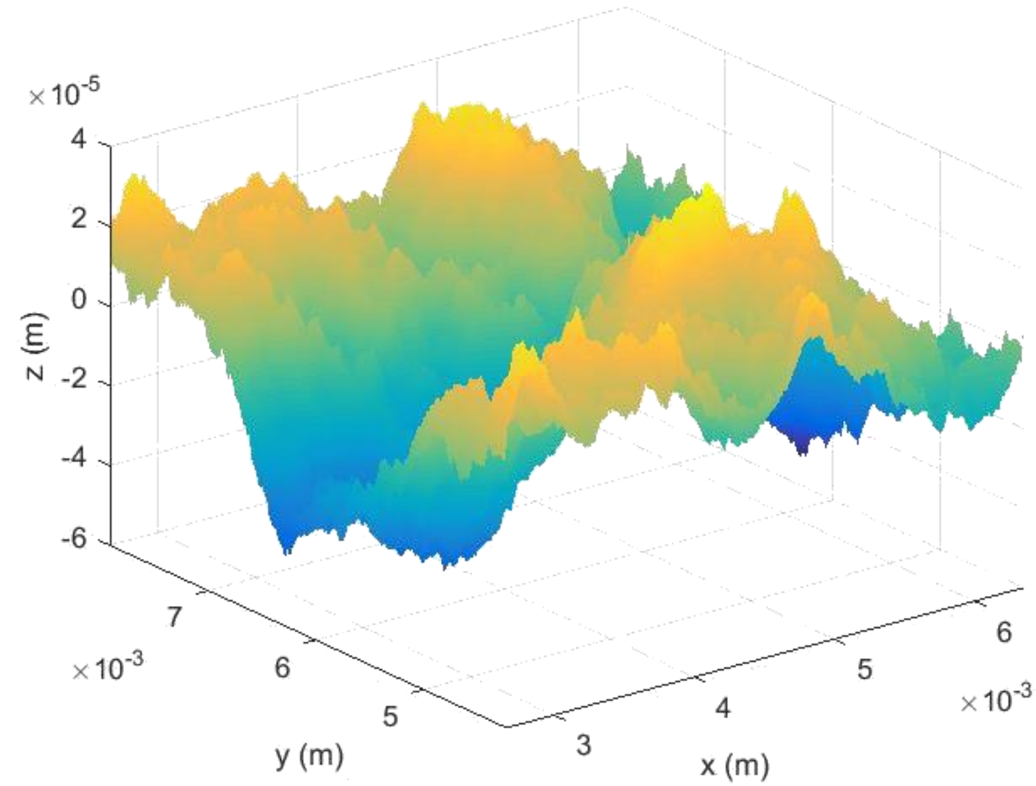

Fig.100 - New generated surface (surface B) based on the small scale roughness of the measured surface data and large scale roughness of the PSD generated surface data

Table 11 - Related parameters calculated for surface A, surface B, the measured surface and the PSD generated surface

	Surface A	Surface B	Measured surface	PSD generated surface
Root mean square (R_q)	1.1063×10^{-5} m	1.2617×10^{-5} m	1.1074×10^{-5} m	$1.2619e\times10^{-5}$ m
Kurtosis (K)	2.9026	7.2077	2.8980	7.2189
Skewness (Sk)	0.0941	-1.0911	0.0908	-1.0941
Asperity radius (R_A)	1.2375×10^{-5} m	1.1096×10^{-5} m	1.1096×10^{-5} m	1.2370×10^{-5} m
Asperity density (η_s)	2.6728×10^{10} m^{-2}	$3.5170e\times10^{10}$ m^{-2}	3.5170×10^{10} m^{-2}	$2.6728e\times10^{10}$ m^{-2}
Fractal dimension (D)	2.51	2.16	2.23	2.23

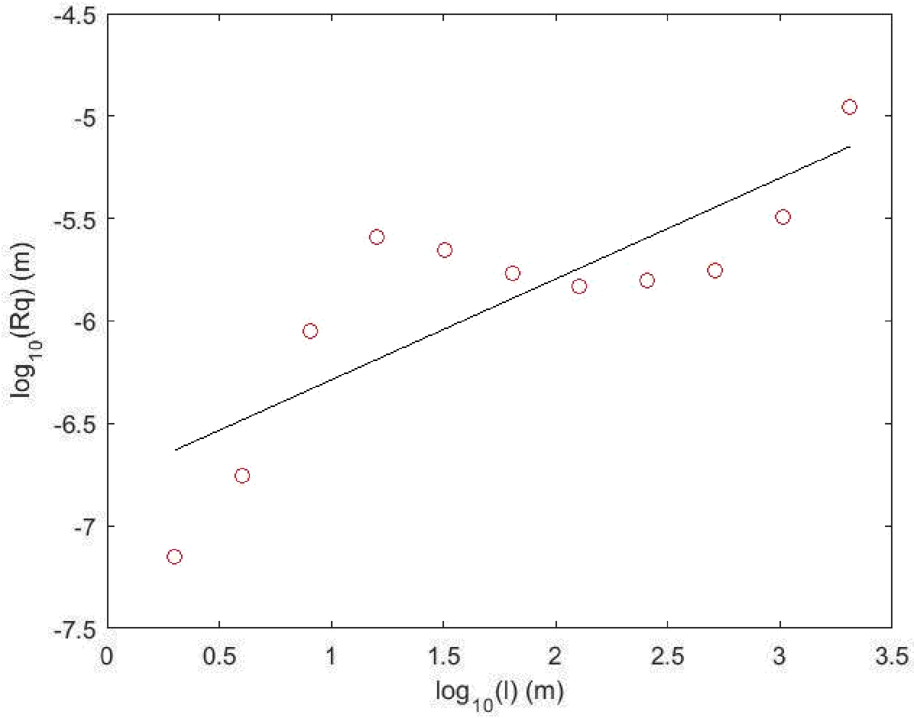

Fig.101 - Plot of the roughness-length method in calculating fractal dimension value for surface A

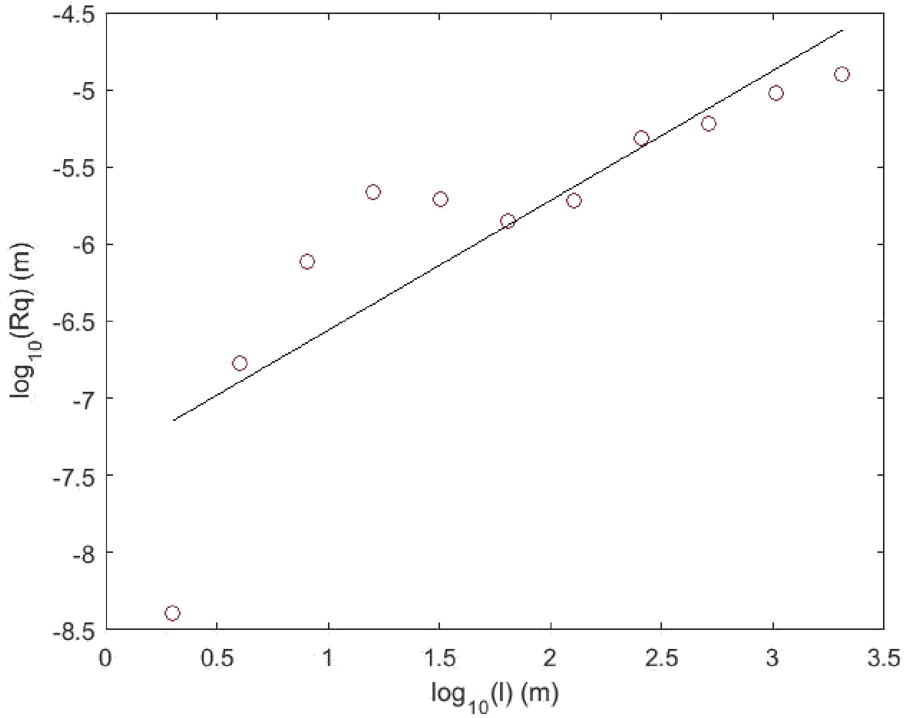

Fig.102 - Plot of the roughness-length method in calculating fractal dimension value for surface B

Table 12 - Some parameters calculated based on different cut-off frequencies

	surface A				surface B			
f_c (m^{-1})	Rq (m)	Sk	K	D	R_q (m)	Sk	K	D
5.00e04	1.1067×10^{-5}	0.0939	2.9026	2.5895	Rq (m)	-1.0917	7.2096	2.3775
3.33e04	1.1063×10^{-5}	0.0941	2.9026	2.5074	1.2619×10^{-5}	-1.0911	7.2077	2.1587
2.50e04	1.1060×10^{-5}	0.0942	2.9030	2.4358	1.2617×10^{-5}	-1.0906	7.2059	2.1646
2.00e04	1.1057×10^{-5}	0.0944	2.9035	2.4127	1.2615×10^{-5}	-1.0902	7.2043	2.1400
1.67e04	1.1055×10^{-5}	0.0945	2.9037	2.3962	1.2613×10^{-5}	-1.0899	7.2028	2.1235
1.43e04	1.1053×10^{-5}	0.0945	2.9037	2.3713	1.2610×10^{-5}	-1.0897	7.2016	2.1134
1.25e04	1.1051×10^{-5}	0.0945	2.9039	2.3532	1.2607×10^{-5}	-1.0897	7.2017	2.1034
1.11e04	1.1049×10^{-5}	0.0944	2.9043	2.3414	1.2604×10^{-5}	-1.0894	7.2000	2.0810
1.00e04	1.1047×10^{-5}	0.0943	2.9045	2.3414	1.2600×10^{-5}	-1.0896	7.1997	2.0717
5.00e03	1.1039×10^{-5}	0.0924	2.9065	2.3018	1.2596×10^{-5}	-1.0920	7.2059	2.0559
3.33e03	1.1036×10^{-5}	0.0882	2.9008	2.2932	1.2547×10^{-5}	-1.0986	7.2266	2.0620
2.50e03	1.1036×10^{-5}	0.0814	2.8894	2.2816	1.2485×10^{-5}	-1.1041	7.2697	2.0648
2.00e03	1.1042×10^{-5}	0.0745	2.8700	2.2799	1.2411×10^{-5}	-1.1253	7.2823	2.0725
1.67e03	1.1045×10^{-5}	0.0647	2.8484	2.2848	1.2324×10^{-5}	-1.1428	7.2957	2.0900
1.43e03	1.1049×10^{-5}	0.0532	2.8149	2.2826	1.2235×10^{-5}	-1.1562	7.5180	2.1101
1.25e03	1.1061×10^{-5}	0.0310	2.7518	2.2869	1.2090×10^{-5}	-1.2293	7.7008	2.1328
1.11e03	1.1061×10^{-5}	0.0310	2.7518	2.2869	1.1898×10^{-5}	-1.2293	7.7008	2.1328
1.00e03	1.1082×10^{-5}	-0.0035	2.6532	2.2870	1.1898×10^{-5}	-1.2700	7.8841	2.2058
5.00e02	1.1479×10^{-5}	-0.1753	2.7466	2.2768	1.1601×10^{-5}	-1.6790	11.685	2.2861
3.33e02	1.1479×10^{-5}	-0.1753	2.7466	2.2768	8.9553×10^{-5}	-1.6790	11.685	2.2861

Small scale roughness and large scale roughness are determined based on the cut-off frequency. Surface A and surface B shown in Figs. 99 and 100 are generated when the cut-off frequency is 33,300 m^{-1}. For these two shown surfaces, the same basic parameters and the fractal dimension value from the roughness-length method [34] are calculated (see Table 11). Fig.101 and Fig.102 show the plots of the roughness-length method in calculating the fractal dimension value for these two combined surfaces. Table 12 shows the basic parameters and the fractal dimension value for surface A and surface B with different cut-off frequencies.

The measured surface and surface A have similar values of *Rq*, *Sk* and *K*, and the values of *Rq*, *Sk* and *K* for the PSD generated surface and surface B are similar based on Table 11, which means large scale roughness tends to dominate the calculation process of the statistical parameters.

By changing the initial surface separation and the cut-off frequency (angular velocity keeps constant) of the measured surface, the PSD generated surface, surface A, and surface B, the changing trend between the cut-off frequency and the total load carrying capacity and the total frictional torque for some cases are plotted (see Fig.103 and Fig.104), the other cases are shown in Appendix C and Appendix D.

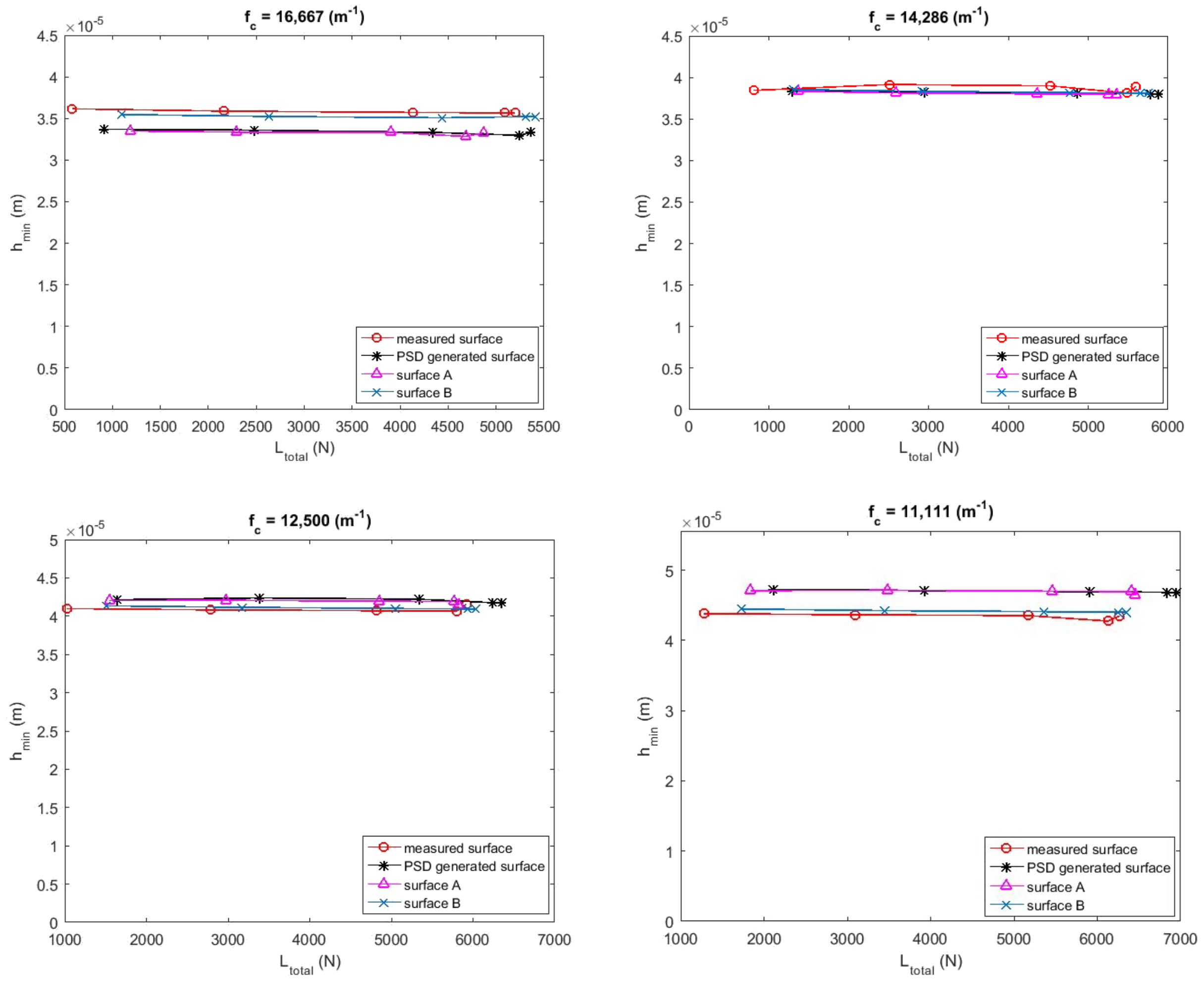

Fig.103 - Changing trend between the minimum film thickness (h_{min}) and the total load carrying capacity (L_{total})

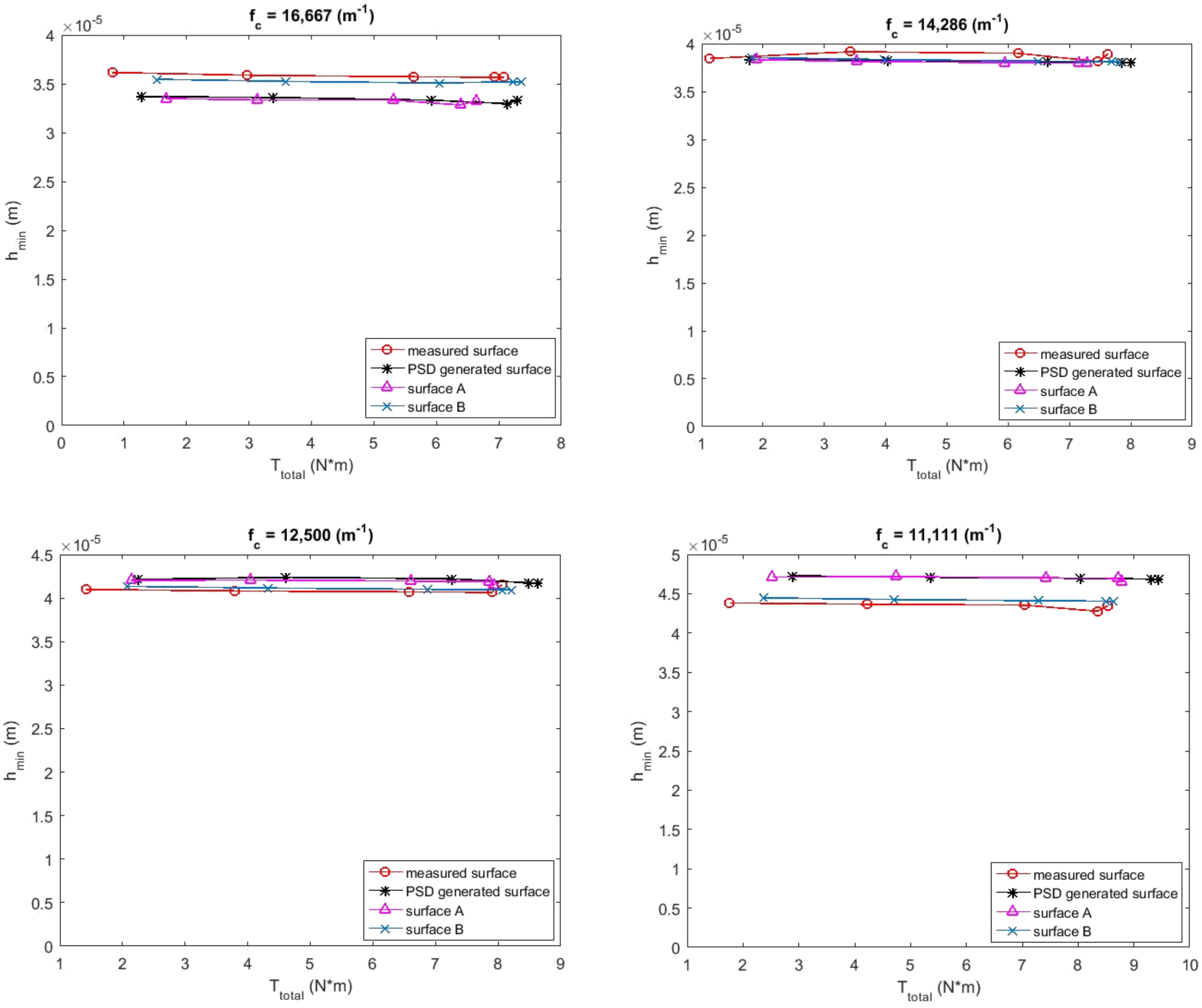

Fig.104 - Changing trend between the minimum film thickness (h_{min}) and the total frictional torque (T_{total})

When the cut-off frequency is smaller, the values of the load carrying capacity and the frictional torque predicted by the PSD generated surface are smaller than the values from the measured surface according to Fig.103 and Fig.104. With the growth of the cut-off frequency, the load carrying capacity value and the frictional torque value become larger than the values calculated from the measured surface.

As we mentioned above, the small scale roughness of surface A is from the PSD generated surface and the small scale roughness of surface B is from the measured surface. The trend lines of the total load carrying capacity and the frictional torque for the measured surface and surface B are very close, and the trend lines for the PSD generated surface and surface A are the same. Therefore, the small scale roughness appears to be dominant in the mixed lubrication regime.

In addition, it is important to understand the physical meaning of the different values of the fractal dimension when discussing the results. According to Majumdar and Bhushan [46], the surface fractal dimension (D_s) can be related to the profile fractal dimension (D_p) by using $D_s = 1+D_p$. It has already been shown in our previous work [32, 33] that the fractal dimension value for a self-similar surface profile is 1. Therefore, the fractal dimension for a self-similar surface should be 2. Note that a surface profile is one line of a 3-D surface.

By comparing the fractal dimension value in Table 8 and Table 10, it can be seen that the measured surface, the PSD generated surface, the MDM generated surface and surface B tend to be self-similar. Nonetheless, the parameter values listed in Table 11 is based on the specific case (f_c = 33,300 m^{-1}), different cut-off frequencies are changed to verify the influence of cut-off frequency on some parameters listed in Table 11 and the values are listed in Table 12.

It can be found from Table 12 that the values of *Rq*, *K* and *Sk* for surface A and surface B do not change significantly with the changing of the cut-off frequency, except at low cut-off frequencies, which are near to the macro scale geometry and would not typically be used (see Figs. 105, 106 and 107). It can be found from Fig.105 that the R_q value for surface A decreases with the increase of the cut-off frequency, and the R_q value for surface B increase with the growth of the cut-off frequency. At larger cut-off frequency, the decrease speed for surface A and the increase speed for surface B slow down. The *Sk* value for both of surface A and surface B increase with the increase of the cut-off frequency according to Fig.106, the slope of the changing line becomes smaller and smaller as the increase of the cut-off frequency. Different from the changing trend of R_q value for surface A and surface B, K value for surface A increase and K value for surface B decrease with the growth of the cut-off frequency based on Fig.107. Similarly, the changing speed of K value for both of these two surfaces becomes slow down when the cut-off frequency becomes large.

However, the fractal dimension value is influenced significantly by the changing of the cut-off frequency. Fig.108 shows the relationship between the cut-off frequency and the fractal dimension value for surface A and surface B based on Table 12.

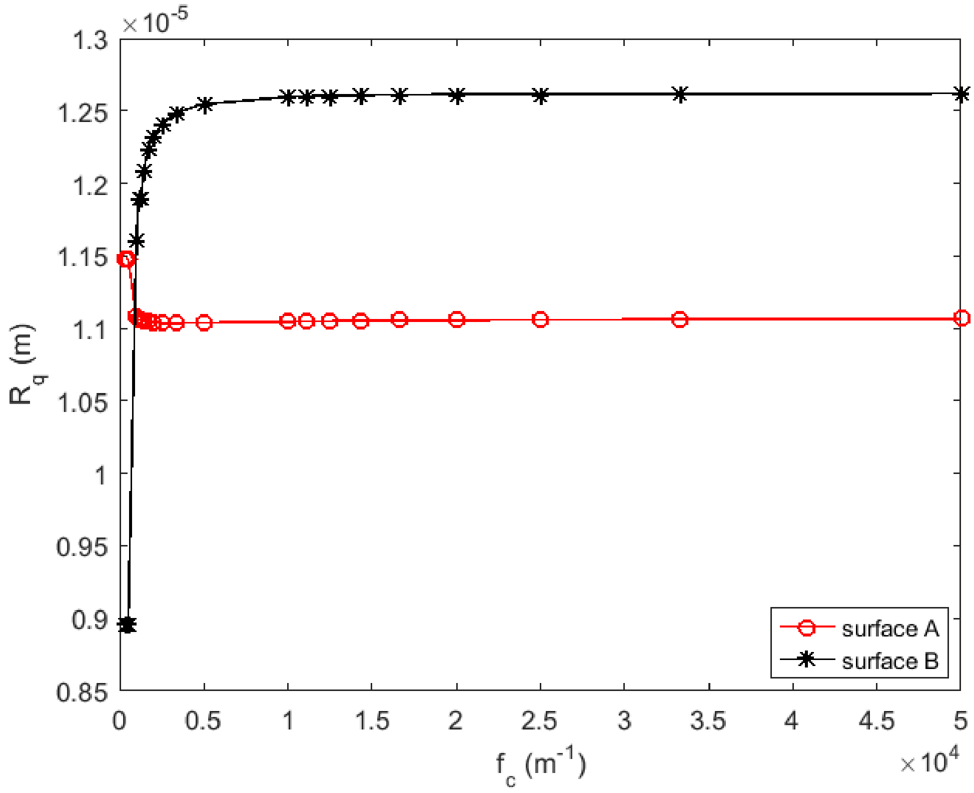

Fig.105 - Relationship between the cut-off frequency (f_c) and the RMS roughness (R_q)

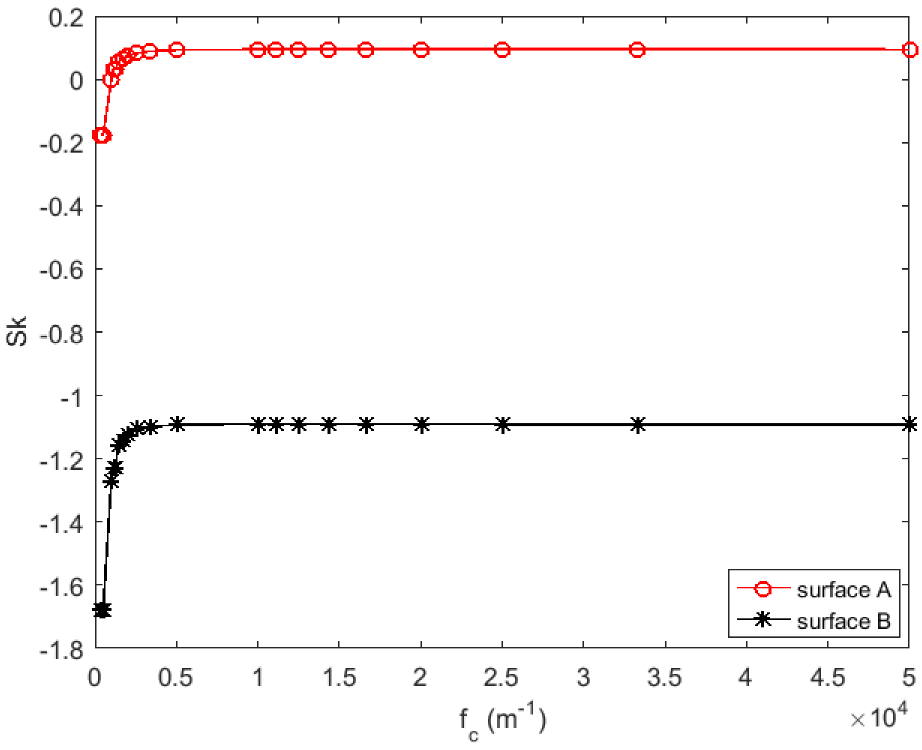

Fig.106 - Relationship between the cut-off frequency (f_c) and the Skewness (*Sk*)

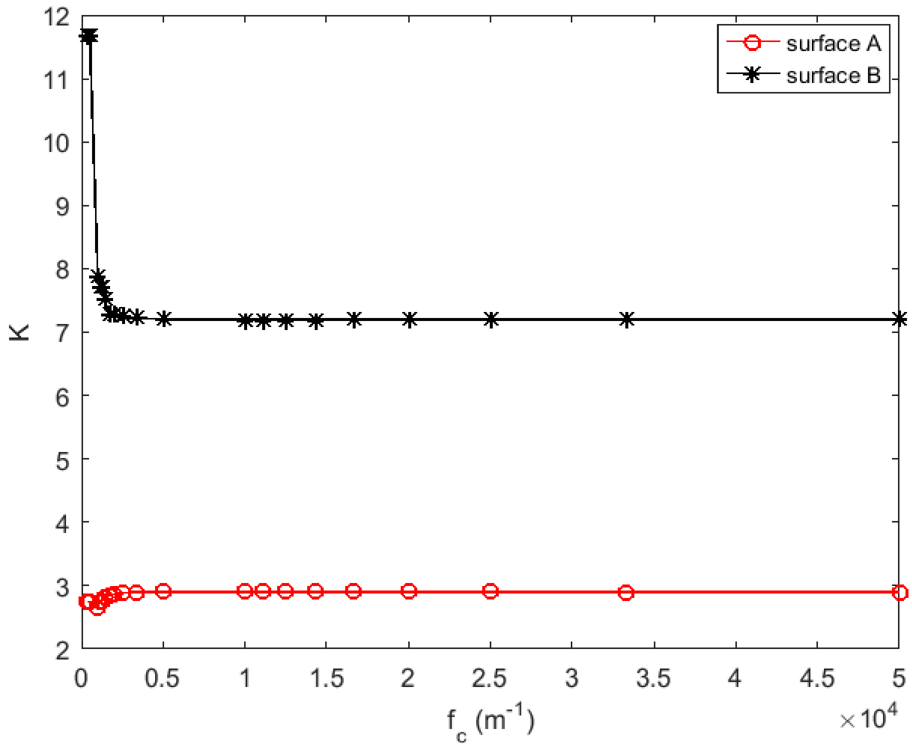

Fig.107 - Relationship between the cut-off frequency (f_c) and the Kurtosis (*K*)

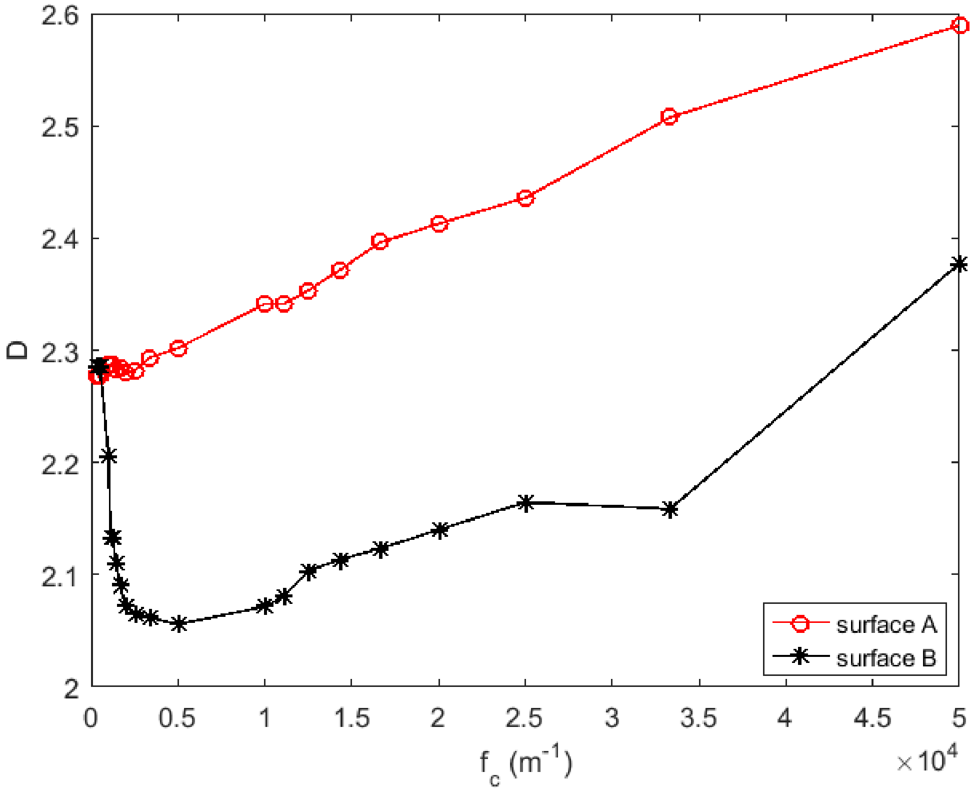

Fig.108 - Relationship between the cut-off frequency (f_c) and the fractal dimension (D)

According to Fig.108, fluctuation happens in the fractal dimension value with the increase of the cut-off frequency. It can be concluded by comparing Figs. 105-108 that fractal dimension actually varies more than roughness or statistical values with scale, which means that the fractal dimension depends on the chosen cut-off frequency and it is not always a reliable parameter in characterizing the rough surface.

7.5 Conclusions

The shear rate of the fluid increases with the increase of the angular velocity, so that the shear stress increases. As a result, the load carrying capacity and the frictional torque values from the real surface, the PSD generated surface and the MDM generated surface all increase but at different amounts. The proportions of the load carrying capacity and the frictional torque from fluid have also increased for the measured surface, the PSD generated surface and the MDM generated surface with the growth of the angular velocity. However, the ratios (L_f/L_s and T_f/T_s) from the PSD generated surface has been the largest for all angular velocities and the ratios (L_f/L_s and T_f/T_s) from the measured surface becomes the smallest for larger angular velocities. Therefore, when the angular velocity increases large enough, the contact area of the measured surface is larger than the other two generated surfaces at the same angular velocity value. This suggests that the angular velocity has a greater influence on the two generated surfaces and that the two surface generation methods are not suitable in representing the measured surface.

When the cut-off frequency used in deconstructing the surface is small, the PSD generated surface is relatively better in representing the measured surface. Whereas, when the cut-off frequency becomes larger, the MDM generated surface can represent the measured surface better, but they both represent the measured surface poorly.

The load carrying capacity value and the frictional torque value calculated for the measured surface, the PSD generated surface and the MDM generated surface are not the same and the load carrying capacity ratio from the fluid and from the solid contact for these three surfaces increases differently, which means it should be considered carefully whether generated surface based on the fractal dimension can be used to represent a measured surface. It should be mentioned again that only a few generated surfaces are evaluated due to the computational limitations, therefore the results cannot be considered generalized.

Meanwhile, this work suggests that the fractal dimension is unreliable when it is the only parameter to characterize the measured surface since the results for the fractal surface and the measured surface differ significantly and it also changes with the chosen angular velocity and cut-off frequency. It should also be noted that the small scale roughness is dominant in the mixed lubrication regime and large scale roughness affects a lot in the calculation process of the statistical parameters.

Although the input parameters for the generated rough surfaces are from the measured rough surface, some surface properties changed during the generation procedure, which implies that the surface generation methods we used in our work need to be improved and new methods need to be developed.

Chapter 8

SURFACE OPTIMIZATION

8.1 Optimization Process

It has been concluded that the small scale roughness is the dominant part of the geometry in the mixed lubrication regime from Chapter 7. The influence of the large scale geometry on the load carrying capacity is investigated in this chapter. The objective of this chapter has been to maximize the load carrying capacity from the fluid (L_f) on a surface by combining the small scale roughness from the measured surface and the large scale geometry from a designed equation. Based on the shape of the measured surface in Fig.49, the large scale geometry equation might be approximated as:

$$z_{large} = (a\theta^2 + b\theta + c) \times (dr^2 + er + f) \tag{59}$$

where a, b, c, d, e and f are constants. These six unknowns can be represented by two unknowns when the following boundary conditions below are applied:

$$z_{large}(r, \theta_0) = z_{large}(r, \theta_1) = 0 \tag{60}$$

$$z_{large}(r_i, \theta) = z_{large}(r_o, \theta) = 0 \tag{61}$$

where θ_0 and θ_1 are angles at two boundaries of the thrust bearing in the circumferential direction; r_i and r_o are the inner and outer radius of the thrust bearing. In these two boundary conditions, the height at four edges of the thrust bearing is set to be zero.

By applying these boundary conditions and set $b = e$, Eq. (59) can be written as:

$$z_{large} = (-14.2526b\theta^2 + b\theta + 0.0031b) \times (-9.9509br^2 + br - 0.0251b) \tag{62}$$

Fig.109 shows the plot of the large scale geometry (b = 5) generated by Eq. (62). Fig.110 shows the optimized surface by combining the small scale roughness from the measured surface with the large scale geometry generated by Eq. (62). During the optimization process, the cutoff frequency is kept consistent for the small scale roughness from the measured surface and large scale geometry from Eq. (62), which is $f_c = 14{,}286\ m^{-1}$.

During the numerical process for the new combined surface, the total load carrying capacity is kept constant while the average film thickness is allowed to vary for a better investigation of the large scale geometry. Therefore, a load balance is required in the code. The numerical calculation process with the load balance part is used which is shown in Fig.111. It should be noted that the temperature influence part is neglected in this numerical process so that computational time can be reduced.

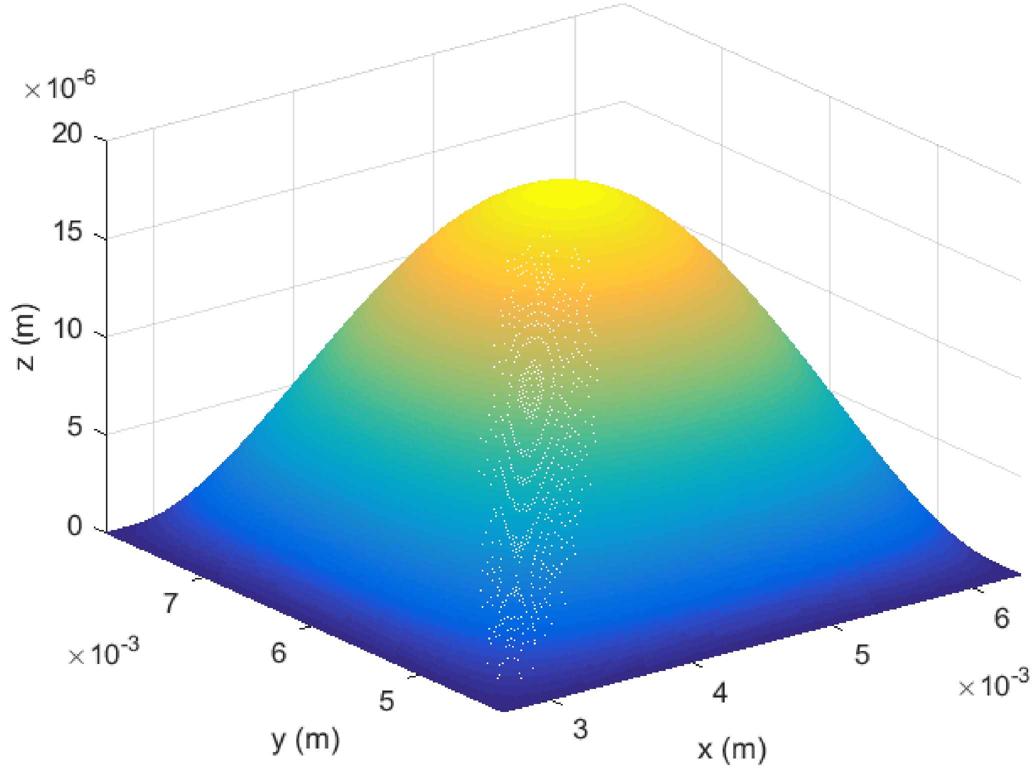

Fig.109 - Large scale geometry generated by Eq.(62) (b = 5, $f_c = 14{,}286\ m^{-1}$)

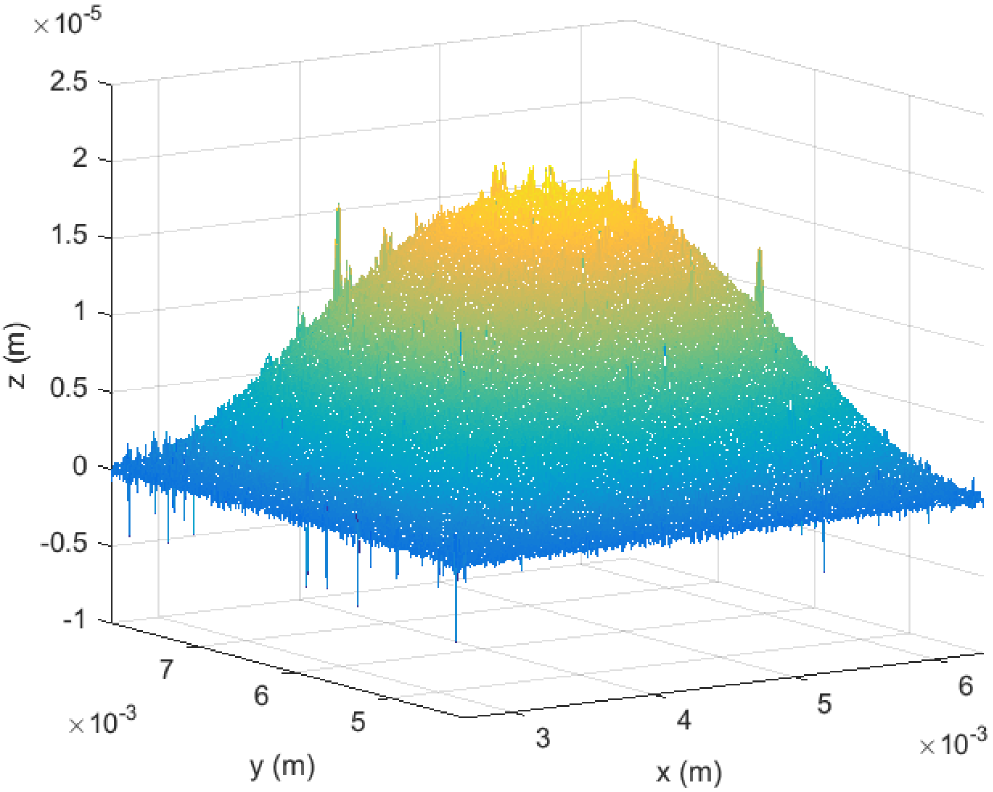

Fig.110 - Sample of generated surface ($b = 5$, $f_c = 14{,}286\ m^{-1}$)

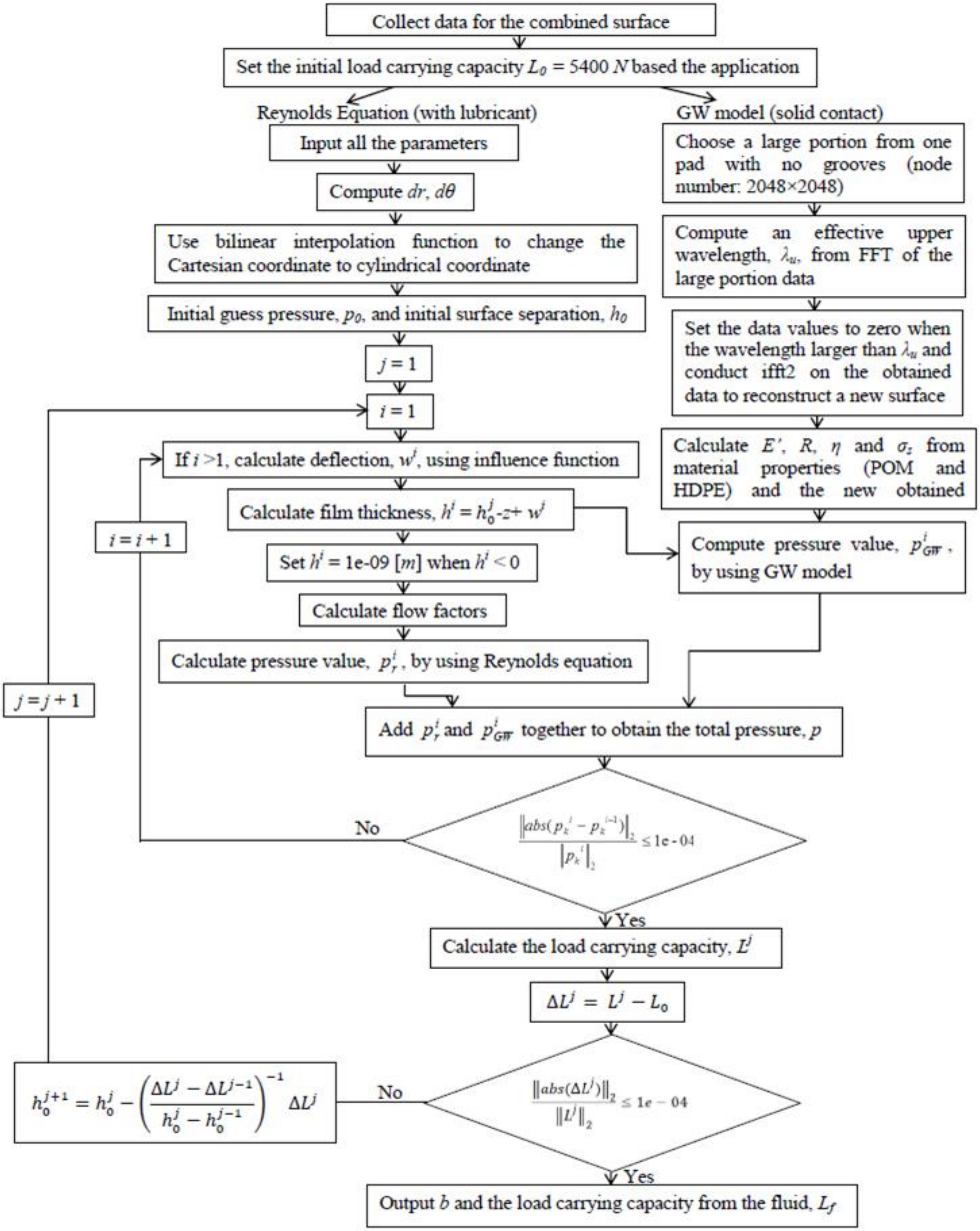

Fig.111 - Flow chart of calculation process with load balance

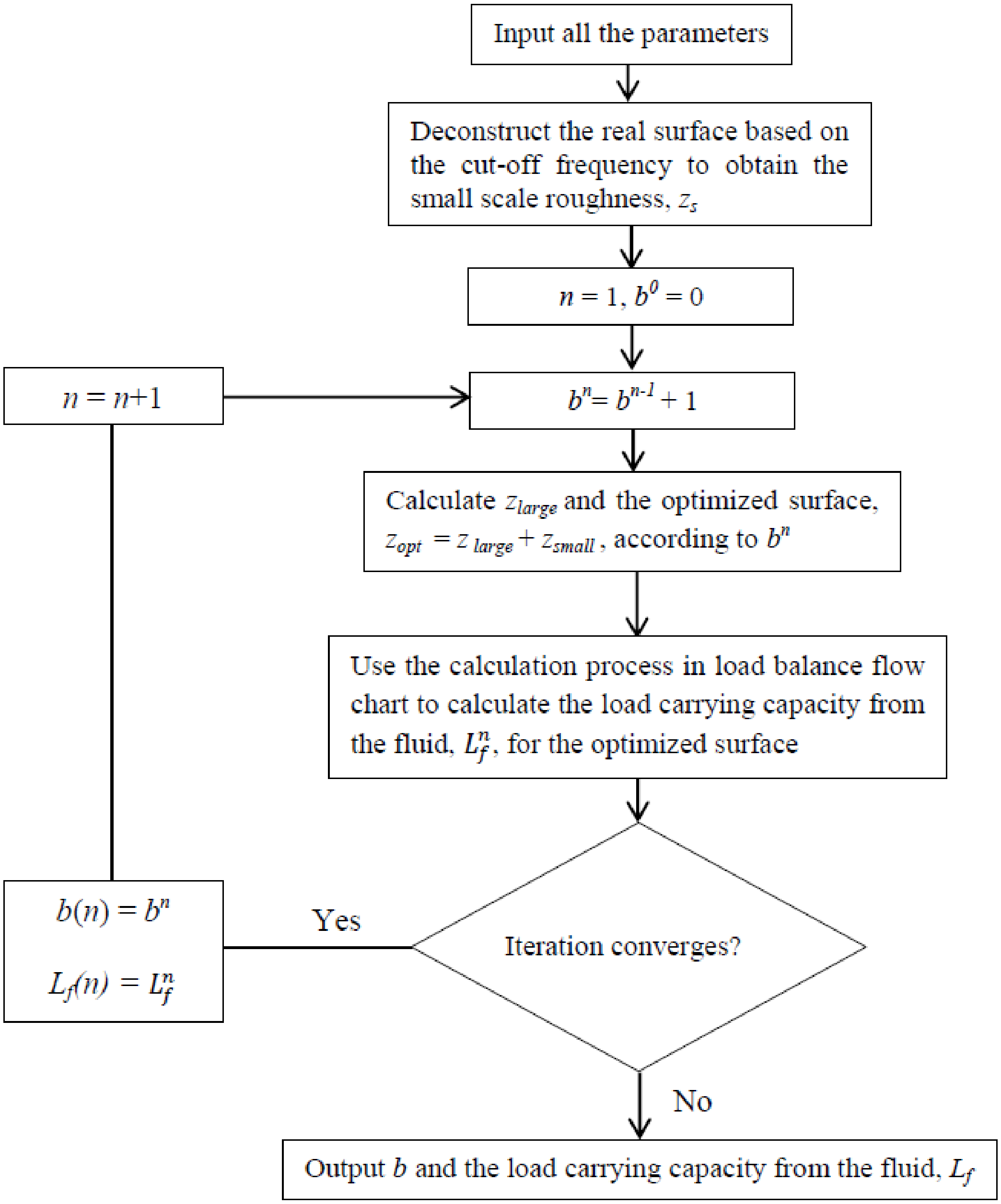

Fig.112 - Flow chart of optimization process

Fig.112 shows the flow chart of the entire optimization process. Since b is the only unknown in Eq. (62), b is set to an initial value of 1 with an increment 1 in this optimization process (the cutoff frequency is 14,286 m^{-1} and the initial surface separation is 1 μm in this process). By using the load balance calculation process in Fig.111, the load carrying capacity from fluid (L_f) for a relative *b* can be calculated. The optimization process is terminated until the iteration in Fig.111 cannot converge.

8.2 Results and Discussions

After *b* value and its relative load carrying capacity from fluid value (L_f) are obtained, the relationship between *b* and L_f can be plotted, which is shown in Fig.113. Meanwhile, Figs. 114 and 115 show the influence of b on L_f/L_s and minimum film thickness with deflection (h_{min}) respectively.

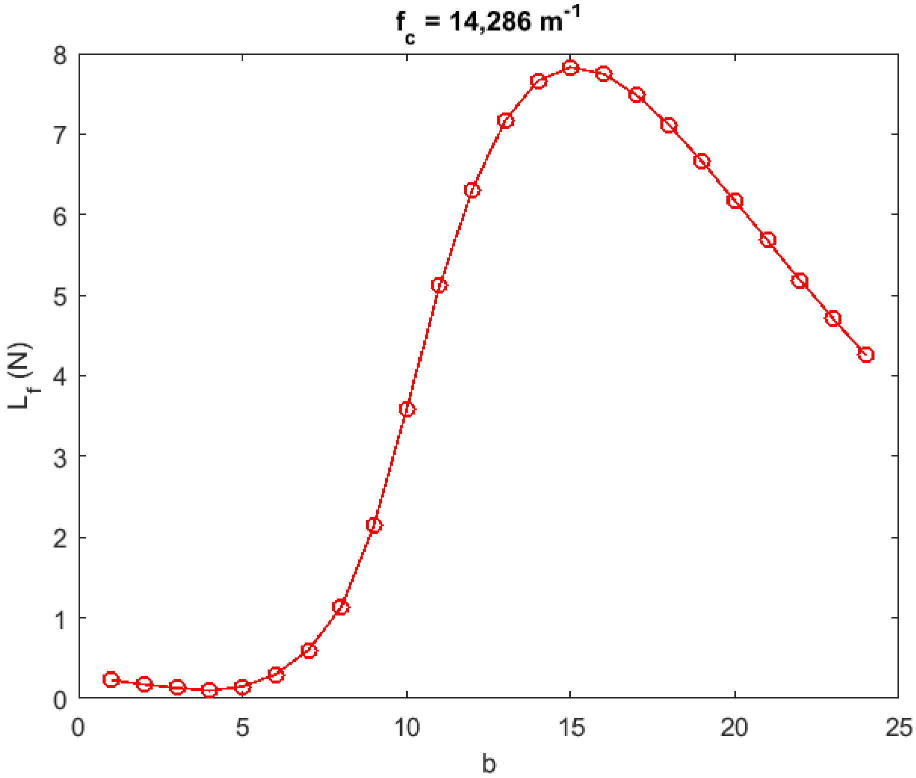

Fig.113 - Relationship between *b* and load carrying capacity from fluid (L_f)

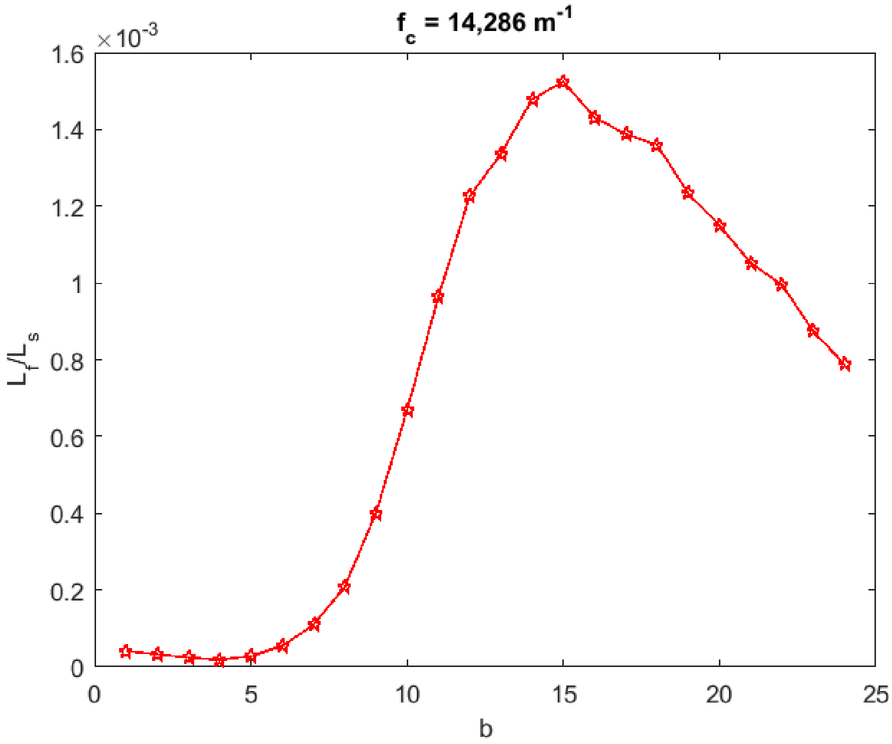

Fig.114 - Relationship between *b* and the ratio between the load carrying capacity from fluid (L_f) and the load carrying capacity from solid contact (L_s)

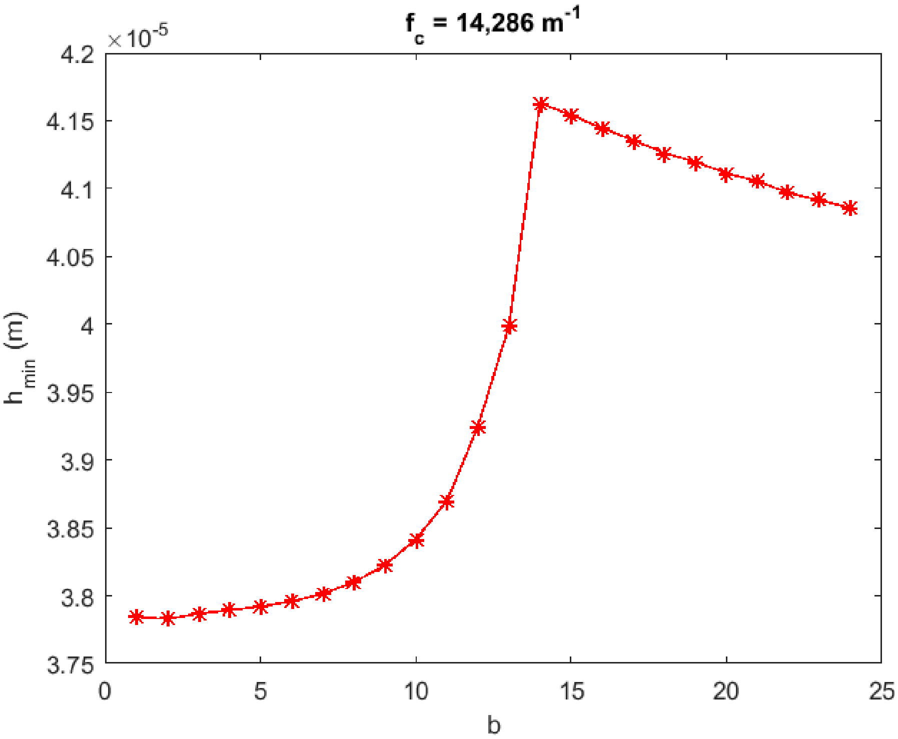

Fig.115 - Relationship between *b* and minimum film thickness with defection (h_{min})

It can be found from Fig.113 that when $b = 15$, the load carrying capacity from the fluid (L_f) has the largest value which means the surface can be optimized. However, this is not the optimal value, but is close to it. The proportion of the load carrying capacity from fluid increases with the increase of the b value, and it decreases when the b value becomes larger than 15 according to Fig.114. In addition, Fig.115 shows the changing trend of the minimum film thickness with deflection (h_{min}) is the same as the changing trend of the load carrying capacity from the fluid (L_f). Therefore, the larger the film thickness is, the more hydrodynamic part the thrust bearing has and the more load carrying capacity generated by the fluid.

Fig.116 shows the nearly optimized surface shape when $b = 15$. It should be note that the scale of the height is amplified, the actually height of the surface feature is small compared to the lengths of the lateral edges.

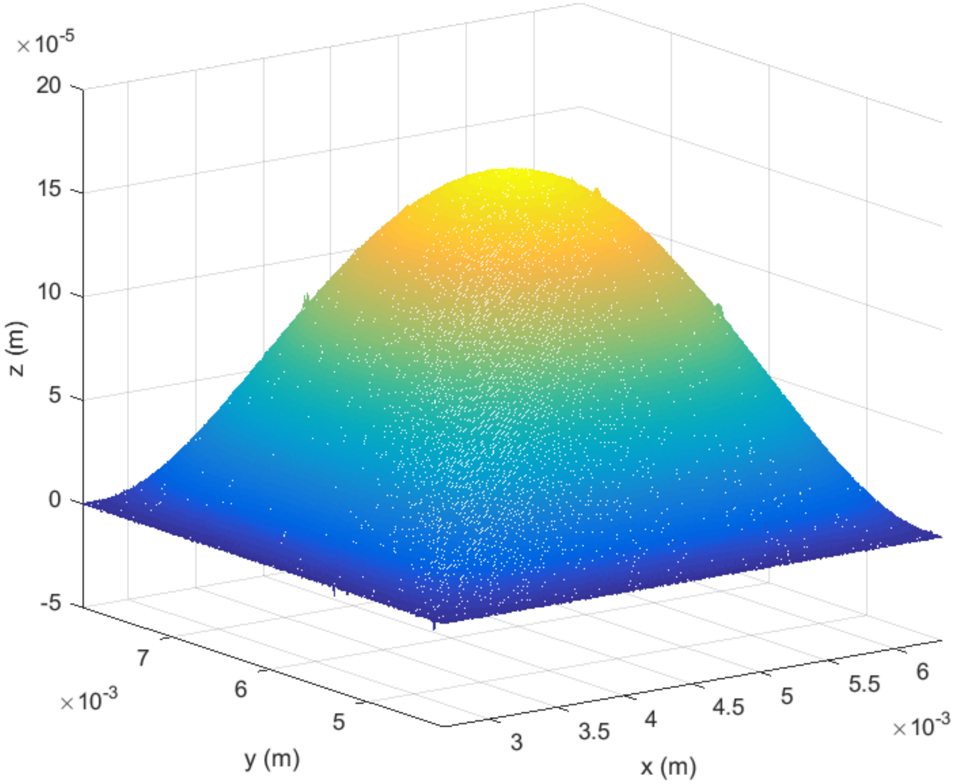

Fig.116 - Optimized surface shape when $b = 15$ ($f_c = 14{,}286\ m^{-1}$)

8.3 Conclusions

In this chapter a large scale geometry equation is derived which is used to generate an nearly optimized surface. An optimized surface is constructed by adding small scale roughness from the measured surface and large scale geometry from the large scale geometry equation. It can be found that when the unknown, *b*, in the large scale geometry equation equals to 15, the optimized surface can generate the largest load carrying capacity from fluid when the total load carrying capacity, the cut-off frequency and the initial surface separation are held constant. Therefore, the thrust bearing surface in this study can be optimized to improve the tribological performance.

However, most of surface optimization process is focused on the journal bearings [47-49] or the stepped shaped thrust bearings [50] and not too many works focused on the flat thrust bearings, this optimization process need to be improved by finding more models about the flat thrust bearing surface advanced optimization algorithm.

CHAPTER 9

CLOSURE

9.1 Conclusions

In this work, a mixed lubrication bearing model is proposed and used to evaluate different realizations of the same surface. This new model is able to provide predictions of important quantities such as frictional torque, load carrying capacity, minimum film thickness, temperature rise, and contact pressure.

The angular velocity and the cut-off frequency all have a great influence on the PSD and the MDM generated surfaces, and the surface parameters used in the two surface generation methods are not suitable in characterizing the measured surface. Therefore, it should be considered carefully if the generated surface based on the fractal dimension can be used to represent a measured surface. Meanwhile, the fractal dimension is unreliable when it is the only parameter to characterize the measured surface since it changes with the cut-off frequency, and real measured rough surfaces are not easily represented as perfect fractals as researchers and engineers often assume,

9.2 Contributions

The contributions of this work to the tribology and engineering filed can be summarized as:

1) Mixed lubrication problems (Reynolds equation) and rough surface contact (GW model) with roughness are solved and the influence of the surface roughness on the lubricant behavior is shown.

2) Generated roughness surfaces by fractal methods cannot be used to represent the real surface.

3) Fractal dimension is not a reliable parameter as researches often regarded.

4) Surface geometry can be optimized.

9.3 Future Work

The model built can make predictions of the performance indicators for the thrust bearing system. However, it still requires further development and verification by comparing with some other existing models and experimental measurements. In addition, the periodic boundary condition is the only boundary condition we considered. Additional boundary conditions, such as cavitation boundary condition, will be added in our model in the future to improve the predictions.

The lubricant we used in our work is grease, which is a non-Newtonian fluid as we discussed. However, the Reynolds equation used in this work is more often used for Newtonian fluids [27] which can only make an approximate prediction of the hydrodynamic part when the lubricant is grease. Therefore, an improvement of the model needs to be made by finding a generalized Reynolds equation that can be used in the grease EHL in the cylindrical coordinates.

Since the fractal dimension value is not a reliable parameter in characterizing rough surfaces it is necessary to find new parameters to characterize the real rough surfaces.

Although the input parameters for the generated rough surfaces are from the measured rough surface, some surface properties changed during the generation procedure, which implies that the surface generation methods we used in our experiment need to be improved and new methods need to be developed.

In addition, the surface geometry optimization process in this work needs to be improved by finding more algorithms and comparing with more models on the flat thrust bearing optimization.

REFERENCE

[1] Shi, F., Wang, Q., ‘‘A Mixed-TEHD Model for Journal-Bearing Conformal Contacts—Part I: Model Formulation and Approximation of Heat Transfer Considering Asperity Contact,’’ ASME Journal of Tribology, 120, pp. 198–205, 1998;

[2] Shi, F., Wang, Q., ‘‘A Mixed-TEHD Model for Journal-Bearing Conformal Contacts—Part II: Contact and Performance Analyses,’’ ASME Journal of Tribology, 120, pp. 206–213, 1998;

[3] Zhang, C. “TEHD Behavior of Non-Newtonian Dynamically Loaded Journal Bearings in Mixed Lubrication for Direct Problem,’’ ASME Journal of Tribology, 124, pp. 178-185, 2002;

[4] Muzakkir, S. M., Hirani, h., and Thakre, G. D., “Experimental Investigations on Effectiveness of Axial and Circumferential Grooves in Minimizing Wear of Journal Bearing Operating in Mixed Lubrication Regime,” International Journal of Current Engineering and Technology, 5(1), pp. 486-489, 2015;

[5] Raimondi, A. A., Boyd J., “A Solution for the Finite Journal Bearing and its Application to Analysis and Design: III”,ASLE Transactions, 1, 1, pp.194-209, 1958;

[6] Gao, G., Yin, Z., Jiang, D., and Zhang, X., “Numerical analysis of plain journal bearing under hydrodynamic lubrication by water”, Tribology International, 75, pp. 31-37, 2014;

[7] Kirk, R. G., Funter, E. J., “Short Bearing Analysis Applied to Rotor Dynamics—Part I: Theory”, ASME Journal of Lubrication Technology, 98, 1, pp. 47-56, 1976;

[8] Sun, J., Gui, C. “Hydrodynamic lubrication analysis of journal bearing considering misalignment caused by shaft deformation”, Tribology International, 97, 10, pp.841-848, 2004;

[9] McCallion, H., Yousif, F., and Lioyd, T., “The Analysis of Thermal Effects in a Full Journal Bearing”, ASME Journal of Lubrication Technology, 92, 4, pp. 578-587, 2010;

[10] Prakash, J., Vij, S. K., “Analysis of Narrow Porous Journal Bearing Using Beavers-Joseph Criterion of Velocity Slip”, ASME Journal of Applied Mechanics, 41, 2, pp. 348-354, 1974;

[11] Bouyer, J., Fillon, M., “An Experimental Analysis of Misalignment Effects on Hydrodynamic Plain Journal Bearing Performances”, ASME Journal of Tribology, 124, 2, pp. 313-319, 2001;

[12] Brockwell, K., Ettles, C., and Stokes, M., “A Design Method for Radially Grooved Thrust Washers”, Proceedings of the Institution of Mechanical Engineers, 184, pp. 82-92, 1969;

[13] Heshmat, H., Walowit, J. A., and Pinkus, O., “Analysis of Gas Lubricated Compliant Thrust Bearings”, ASME Journal of Lubrication Technology, 105, 4, pp. 638-646, 1983;

[14] Carpino, M., “Analysis of a Low Speed Flexible Flat Land Thrust Bearing”, ASME Journal of Tribology, 112, 4, pp. 678-683, 1990;

[15] Yu, T.H., Sadeghi, S., “Groove Effects on Thrust Washer Lubrication”, ASME Journal of Tribology, 123, 2, pp.295-304, 2000;

[16] Cameron, A., Wood, W. L., “Parallel Surface Thrust Bearing”, ASLE Transactions, 1, 2, pp.254-258, 1958;

[17] Taniguchi, S., Ettles, C., “A Thermo-Elastic Analysis of the Parallel Surface Thrust Washer”, ASLE Transactions, 18, 4, pp. 299-305, 1976;

[18] Yu, T.H., Sadeghi, S., “Thermal Effects in Thrust Washer Lubrication”, ASME Journal of Tribology, 124, 1, pp.166-177, 2001;

[19] Jackson, R. L., Green, I., “The Behavior of Thrust bearings Considering Mixed Lubrication and Asperity Contact”, Tribology Transactions, 49, 2, pp.233-247, 2006;

[20] Jackson, R.L., Green, I., "The Thermoelastic Behavior of Thrust bearings Considering Mixed Lubrication Asperity Contact and Thermoviscous Effects", Tribology Transactions, 51, 1, pp.19-32, 2008;

[21] Jackson, R.L., Green, I., "Study of the Tribological Behavior of a Thrust bearing", Tribology Transactions, 44, 3, pp.504-508, 2001.

[22] Mandelbrot, B.B., "The fractal geometry of nature", Macmillan, New York, NY, 1983;

[23] Mandelbrot, B.B., "Self-affine fractal sets, I: the basic fractal dimensions", Fractals in Physics, 3, pp.3-15, 1986;

[24] Patir, N., Cheng, H.S., "An Average Flow Model for Determining Effects of Three-Dimensional Roughness on Partial Hydrodynamic Lubrication," ASME Journal of Tribology, 100, 1, pp. 12-17, 1978;

[25] Patir, N., Cheng, H.S., "Application of Average Flow Model to Lubrication Between Rough Sliding Surfaces," ASME Journal of Tribology, 101, 2, pp. 220-230, 1979;

[26] Greenwood, J.A., Williamson, J.B.P., "Contact of Nominally Flat Surface", Proceedings of the Royal Society A, 295, 1442, pp. 300-319, 1966;

[27] Kazama, T., Yamaguchi, A., "Application of a Mixed Lubrication Model for Hydrostatic Thrust Bearing of Hydraulic Equipment", ASME Journal of Tribology, 115, 4, pp.686-691, 1993;

[28] Guo, Y., Lu, X., and Li, W., et. al., "A mixed-lubrication model considering elastoplastic contact for a piston ring and application to a ring pack", Journal of Automobile Engineering, 229, 2, pp. 174-188, 2015.

[29] Love, A. E. H., "Stress Produced in a Semi-infinite Solid by Pressure on Part of the Boundary", Philosophical Transactions of Royal Society, 228, 659-669, pp. 377- 420, 1929;

[30] Johnson, K. L., "Contact Mechanics", Cambridge University Press, 1985;

[31] Barber, J. R., “Effect of Thermal Distortion on Constriction Resistance”, International Journal of Heat and Mass Transfer, 14, 6, pp. 751-766, 1971b;

[32] Zhang, X., Jackson, R.L., “An Analysis of the Multiscale Structure of Surfaces with Various Finishes”, Tribology Transaction, 60, 1, 121-134, 2017;

[33] Zhang, X., Xu, Y., and Jackson, R.L., “An Analysis of Generated Fractal and Measured Rough Surfaces in Regards to Their Multi-scale Structure and Fractal Dimension”, Tribology International, 105, pp. 94-101, 2017;

[34] Fardin, N., Stephansson, O., and Jing, L., “The Scale Dependence of Rock Joint Surface Roughness”, International Journal of Rock Mechanics and Mining Sciences, 38, 5, pp.659-669, 2001;

[35] Hamrock, B. J., “Fundamentals of Fluid Film Lubrication”, McFraw-Hill, Inc., Hightstown, NJ, 1994;

[36] Roelands, C.J.A., “Correlational aspects of the viscosity-temperature-pressure relationship of lubricating oils”, Druk. V.R.B, Groningen, 1966;

[37] Özisik, M. N., “Heat Conduction”, 2nd edition, New York: John Wiley, 1993;

[38] Khayat, K. H., Yahia, A., “Effect of Welan Gum-high-range Water Reducer Combinations on Rheology of Cement Grout”, ACI Materials Journal, 94, 5, pp. 365-372, 1997;

[39] Jackson, R. L., Green, I., “Experimental Analysis of the Wear, Life and Behavior of PTFE Coated Thrust bearing under Non-axisymmetric Loading”, Tribology Transactions, 46, 4, pp. 600-607, 2003;

[40] Hu, Y. Z., Tonder, K., “Simulation of 3-D Random Rough Surface by 2-D Digital Filter and Fourier Analysis”. International Journal of Machine Tools and Manufacture, 32, pp.83–90, 1992;

[41] Yastrebov, V.A., Anciaux, G., Molinari, J., “From Infinitesimal to Full Contact Between Rough Surfaces: Evolution of the Contact Area”, International Journal of Solids and Structures, 52, pp.83-102, 2015.

[42] Fournier, A., Fussell, D., and Carpenter, L., “Computer Rendering of Stochastic Models”, Graphics and Image Processing, 25, 6, pp.371-384, 1982.

[43] Saupe, D., “Algorithms for Random Fractals”, In: Barnsley, M.F., Devaney, R.L., Mandelbrot, B.B., Peitgen, H.-O., Saupe, D., Voss, R.F. (Eds), The Science of Fractal Images. Springer, New York, pp. 71-136, 1988.

[44] Voss, R.F., “Fractal in Nature: From Characterization to Simulation”, In: Barnsley, M.F., Devaney, R.L., Mandelbrot, B.B., Peitgen, H.-O., Saupe, D., Voss, R.F. (Eds), The Science of Fractal Images. Springer, New York, pp. 21-70, 1988.

[45] Marak, I., http://old.cescg.org/CESCG97/marak/node3.html;

[46] Majumdar, A., Bhushan, B., “Fractal Model of Elastic-plastic Contact Between Rough Surfaces”, ASME Journal of Tribology, 113, 1, pp.1-11, 1991.

[47] Yang, B.S., Choi, B.K., and Kim, H.J., 2001, “Optimum Design of Short Journal Bearings by Atificial Life Algorithm,” Tribology International, 34, pp. 427-435;

[48] Hirani, H., 2004, “Multiobjective optimization of a journal bearing using the Pareto optimality concept,” Proceedings of the institution of Mechanical Engineers, Part J: Journal of Engineering Tribology, 218, pp. 323- 336;

[49] Pang, X., Qin, N., and Dwyer-Joyce, R.S., et. al., 2010, “A General Profile Parameterization of Hydrodynamic Journal Bearings for Efficient Shape Optimization,” Tribology Transactions, 53, pp. 117-126;

[50] Fesanghary, M., Khonsari, M.M., 2012, “Topological and Shape Optimization of Thrust Bearings for Enhanced Load-carrying capacity,” Tribology International, 53, pp.12-21;

APPENDICES

A: Relationship between the load carrying capacity and the cut-off frequency for different angular velocity

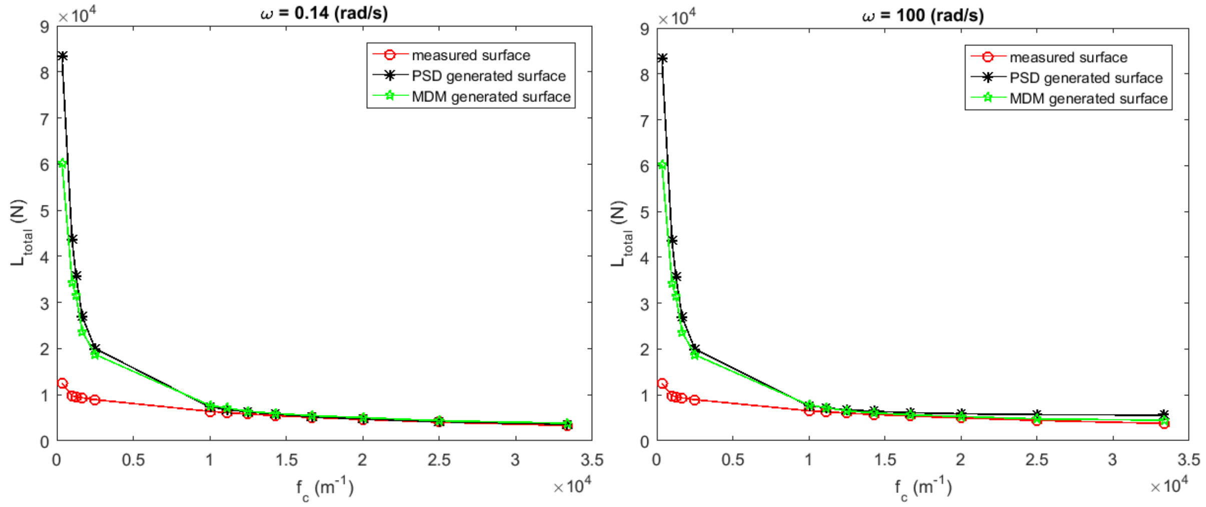

Fig.A1 - Relationship between the load carrying capacity (L_{total}) and the cut-off frequency (f_c) for different angular velocity (ω)

B: Relationship between the frictional torque and the cut-off frequency for different angular velocity

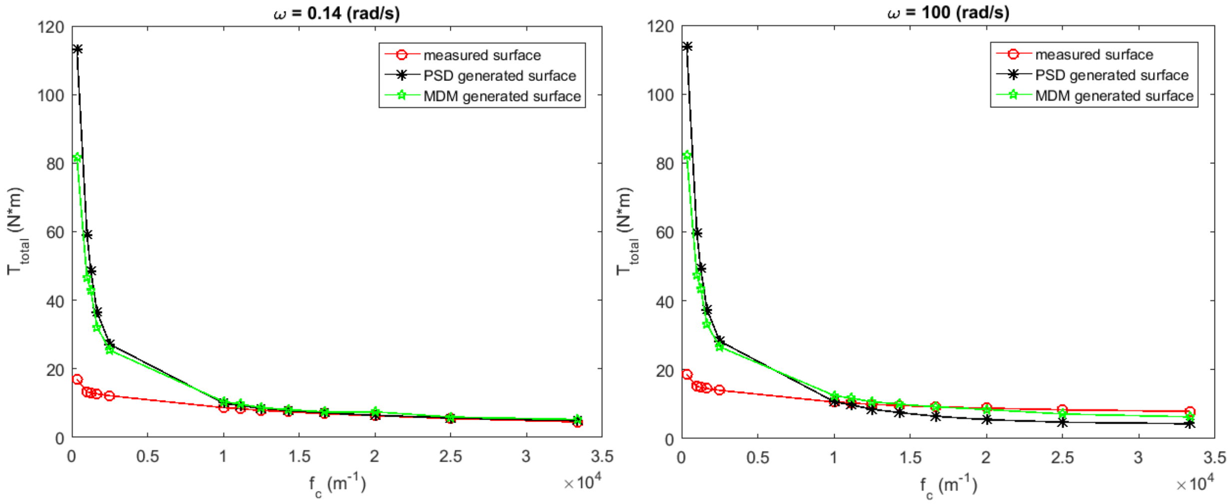

Fig.B1 - Relationship between the total frictional torque (T_{total}) and the cut-off frequency (f_c) for different angular velocity (ω)

C: Changing trend between the cut-off frequency and the total load carrying capacity

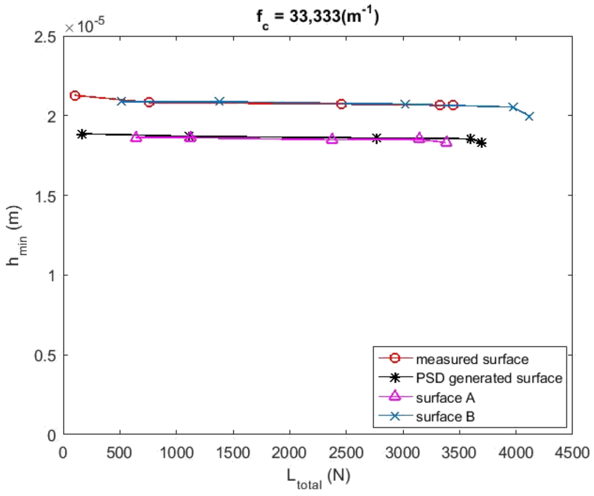

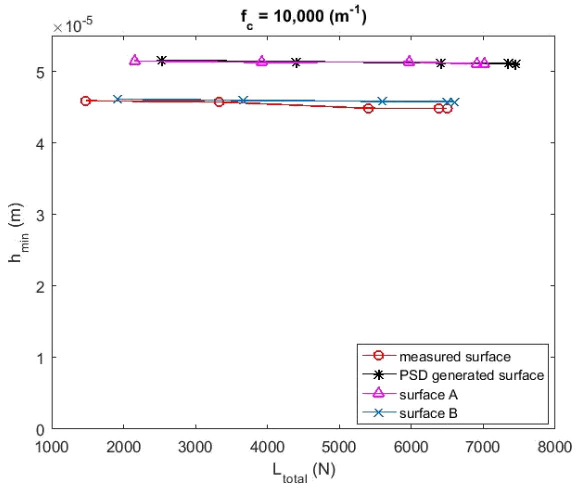

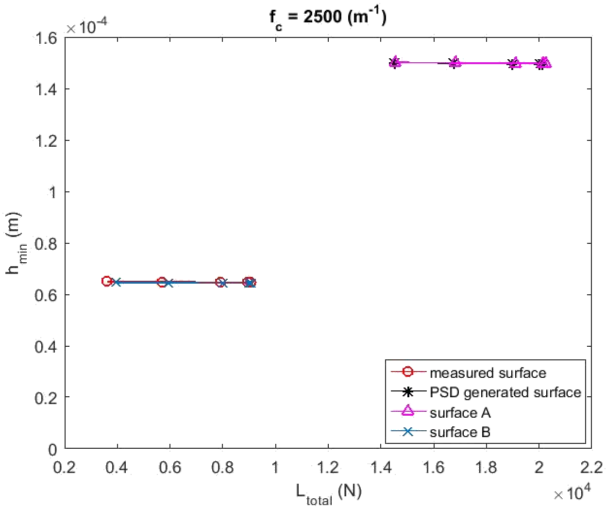

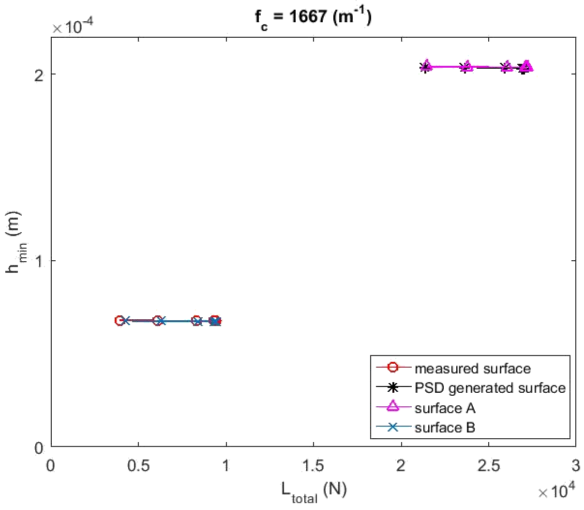

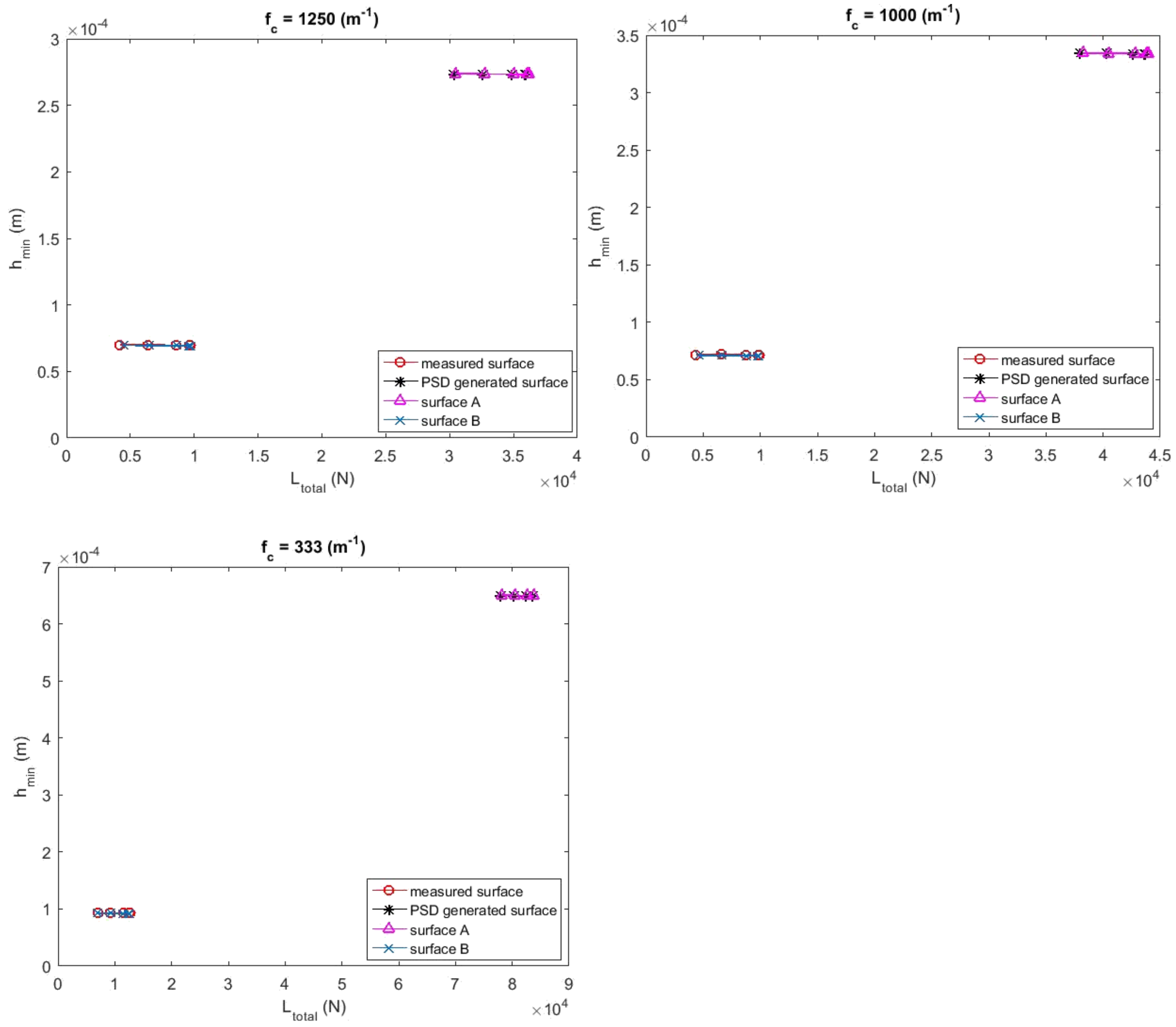

Fig.C1 - Changing trend between the cut-off frequency (f_c) and the total load carrying capacity (L_{total})

D: Changing trend between the cut-off frequency and the total frictional torque

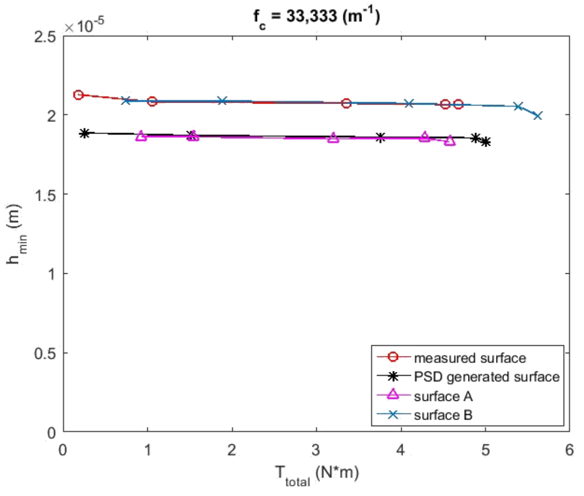

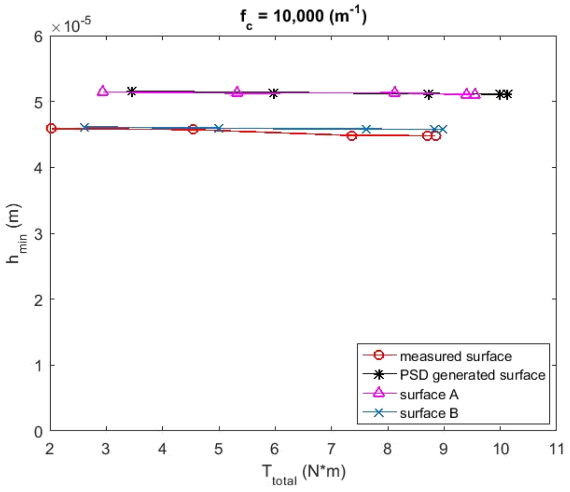

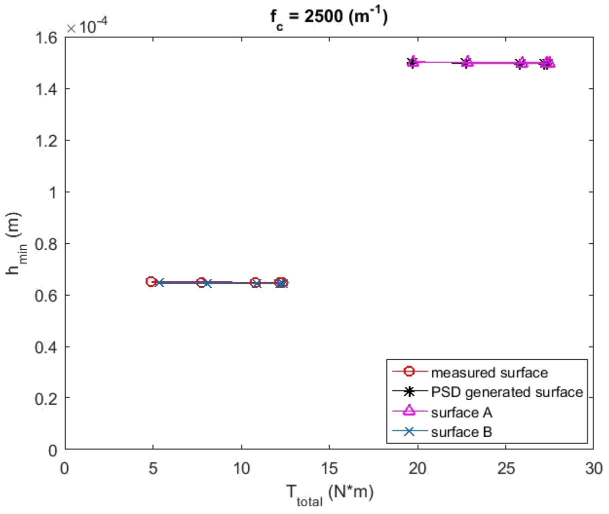

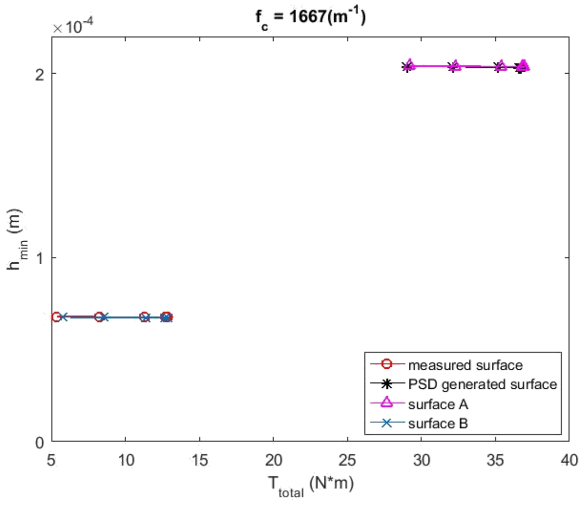

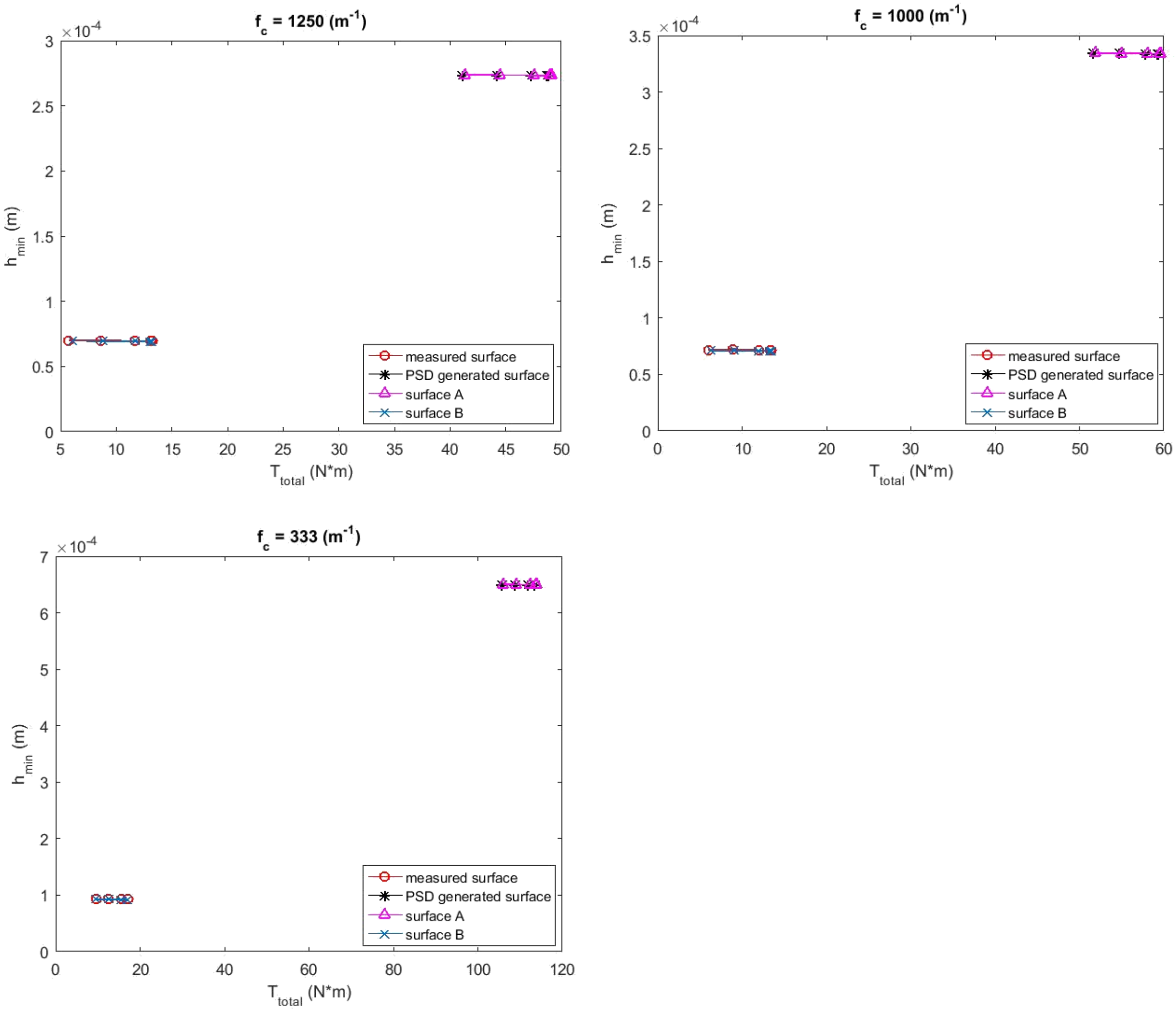

Fig.D1 - Changing trend between the cut-off frequency (f_c) and the total frictional torque (T_{total})